HYBRID BIOSENSING SYSTEMS FOR THE DETECTION OF BIOMOLECULES AND DISEASE BIOMARKERS

A THESIS SUBMITTED TO
THE GRADUATE SCHOOL OF ENGINEERING AND SCIENCE
OF BILKENT UNIVERSITY
IN PARTIAL FULFILLMENT OF THE REQUIREMENTS FOR
THE DEGREE OF
MASTER OF SCIENCE
IN
MATERIALS SCIENCE AND NANOTECHNOLOGY

By
YUSUF ASLAN
August 2023

HYBRID BIOSENSING SYSTEMS FOR THE DETECTION OF BIOMOLECULES AND DISEASE BIOMARKERS

By Yusuf Aslan

August 2023

We certify that we have read this thesis and that in our opinion it is fully adequate,in scope and in quality, as a thesis for the degree of Master of Science.

Fatih İnci (Advisor)

Adil Denizli

Bülend Ortaç

Approved for the Graduate School of Engineering and Science:

Orhan Arıkan
Director of the Graduate School

ABSTRACT

HYBRID BIOSENSING SYSTEMS FOR THE DETECTION OF BIOMOLECULES AND DISEASE BIOMARKERS

Yusuf Aslan
M.S. in Materials Science and Nanotechnology
Advisor : Fatih İnci
August 2023

Optical metasurfaces are configurations of artificially structured surfaces designed to obtain unusual electromagnetic properties. The ability to manipulate a confined electromagnetic field enables metasurfaces to be utilized as optical point-of-care (POC) biosensors for the detection of low concentrations of biomarkers. Moreover, the integration of fluorescent molecules and plasmonic metasurfaces is utilized to enhance both plasmonic and fluorescent signals; however, the nanoscale distance and spectral overlap between the fluorescent emitter and plasmonic metasurface are crucial for the separation of the fluorescence-coupled plasmonic radiation and non-radiative induced plasmon surface entrapment. In this study, fluorescently labeled (FITC) proteins are integrated over a plasmonic metasurface via three different surface modifications for obtaining a hybrid biosensing system that boosts the device's plasmonic sensitivity and lowers the detection limit. The metasurface is fabricated via physical vapor deposition of titanium (10 nm), silver (30 nm), and gold (15 nm), respectively over polycarbonate nanograting substrates of optical disks (DVDs). Additionally, the surface modifications are arranged via short-distance, medium-distance, and long-distance modifications for fluorescently labeled molecule binding. After the evaluations, the highest plasmonic wavelength shift over the FITC labeled protein binding is obtained from the medium-

distance modification with ~4.4 times signal enhancement over the short-distance modification. The medium-distance modification is further combined with an immunoassay for the detection of Alzheimer's disease. Consequently, this study paves the way for designing new arrangements on a metasurface to couple with fluorescence molecules while enhancing the analytical performance of the plasmonic biosensor.

Keywords : Metasurfaces, Surface Plasmon Resonance (SPR), Fluorescence, Point-of-care (POC), Alzheimer's Disease (AD)

ÖZET

BİYOMOLEKÜLLER VE HASTALIK BİYOBELİRTEÇLERİNİN TESPİTİ İÇİN HİBRİT BİYOALGILAMA SİSTEMLERİ

Yusuf Aslan
Malzeme Bilimi ve Nanoteknoloji, Yüksek Lisans
Tez Danışmanı : Fatih İnci
Ağustos 2023

Optik metayüzeyler, elektromagnetik dalgayı yönlendirmek ve kontrol etmek için kullanılan yapay yapılardır. Nanometre ölçeğine sınırlandırılan elektromanyetik alanı manipüle etme kabiliyeti sayesinde, metayüzeyler vücutta düşük konsantrasyondaki yer alan biyobelirteçlerin tespiti için optik hasta başı (POC) biyosensörleri olarak kullanılabilirler. Ayrıca floresan molekülleri ile plazmonik metayüzeylerin entegrasyonu, plazmonik ve floresan sinyallerini artırmak amacı ile kullanılabilir. Ancak bu sinyal artırımının elde edilebilmesi için, floresan molekülleri ile pazmonik metayüzey arasındaki nanometre ölçeğindeki mesafenin ve floresan ile plasmonik kaynakların spektral örtüşmesinin, floresanla arttırılan plazmonik ışıma elde edilmesi için optimize edilmesi gerekir. Bu şekilde, yüzeye hapsolan yüzey plazmonlarının ışıma olmadan enerji değişimi yapması ile floresan eşlenen plazmonik ışımanın sinyal artırımında bulunması durumlarının birbirinden ayrılmaları gerekmektedir. Bu çalışmada, floresan molekülleri (FITC) ile işaretlenen proteinler üç farklı ayırım mesafesine sahip yüzey modifikasyonlarının aracılığıyla metayüzeye bağlanırlar. Bu çalışma, düşük tespit sınırına sahip ve flüoresan molekülleri ile plazmonik duyarlılığı arttırılmış bir hibrit biyosensör sistemi tasarlamayı ve üretmeyi hedefledik. Çalışmada kullanılan metayüzey, polikarbonat tabanlı (DVD'ler) yüzey üzerine sırasıyla titanyum (10 nm), gümüş (30 nm) ve altın (15 nm) metallerinin fiziksel buharlaştırma yöntemi ile kaplanmasıyla üretildi.

Ayrıca yüzey modifikasyonları, floresanlı molekül bağlanması için kısa mesafe, orta mesafe ve uzun mesafe modifikasyonları olacak şekilde seçildi. Yapılan değerlendirmeler sonucunda, avidin-FITC ile işaretlenen orta-mesafeli modifikasyon en yüksek plazmonik dalga boyu kaymasını sağladı. Bu şekilde, orta mesafe modifikasyonundan elde edilen sinyal, kısa mesafe modifikasyondan elde edilen sinyale kıyasla yaklaşık 4.4 kat sinyal artışı sağladı. Bu nedenle, Alzheimer hastalığı tespiti için orta-mesafeli modifikasyon üzerine Alzheimer biyobelirteçlerine spesifik antikorlar yerleştirildi. Sonuç olarak, bu çalışmada, floresan molekülleri kullanılarak, hem plazmonik biyosensörün analitik performansı arttırıldı, hem de plazmonik metaüzey üzerinde yeni düzenlemeler tasarlandı.

Anahtar Sözcükler : Metayüzeyler, Yüzey Plazmon Rezonansı, Floresans, Hasta Başı, Alzheimer Hastalığı

To my dear parents…

Acknowledgement

On the first day of my Master's program, I wandered around campus with a sense of uncertainty, pondering where and how to begin unraveling the complexities of scientific knowledge. Then, I found myself in the newly sprouting microcosm of Incilab. Asst. Prof. Dr. Fatih İnci initiated me by handing me a challenging project where I could delve into the convoluted world of optics and biosensors. At first, I was afraid of making mistakes. He taught me not to avoid making mistakes but to embrace them, to learn from them. In addition, he equipped me with a toolbox of scientific thinking, experimental design, and figure-creating skills. He also encouraged me to think outside the box and develop innovative and creative solutions. Moreover, he has approached me as if I am one of his colleagues and trusted me along the arduous ways of research. I am grateful to him for allowing me to be a part of Incilab and to contribute to the ground-breaking research.

I would also like to thank the thesis committee, Prof. Dr. Adil Denizli and Asst. Prof. Dr. Bülend Ortaç for their guidance and support in my thesis. Furthermore, I extend my gratitude to Asst. Prof. Dr. Bülend Ortaç for providing me with the assistantship opportunity for MSN 510-1, Imaging Techniques in Materials Science and Nanotechnology. His guidance has also been influential to my academic journey. I hope our insightful and productive discussions on research and academia will continue.

I would like to express my gratefulness to my colleagues and the members of Incilab. Dr. Özgecan Erdem was always available with her support and help. She was also like a big sister to me. I am also thankful to Eylül Gülşen Yılmaz and Beyza Nur Küçük for their enduring friendship and support. I feel like a part of a team while I am working with them. In addition, Kutay Sağdıç and Esma Derin had critical contributions and support to the project. I am also grateful for their friendship. In addition, I would like to thank Hussain (Dhrubo) Kawsar Chowdhury for his friendship and his accompany during the experiments. Further, I would like to also thank Murat A. Güngen for his valuable discussions about academia, scientific history, and investment tips. Moreover, Ekin Bircan Boşdurmaz had his supported over simulation and helped me to overcome technical problems. I appreciate his efforts.

UNAM facility is home to many hard-working and successful engineers and technicians. Especially, Mr. Abdullah Kafadenk and I worked together on the optimization of DVD-templated metasurface fabrication, and he taught me the PVD process. In addition, Ms. Esra Arman Karaaslan and Mr. Can Güven provided their help during common equipment usage. I am thankful to them for their support.

I also made many friends and colleagues at Bilkent University who supported me during my Master's. Therefore, I would like to thank Md. Faysal Hossain, Elif Sena Temirci, Arda Kurucu, Enise Kartal, Ceren Alataş, Mehmet Atıf Durmuş, Hilal Korkut, Md. Kawsar Ahmed, Farzan Shabani, and many more for their bits of help.

Additionally, I would like to express my appreciation to Bilkent University, the UNAM facility, and the Material Science and Nanotechnology (MSN) department for providing me with an encouraging academic environment during my Master's degree. Moreover, I would like to extend my acknowledgement for the support of the TÜBİTAK 3501-Career Development Program (Project No: 120Z335) for their crucial funding during my thesis study.

Last but not least, I would like to give my utmost gratitude to my family and Aslı Bozkurt for their endless support during my thesis. My mother, Adalet İpek Yurdacan, my father, Halis Aslan, and my sister, Ayşe Elif Aslan, were always ready to help me when I encountered any difficulty. Aslı Bozkurt was a shore that I can harbor in times of need. I appreciate her enduring support. I would like to also express my gratitude to my grandparents, Rukiye Aslan, Emine, and Ekrem Yurdacan, for all their support and love.

Contents

List of Figures

List of Tables

CHAPTER 1

1. INTRODUCTION

1.1 Introduction to Point-of-Care

Diseases are an integral part of our daily lives, posing constant threats to our health, as well as prompting the need for medical care to sustain us and accelerate the healing of injured body parts, such as organs and tissues. Hospitals, universities, and medical research centers have typically been at the forefront of disease identification, further investigation, and therapy. These establishments provide diverse traditional diagnostic modalities, encompassing laboratory analyses, imaging procedures, endoscopic examinations, microbiological assessments (including biopsy-based techniques), electrocardiography, and pulmonary function evaluations [1]. In addition to these methods, laboratory testing provides precise, objective, and most importantly, quantitative information by utilizing a broad range of disease-specific biomarkers isolated from bodily fluids. Several conventional laboratory testing platforms are clinical chemistry analysis, hematology, microbiology culture, polymerase chain reaction (PCR), immunoassays, flow cytometry, and mass spectrometry. In addition, they often require a specialist to perform the assays, and they are frequently operated with lengthy procedures. One critical solution for streamlining diagnosis is to deploy new strategy into point-of-care (POC) and bed-side. Briefly, POC is defined as the applications surrounded by laboratory-independent, specific, and sensitive delivery of diagnosis to near-patient with a short turnaround time. The socio-economic implications of POC diagnostics are worth analyzing, particularly in the context of 45.4 billion USD global revenue by 2022, which is expected to rise to 75.5 billion USD by 2027, meaning a compound annual growth rate of 10.7% [2]. The main impact of the growth is attenuated by the increasing prevalence of infectious diseases and increased availability of self-testing and home-care products. Furthermore, the development of multiplexed POC devices is considered a key area of opportunity in the market, and many researchers are working towards creating single

platforms capable of simultaneous detection of multiple targets. In the future, high-throughput integrated platforms with multiplex capabilities are also expected to have an impact on personalized medicine, similarly to how they have influenced POC.

To adapt the tests/assays at the POC settings, the World Health Organization (WHO) introduced a set of parameters that an ideal test should meet for utilization at every stage of healthcare [3]. These parameters are coined under the abbreviation of ASSURED, which is affordable, sensitive, specific, user-friendly, rapid & robust, equipment-free, and delivered. These criteria facilitate decision-making in clinical management and help guide treatment more efficiently. Currently, these parameters have been further updated under RE-ASSURED, with the addition of real-time connectivity and ease of specimen collection [4] (Figure 1.1). These new standards provide rapid access to information for patients and healthcare workers through real-time connectivity. They also introduce the ease of specimen collection term, such as non-invasive [5] or minimally invasive methods [6], in order to increase the feasibility of self- and home-testing. In addition, the RE-ASSURED qualifications have also emphasized the importance of safely disposing of single-use rapid diagnostic tests by introducing sustainable waste management regulations.

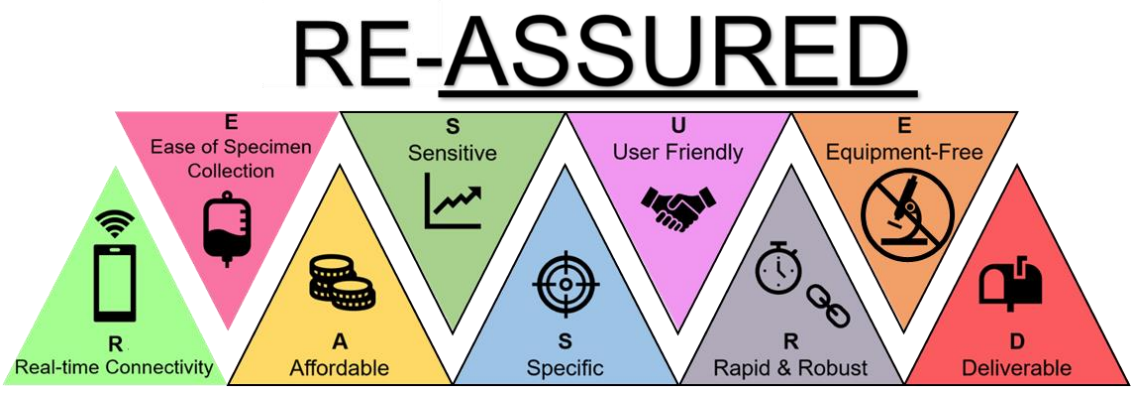

Figure 1.1: The term "RE-ASSURED" represents a set of essential criteria guiding the design and functionality of POC-based strategies.

The utility of the RE-ASSURED criteria in POC diagnostics reduces the patient's reliance on centralized laboratories. The advent of biosensors has accelerated this

decentralization transition by providing quantitative and rapid measurements at the point of need. This effectively aids the decision-making process of the patient's condition and reduces the burden on healthcare facilities [7]. These biosensors can seamlessly integrate into portable and affordable platforms, facilitating their distribution to areas with limited resources, including low-income countries, disaster zones, and rural regions. As the commercial market for biosensors expands and, they have the potential to be incorporated into new engineering fields, including the Internet of Things (IoT), artificial intelligence, and printed electronics [8]–[10].

1.2 Biosensor

Biosensors are analytical devices that integrate receptors and physicochemical transducers for investigating a biological event, such as antibody-target binding [11]–[13]. The change in the monitored biomolecular interaction is selectively recognized as a signal change by the transducer. The receptors in a biosensor are biological or synthetic molecules that recognize an analyte of interest and share information about the investigated biological event. Molecularly imprinted polymers [14], aptamers [15], DNAs [16], enzymes [17], and even cells [18] can be utilized as receptors. They can quantitively recognize many different analytes, e.g. molecules, proteins, nucleic acids, toxins, whole viruses or cells, bacteria, extracellular vesicles, and more (Figure 1.2), and utilize them for the diagnosis and prognosis of diseases [19]–[21]. The transducer of a biosensor is a platform that converts a biological event into a measurable signal [22]. They serve as a bridge between the quantification and recognition of analytes (Figure 1.2). Transducers can vary by the working principle of the physicochemical. Electrochemical [23], optical [24], piezoelectrical [25], thermal [26], and magnetic [27] transducers are some of the most utilized platforms in biosensors.

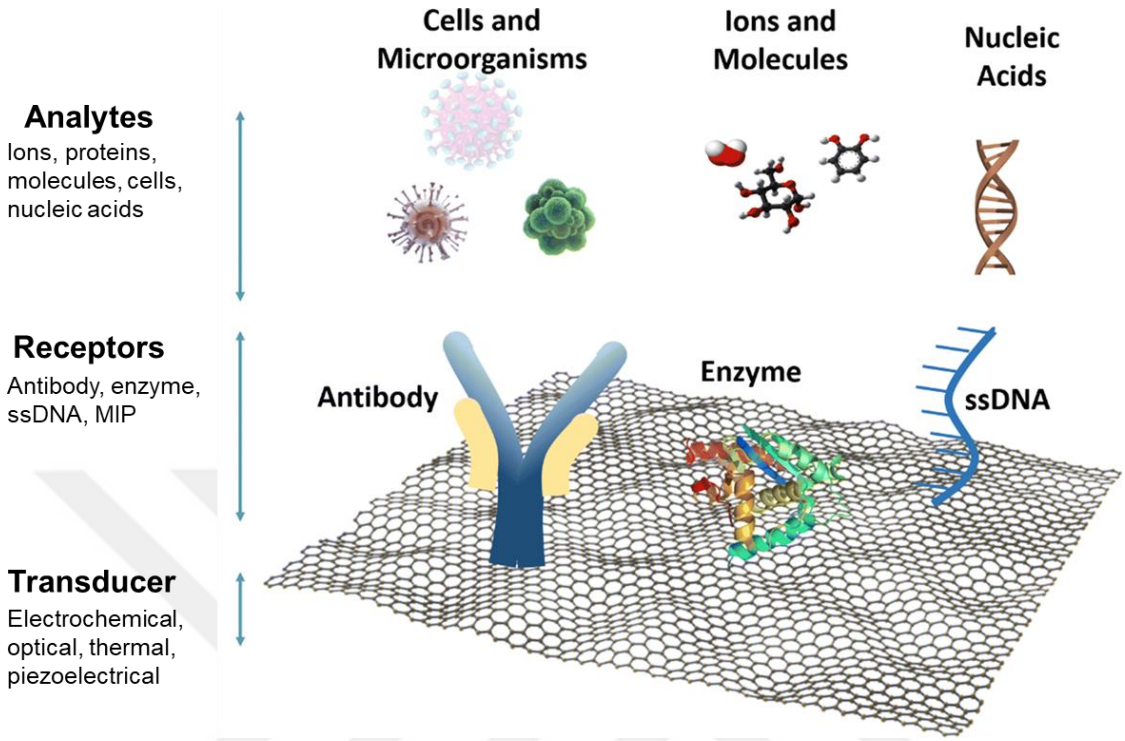

Figure 1.2: Elements of a biosensor are placed over a 2D graphene layer [28]

The first biosensor, developed by Professor Leland C. Clark in 1962 for monitoring oxygen levels in the blood during cardiopulmonary bypass, utilized two simple materials: platinum electrodes (working and reference) and a polyethylene membrane containing the enzyme Glucose Oxidase [29], [30]. Over time, biosensors have incorporated various materials in different forms to enhance their performance. Paper [31], thin films, nanoparticles, chemically patterned or functionalized surfaces [32], [33], two-dimensional (2D) substrates [34], membranes [35], [36], and photonic crystals [37] can be listed as examples of these materials. Each of these materials brings a unique property to the biosensors. For example, 2D materials provide high sensitivity, high surface-to-volume ratio, and robustness. These features are exploited for the analysis of surface adsorbing low-concentration analytes [38]. However, their fabrication and device integration are challenging in geometry, size, and alignment inconsistencies [39]. Another example is paper-based systems owing to inexpensive, robust, and easy to functionalize fashions [40]. They also enable passive fluid transport through the capillary effect. However, they mostly lack multiplexing and real-time monitoring [41]. Furthermore, they

may cause false positive or false negative results due to issues such as cross-reactivity and concentration values lower than the LOD [15]. The usage of each material and the type of each biosensor provide various advantages and disadvantages. To assess this in a controlled manner, some performance parameters are introduced to the biosensor-realm [42]–[44]. Common performance parameters for biosensors include limit of detection (LOD) [45], dynamic range [46], sensitivity and specificity, response time [47], stability and reusability [48], reproducibility [49], accuracy [49], resistance to interference and matrix effects [50], and shelf life [51]. For example, the LOD is the lowest concentration value that a biosensor can reliably detect and distinguish from background noise [52]. It represents the sensitivity of the assay and becomes particularly significant when dealing with low-concentration analytes in bodily fluids. A wide dynamic range provides the measurement of both high and low concentration values with accurate and reliable signal [53]. Providing all of these performance parameters in a single device is the ideal condition for ensuring optimal biosensor performance. Yet, in practice, achieving the utmost potential of each parameter concurrently represents a challenge since enhancements in one parameter may be accompanied by drawbacks in another. This trade-off becomes evident during the design and development of biosensors.

To understand this trade-off, it is critical to overview the benefits and drawbacks associated with the utilization of various transducers on biosensors. Each transducing platform offers unique capabilities and limitations that can impact the overall performance of the biosensor. By considering these factors, researchers can make informed decisions about which performance parameters to prioritize based on the specific application requirements. For example, electrochemical biosensors mostly provide cost-effective, low LOD, and rapid measurements [54]. However, they interfere with matrix effects in complex samples and sensor surfaces are suspected to fouling which can impair the sensitivity [55]. Piezoelectric biosensors also perform highly sensitive, label-free and real-time measurements [56]. However, they are complex and require frequent calibration [57]. On the other hand, optical biosensors mostly provide label-free, real-time, high-sensitive, and multiplexed detection of many analytes [58]–[60].Current challenges associated with them are complex instrumentation [61], device-cost [61], [62], sample matrix interaction [63], and limited penetration depth. The impact of these challenges can vary between different subtypes of optical biosensors.

1.2.1 Optical Biosensors

Optical biosensors qualitatively and quantitatively recognize biological events through changes in optical properties upon the analyte interaction. The signals mostly include refractive index, absorbance, reflectance, and scattering in these biosensing modality. Each of these signals is generated through different optical phenomena that occur between the material and light. For instance, the change in inelastic scattering of light can be observed through the optical phenomenon of Raman scattering, where photons interact with molecules of interest, causing shifts in energy values of their vibrational and rotational modes [64]. Additionally, Raman scattering signals can be amplified by integration of metal nanostructures (Surface-enhanced Raman Spectroscopy, SERS), exploiting the confinement of the electromagnetic field at the nanoscale. Another example of optical biotarget detection is the change in resonance reflection/transmission of photonic crystals after analyte capture. The shift in resonance occurs because of the localized changes in crystal dielectric permittivity upon target interaction [65]. Whispering-gallery mode (WGM) [66], surface plasmon resonance (SPR) [67], localized surface plasmon resonance (LSPR) [68], and reflectometric interference spectroscopy (RIfS) [69] can be given as the other examples of optical biosensor types.

In addition, optical biosensors can be categorized based on the utilized optical signal transduction mechanism. Each type of optical biosensor offers different benefits and drawbacks depending on the nature of the optical signal and materials used. For instance, advanced fluorescence biosensors can provide multiplexed analysis of biomarkers at the resolution of a single molecule [70]. However, this ultra-sensitivity may accompanied by higher costs and the need for complex designs [71]. Metal nanoparticles are also widely used in lateral flow assays (LFAs) for detecting pregnancy (via human chorionic gonadotropin hormone, hCG) [72], COVID-19 [73], and even cancer [74]. However, LFAs have inherent limitations in sensitivity as they often rely on bioreceptors through immunoassays and mainly provide semi-quantitative or qualitative results [75]. Among optical biosensors, plasmonic biosensors, such as SPR and LSPR, offer high adaptability to POC conditions due to their portability and high sensitivity [76]. The main

challenge currently faced by these biosensors is the need to develop scalable products that can reduce overall costs while maintaining their high sensitivity.

1.2.2 Plasmonic Biosensors

Plasmonic biosensors have garnered significant interest in the last decades [67], [76]–[78]. They utilize propagating surface plasmon polaritons (PSPPs) between metal surface and the dielectric medium, and these PSPPs form an evanescent electromagnetic (EM) field on the dielectric medium of the biosensor (up to 100 nm in metal surfaces and few nanometers in metal nanoparticles) which is highly sensitive to the changes in refractive index [76]. Biomarker interactions on a biosensor cause a change either in the refractive index or in the wavelength of the resonance [79].

Briefly, utilizing SPR biosensors offer real-time and label-free detection of biomarkers, allowing for rapid and continuous tracking of biomolecular binding events. SPR can be harnessed or enhanced throughout many materials including thin metal films [80], [81], metal nanoparticles [82], [83], 2D materials (such as graphene [84], transition metal dichalcogenides [85], MXenes [86], and more), and metasurfaces [87]. However, SPR-based biosensors encounter challenges in achieving to detect low molecular weight compounds at minute concentrations [88]. In addition, multiplexing [89], [90] and surface fouling in complex media [91] are also considered as the exiting difficulties of the field.

Metasurfaces have potential to tackle these challenges by improving LOD with greater near EM field enhancement of periodically formed metal nanostructures and allowing for the detection of small molecules [92]. The periodic structure of these materials can be also harnessed for multiplex detection by the usage of complementary metal-oxide semiconductor (CMOS) or charge-coupled device (CCD) cameras [93]. Integrating antifouling coatings, such as zwitterionic polymers [94], of the metasurface can also address the surface fouling limitation for not only SPR-based system and also for the other modalities [95].

On the other hand, plasmonic biosensors can be incorporated into compact and portable devices, enabling applications in POC settings and decentralized healthcare [96]. Their integration with microfluidics reduces sample volume and provides high-throughput measurement with separated channels or chambers [97]. With their

exceptional sensitivity, real-time detection capability, versatility, and potential for integration, plasmonic biosensors have emerged as a promising platform for various biomedical and diagnostic applications.

1.3 Surface Plasmon Resonance

Surface plasmons (SPs) are electromagnetic waves that propagate along a surface and are formed by the collective oscillation of free electrons trapped between a dielectric interface and a conductor surface. These oscillating free electrons create a plasmonic resonance, which is responsive to changes in surface charge oscillations and the electromagnetic field of light. By incorporating subwavelength nanoplasmonic structures, it becomes possible to confine the electromagnetic field within dimensions smaller than the wavelength, potentially enhancing sensitivity.

The interaction between the surface charge density and the electromagnetic field (Figure 1.3 a) yields two outcomes. Firstly, the momentum of the SP, $\hbar k_{SP}$, mode exceeds that of a free-space photon, $\hbar k_0$, with the same frequency (Figure 1.3b). This momentum increase in the SP mode arises from the binding of the SP to the surface, and it is crucial to establish a connection between the incoming light and SP at the same frequency to generate SPs. Secondly, the interaction between the surface charges and the surface propagating electromagnetic field leads to the generation of a perpendicular electromagnetic field. This field exponentially decays in strength as the distance from the surface increases (Figure 1.4) from both the dielectric (δ_d) and metal layer (δ_m). This evanescent field is a consequence of non-radiative SPs being bound to the surface, preventing their propagation away from the surface.

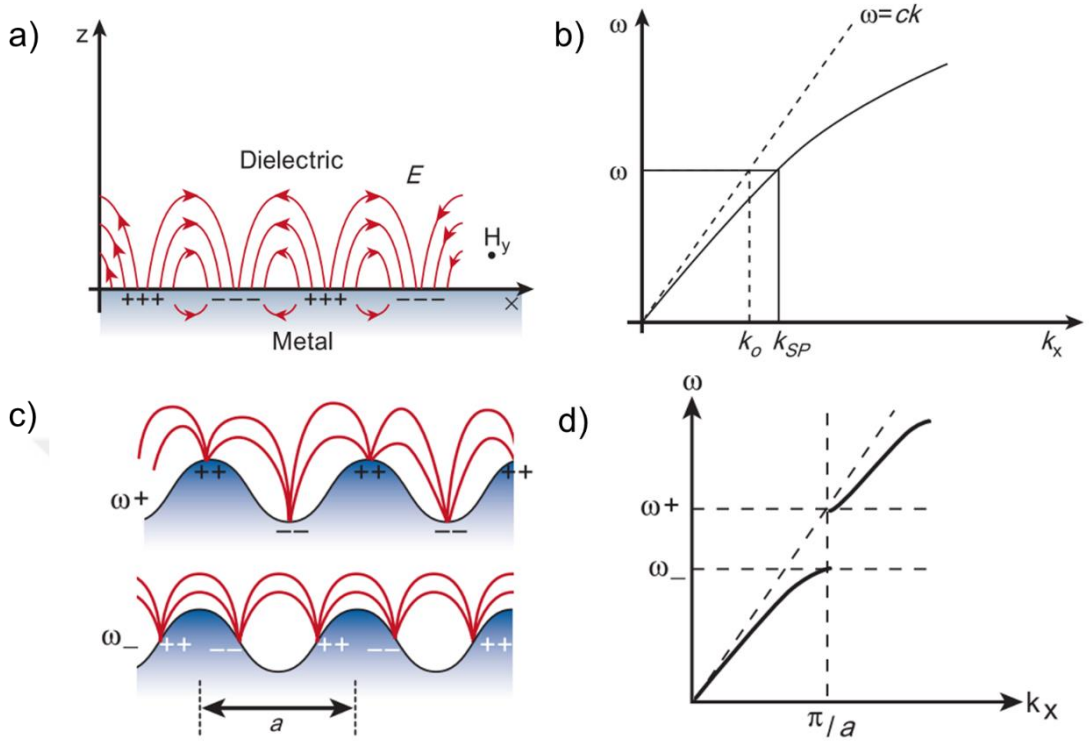

Figure 1.3: The interface between a metal and a dielectric host surface plasmons (SPs), exhibit distinctive dispersion curves. b) A momentum mismatch exists between the SP's momentum (k_{SP}) and that of a free-space photon (k_0) at the same frequency. c) When a periodic pattern is applied to the metal surface, it forms an SP photonic bandgap. d) This periodic patterning enables the creation of a stop-gap for SPs, known as the SP stop gap [98].

The momentum mismatch can be addressed through three distinct methods: Firstly, the utilization of a prism enhances the momentum of the incident light, facilitating coupling with the momentum of SPs. Secondly, introducing topological defects on the surface, such as nanoscale holes or bumps, enables the localized generation of SPs through scattering. Lastly, metallic diffraction gratings (Figure 1.3c) can be employed to couple the momentum of SPs and incident light by leveraging the scattering of light from the grating structure. When the metal surface is textured periodically, it can result in the creation of a stop-gap for SPs known as an SP photonic bandgap. This bandgap occurs when the period of the texture is half the wavelength of the SP, as depicted in the

dispersion diagram. Within this bandgap, SP modes with frequencies between the upper (ω^+) and lower (ω^-) band edges are unable to propagate (Figure 1.3 d). This periodic texturing can be extended to two dimensions, effectively blocking SP propagation in all in-plane directions and forming a complete bandgap for SPs. At the band edges, there is a high density of SP states, which significantly enhances the associated electromagnetic field.

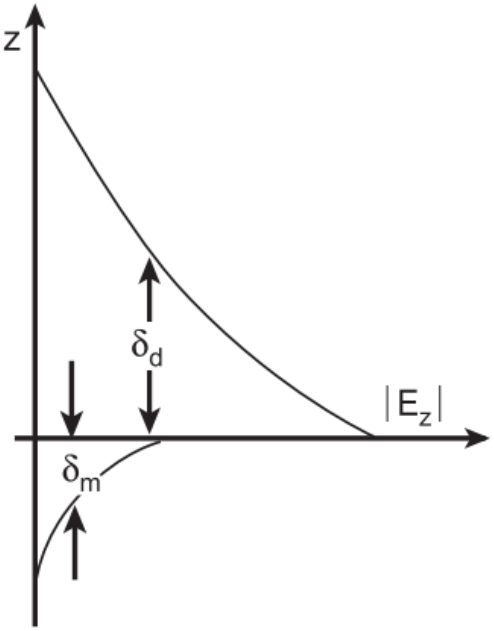

Figure 1.4: Metal (δ_m) and dielectric (δ_d) decay lengths of the evanescent electromagnetic field that is perpendicular to the plasmonic metal surface [98].

1.4 Plasmonic Metasurfaces

Plasmonic metasurfaces are artificially engineered interfaces that exhibit unique optical properties due to their subwavelength-scale structural features and the collective behavior of plasmons.

They are designed to manipulate and control light at the subwavelength level by tailoring the arrangement, size, shape, and composition of nanostructured metal elements. Metallic or dielectric nanoparticles [99], nanowires [100], nanorods [101], nanoholes [102], bowties [103], or nanoslits [104] are examples of metasurface building blocks. By

arranging these structures in periodic or aperiodic patterns, plasmonic metasurfaces can achieve properties that are not found in naturally occurring materials.

These metasurfaces possess the extraordinary ability to control light in ways such as subwavelength imaging [105], negative refraction [106], enhanced light-matter interaction [107] and even achieving cloaking effects [108]. This is achieved by exploiting phenomena like surface plasmon resonances [109], extraordinary optical transmission [110], and negative refractive index [111]. By engineering the geometry and composition of the metasurface, researchers can precisely control the interaction between light and matter, enabling novel functionalities and unprecedented optical properties.

The fabrication processes for the periodic building blocks of plasmonic metasurface primarily involve electron beam lithography [112], ion-beam milling [113], nanoimprint lithography [114], and self-assembly techniques [115]. Nevertheless, the challenge of cost-effective large-scale fabrication of plasmonic metasurfaces persists, despite advancements in their applications. This hinders the widespread and inexpensive usage of metasurfaces in POC applications.

1.4.1 Scalable Plasmonic Metasurfaces for Biosensing Applications

Plasmonic metasurfaces consist of subwavelength nanostructures or meta-atoms arranged on a planar surface, effectively confining the electromagnetic field to the vicinity of the surface. These platforms have emerged as promising optical biosensors for rapid and highly sensitive detection of biomarkers. However, their fabrication processes often involve expensive and time-consuming methods, limiting their integration into POC biosensors on a large scale.

Efforts are being made to address this challenge [116]–[120]. R. Ahmed et al. proposes a solution by utilizing digital versatile discs (DVDs) as grating substrates, eliminating the need for complex nanofabrication techniques and reducing associated costs [120]. DVD substrate has an intrinsic polycarbonate (PC) templated grating structure which provides periodic geometry for the metasurface fabrication eliminating the need for the nanostructure formation step, enabling a Fano resonance. Fano

resonances have an asymmetrical sharp peak followed by a dip that is formed by the constructive interference of broad and narrow resonance. The PC surface can also be chemically etched for changing the geometrical parameters (width, height) of the gratings (Figure 1.5). The consequent geometrical change in the grating structure has allowed tuning the plasmonic resonance of the metasurface. This platform provides the real-time detection of rec-gp120 protein that is located on HIV-1 viruses. This device represents a significant advancement in the cost-effective and scalable production of plasmonic POC devices.

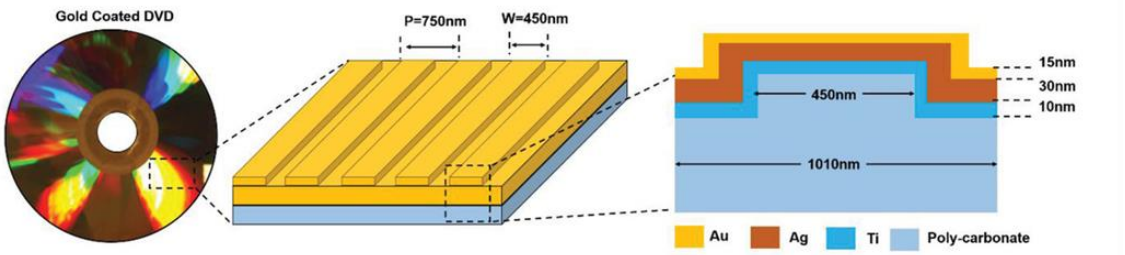

Figure 1.5: Grating structure and cross-sectional representation of the DVD metasurface [120].

However, there is a need to further enhance the sensitivity of the signal for tracking minute concentrations of biomarkers, such as amyloid beta and tau [121], circulating and tumor originated cells and nucleic acids [122], extracellular vesicles [123], for the early diagnosis of many diseases. Signal enhancing methods can be employed to achieve this. Furthermore, to meet the RE-ASSURED criteria of POC biosensors, the optical measurement setups employed for monitoring changes in plasmonic resonance should prioritize affordability and portability. For instance, platforms equipped with LED sources [97], [120] and cost-effective detectors, such as portable spectrometers [120], CCDs [93], and sCMOS [97], featuring 3D printed bodies [124] can offer cost-effective and easily transportable solutions.

1.5 Sensitivity Enhancement on Plasmonic Platforms

The signal amplification in plasmonic arrays traditionally relies on field enhancements achieved through near-field and far-field coupling, employing various methods. One fundamental approach involves modifying the design of the plasmonic surface to incorporate smaller periodic structures such as nanorods, nanowires, cavities, and nanoparticles [125]. However, fabricating these nano-scale subwavelength dimensions on plasmonic surfaces increases the complexity and cost of the fabrication process [126].

To address these challenges, researchers have explored alternative strategies such as integrating metallic nanoparticles with surface coatings [127], [128], modifications [129], antibodies [68], and aptamers [130], aiming to reduce the fabrication cost of small-sized nanostructures. Furthermore, the utilization of emitting and radiative materials other than nanoparticles is becoming progressively more prominent. Examples include fluorescent proteins [131], luminescent metal–organic frameworks (MOFs) [132], upconversion nanoparticles [133], and quantum dots [134]. These elements offer stronger coupling effects through methods like enhancing and inhibiting spontaneous emission inside a cavity and coupling to plasmonic surfaces.

Fluorescent targets, in particular, have been employed to increase the sensitivity of plasmonic platforms by monitoring changes in emission intensity [135] and plasmonic resonance [136]. Plasmonic-enhanced fluorescence biosensors represent a rapidly growing field with diverse applications in biomarker detection [137]. However, conventional fluorescence tracking often relies on specialized equipment like confocal and wide-field fluorescence microscopes, which require bulky and costly detectors such as photomultiplier tubes (PMTs) and avalanche photodiodes (APDs) [138]. This reliance on specialized equipment can significantly increase costs and hinder the portability of fluorescence tracking setups.

In the literature, there are limited examples of biosensors that utilize plasmonic resonance tracking for fluorescence-enhanced plasmonic detection [136], [139]. This poses a challenge for researchers to develop affordable and portable plasmonic biosensors capable of tracking fluorescence signals coupled with plasmonic resonance. Overcoming this challenge would enable the development of more accessible and versatile plasmonic

biosensing platforms, facilitating the integration of fluorescence tracking with plasmonic enhancements.

1.6 Coupling Fluorescence and Plasmonic Devices

The energy transfer mechanism of the fluorescence-plasmon coupling is influenced by the distance between fluorophore and plasmonic surface, the spectral overlap between fluorescence and plasmon, and the geometry of the plasmonic structure, such as the size of the nanoparticle [140]–[143]. The plasmonic response of the metallic nanostructures is determined by their size and shape, leading to two possible outcomes. In the case of small nanoparticles (less than 15 nm), electron scattering dominates, causing the plasmons to absorb incoming light and convert it into heat [140]. Alternatively, in larger structures, radiative damping dominates over plasmonic decay, allowing the plasmon to re-radiate to the far-field [140]. Depending on the size and shape of the metal nanostructure, the outcome of the light propagation differs.

The energy transfer between the fluorophore and surface plasmon is primarily influenced by the separation distance between them. When this distance falls within the range of ~1-10 nm, a non-radiative energy transfer occurs where no photons are emitted during the process. This type of energy transfer is described by the lossy surface waves. The lossy surface waves are surface trapped plasmons and their energy cannot be recovered as a useful signal [141]. As a result, the quenching of the fluorescence near the metal surface is observed due to the optical constrains formed at the short fluorophore-surface plasmon separation distance [141].

Instead of undergoing a non-radiative decay, both the signal of the plasmon and fluorescence can be enhanced near the metal surface. The electromagnetic description of the fluorescence enhanced-plasmonic radiation was briefly explained as the far-field radiation of fluorescence coupled plasmonic signal [140], [141], [144], [145]. This effect occurs after the separation distance increases up to a distance where the non-radiative lossy surface waves are no longer dominant over the plasmonic radiation. The reason of the enhancement is attributed to increase in the local incident field of fluorophore [146] and the modification of the local density of optical states (ρ_{LDOS}) within the cavity. ρ_{LDOS} is represented by the number of ways an electromagnetic wave can interact with the

fluorophore and is normalized to the incident intensity (Equation 1.1). Consequently, the overall radiation rate is enhanced compared to radiation in free space when the LDOS reaches its peak at the resonance wavelength.

$$\rho_{LDOS}(\omega) = |E_{loc}(\omega)|^2 \tag{1.1}$$

The fluorescence-coupled plasmonic radiation is amplified when the resonance of the plasmonic scattering or absorption spectrum aligns with the fluorescence spectrum, accompanied by changes in the LDOS [140], [147]. The enhancement and quenching of the fluorophore-coupled plasmonic radiation is also strongly influenced by the spectral overlap between the plasmonic resonance and the fluorescence spectrum. The spectral overlap region of the fluorescence spectrum (excitation/emission) determines the result between the fluorophore and metal-surface interaction. Fluorescence-coupled plasmonic radiation can be obtained by both coupling the excitation and emission spectrum with the fluorescence spectrum [148], [149]. In summary, achieving fluorescence-enhanced plasmonic radiation requires the optimization of the spectral overlap and separation distance. These factors should be carefully arranged together for maximizing the desired enhancement effects.

CHAPTER 2

2. ALZHEIMER'S DISEASE

Biosensors are analytical tools to enable us to understand diseases, thereby paving the way to diagnose a specific type of disease through biomarker and receptor interactions [150]. In this study, Alzheimer's Disease was chosen as the disease model to evaluate the biosensor performance of fluorescence-coupled plasmonic metasurfaces. The primary objective of the research was to develop a biosensor for early-stage diagnosis of Alzheimer's Disease through serum biomarkers. By utilizing fluorescence-coupled plasmonic metasurfaces as biosensors, the study remarked on the impact of dementia and aimed to address the existing challenges in POC platforms for Alzheimer's Disease diagnosis.

2.1 Dementia

Dementia is a broad definition that refers to a set of illnesses impacting cognitive skills such as memory, thinking, and the capacity to execute daily tasks. Dementia can be caused by several factors that damage nerve cells and harm brain over the time. This frequently results in a decrease in cognitive function (the ability of thinking) that is exceeding what would be expected from biological aging. Dementia impacts not only on the patients, but also it has social and financial implications for their caretakers, relatives, and the society. Insufficient consideration and comprehension of dementia frequently lead to stigmatization and challenges for the diagnosis and care of the condition. Dementia may arise due to a variety of neurodegenerative disorders or brain injuries that lead to direct or indirect harm. Alzheimer's disease is the most prevalent reason for dementia, accounting for more than half of the global dementia cases. However, the syndrome is additionally affected by additional disorders such as Lewy bodies and frontotemporal dementia. Other factors contributing to dementia include stroke, HIV infection, excessive alcohol consumption, repeated brain injuries, and nutritional

deficiencies. It is worth to note that different forms of dementia can coexist, including mixed forms resulting from multiple causes [151].

Moreover, statistically, dementia affects a significant number of individuals worldwide, with approximately 55 million cases in 2020 and nearly 10 million new cases emerging each year [152]. It stands as a leading cause of disability and dependency among elderly globally and ranks as the seventh leading cause of death overall. The economic impact of dementia is substantial, with global costs reaching 1.3 trillion US dollars in 2019.

2.2 Alzheimer's Disease (AD) and Neuropathology of AD

Dr. Alois Alzheimer, a notable neurologist, observed distinct abnormalities in the brain tissue of a deceased individual suffering from dementia. These abnormalities manifested as plaques and tangles [153]. Plaques, which are insoluble accumulations, were identified as aggregates of amyloid-beta (Aβ), a crucial peptide in the field of neuropathology. The amyloid precursor protein (APP) undergoes successive cleavages by β- and γ-secretases, forming various amyloid beta deposits with different amino acid sequences, ranging from 37 to 49 [154]. The most well-known variants are $A\beta_{40}$ and $A\beta_{42}$. Aβ peptides tend to misfold and form soluble oligomers, which aggregate into larger, insoluble fibrils. Over time, these fibrils accumulate into amyloid plaques (Figure 2.1 a). The neurotoxic nature of Aβ peptide is still under investigation, as multiple species have been identified [155]. However, their presence inside neurons has been linked to impaired cellular signalling [156] and synaptic plasticity [157], which can defect the functions of memory formation and retrieval in the brain.

The clearance of Aβ peptides by microglia also plays a significant role in the pathology of Alzheimer's disease (AD). However, the process of Aβ clearance can trigger the release of inflammatory cytokines and subsequent neurodegeneration. Moreover, microglia can phagocyte synapses further contributing to synaptic dysfunction and neuronal death [158], [159]. These abnormalities disrupt normal patterns of information stored in the brain.

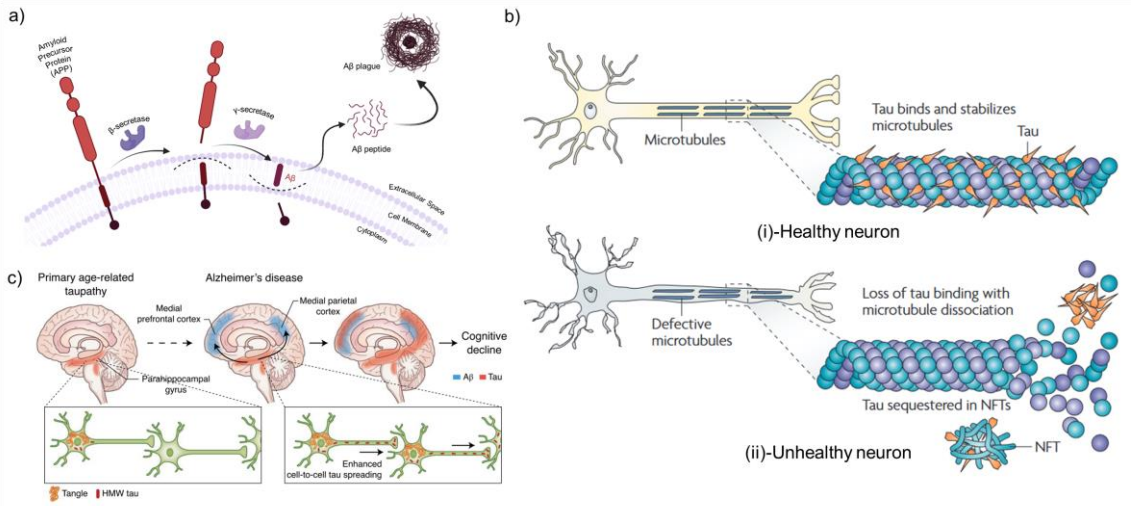

Figure 2.1: Neuropathological pathways of Aβ and tau. a) Cleavage of APP and Aβ plague formation (Created with Biorender®), b) comparison of healthy and unhealthy/modified tau proteins in microtubules, formation of NFT [160], c) cell-to-cell spread of tau and resulting cognitive decline [159].

Another pathological pathway of AD is tau—found in microtubules, which maintains the molecular transport within axons. In the context of AD, tau undergoes modifications, leading to the formation of aggregated structures known as neurofibrillary tangles (NFT) [160]. This disruption of molecular transport ultimately results in neuronal death (Figure 2.1 b). Additionally, tau has been observed to spread between neurons [159], causing the conversion of healthy tau proteins into modified forms and accelerating the progression of neuropathology (Figure 2.1 c). Overall, both Aβ and tau are widely accepted as pathological indicators of AD and utilized as biomarker profiles for the biological diagnosis of AD.

2.3 Biological Diagnosis of Alzheimer

Initially, AD was considered solely as a clinical syndrome, and the diagnosis has been made with only clinical symptoms without including neuropathological identification. There has been a movement, meanwhile, toward a biological explanation for AD as our understanding of the underlying molecular pathways has increased. The need for a more precise diagnostic approach to AD became vital as researchers realize the

relevance of identifying and intervening in the syndrome before the onset of symptoms during the preclinical phase. Regrettably, clinical settings often struggle with an accurate diagnosis, with approximately one in four patients receiving an incorrect diagnosis, making early detection of AD challenging [161].

The National Institute on Aging and the Alzheimer's Association (NIA-AA) established a set of diagnostic guidelines for staging AD patients in 2011 which assists the decision-making process and provides the framework for further research [162]. These guidelines introduced the concept of AD without symptoms, but with detectable biomarkers. Various biomarkers have since been utilized for the diagnosis of AD. Measuring Aβ42 or the Aβ42/Aβ40 ratio inside cerebrospinal fluid (CSF) or amyloid positron emission tomography (PET) imaging are available biomarkers for the detection of Aβ deposits [163]. The presence of aggregated tau, which forms neurofibrillary tangles (NFTs), can be detected using CSF phosphorylated tau or tau PET imaging [164]. Additionally, other biomarkers such as anatomic magnetic resonance imaging (MRI) [165], fluorodeoxyglucose (FDG) PET [166], and CSF total tau [167] have emerged, providing insights into neurodegeneration and neuronal injury.

Furthermore, in 2018, the NIA-AA proposed a new research framework called the ATN framework, which aimed to redefine and stage AD based on a purely biological perspective, integrating both asymptomatic and symptomatic stages. The ATN framework classifies biomarkers into three general groups: 'A' for Aβ plaques derived biomarkers, 'T' for NFT-originated biomarkers, and 'N' for neurodegeneration and neuronal injury-originated biomarkers [168], [169].

Conventional AD detection methods, such as CSF, MRI, and PET-based techniques, have shown to be useful for accurately diagnosing AD pathology. However, these methods have notable limitations. For instance, CSF collection through lumbar puncture is an invasive procedure and requires surgical skills [170], while imaging methods like PET and MRI are costly and they cannot be widely accessible, particularly in developing countries. As a result, these methods do not meet the RE-ASSSURED qualifications (detailed in Chapter 1) and their common clinical usage is limited in resource-scarce settings. Hence, there is a great and unmet need for the development of more affordable and less-invasive diagnostic platforms for AD.

In addition to collecting biomarkers from CSF, the utilization of blood biomarkers for AD diagnosis is a promising and emerging approach that reduces the invasiveness of specimen collection and allows for easy integration into existing immunochemical tests and biosensors, facilitating widespread AD diagnosis. Among the commonly used blood biomarkers for AD, plasma AB42/AB40, phosphorylated tau (p-tau), plasma neurofilament light (NfL), and plasma glial fibrillary acidic protein (GFAP) are prominent [171], [172]. However, a major challenge with these biomarkers is their extremely low concentrations (Figure 2.2 b) in blood due to their transfer through blood-brain barrier (Figure 2.2 a) [172]. Consequently, current detection methods for plasma biomarkers require high sensitivity, predominantly found in benchtop instruments like immunoprecipitation-mass spectrometry (IP-MS), enzyme-linked immunosorbent assay (ELISA), electrochemiluminescence immunoassays, single molecule arrays, and immune-infrared sensors [171], [173] . To advance the practicality of blood-based AD diagnosis, the development of more sensitive and accessible detection methods is crucial, enabling wider adoption and improving early detection and management of AD.

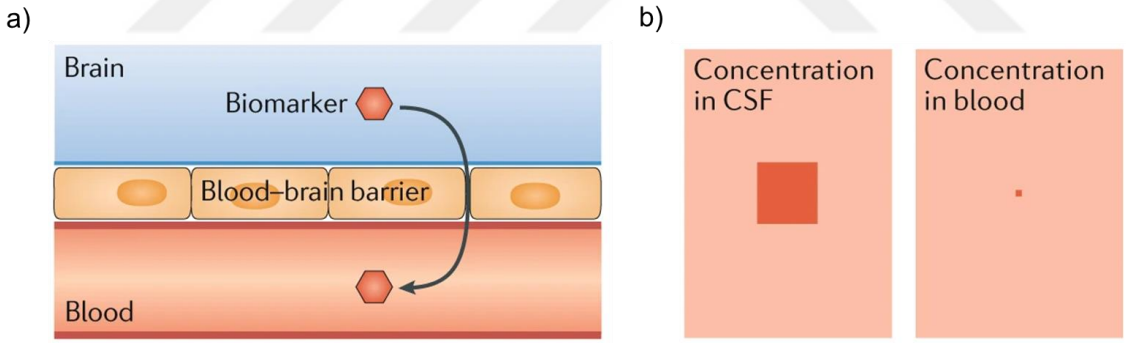

Figure 2.2: AD Biomarker mechanicm from brain to blood. a) The transfer of AD biomarkers through blood-brain barrier, b) the concentration drop in AD biomarkers during the transfer brom blood-brain barrier [172].

2.4 Aim of This Study

This study utilizes plasmonic metasurfaces coupled with fluorescence molecular emitters to construct hybrid (fluorescence and plasmonics) biosensors that demonstrate high sensitivity against targeted biomarkers, while being simultaneously scalable and

cost-effective. The geometry of the metasurface design is chosen as one-dimensional grating. These grating structures are readily found in DVDs, and they can be converted into a metasurface by coating thin metal films at nano-scale. Furthermore, the utilization of grating structure rather than a flat surface eliminates the requirement for a high-refractive index medium to facilitate momentum coupling between surface propagating plasmons and incident light, thereby minimizing more sophisticated optical set-up, including a prism to couple this momentum mismatch. DVD-templated metasurfaces are further combined with fluorescently conjugated surface modifications for obtaining hybrid plasmonic biosensors. The surface modifications are varied as short, medium, and long distances to control the separation distance between the plasmonic surface and fluorophore. The optimum surface modification is selected to maximize the signals. AD is used as a model disease for the biosensor, with $A\beta_{42}$ and tau serving as biomarkers. However, the biosensor can be adapted to detect any other disease and biomarkers by simply replacing the bioreceptor. The plasmonic signal is monitored using a portable spectrometer and light source, a 3D-printed optical setup, and a MATLAB-GUI interface. This thesis introduces a novel approach for coupling plasmonic metasurfaces and fluorescent molecules; provides a versatile strategy for adjusting the separation distance through surface modifications; and offers a cost-effective, scalable, and highly sensitive platform for the early diagnosis of AD.

CHAPTER 3

3. MATERIAL AND METHODS

3.1 Materials

Methanol, bovine serum albumin (BSA), and 3-Mercaptopropanyl-N-hydroxysuccinimide ester (3-MNHS) were purchased from Sigma-Aldrich (St Louis, MO, USA). Absolute ethanol, isopropanol, glycerol, and acetone were obtained from Isolab (Isolab, Istanbul, Turkey). Avidin-FITC, avidin-Texas Red, streptavidin-Qdot 525, streptavidin-Qdot 625, and normal human serum were purchased from Invitrogen (Carlsbad, CA, USA). Phosphate Saline Buffer (PBS) tablets were obtained from Biomatik (Ontario, Canada). SH-PEG-Biotin (Molecular Weight, MW: 600) and SH-PEG-Biotin (MW: 2000) were purchased from NANOCS (New York, NY, USA). The Human Tau colorimetric ELISA kit was purchased from Novus Biologicals (Cambridge, UK). Recombinant Tau-441 (2N4R), Biotin-anti-Tau (189-195), and Human β-Amyloid Peptide (1-42) were obtained from Biolegend (San Diego, CA, USA). The Amyloid beta 42 Human ELISA kit, biotinylated beta-Amyloid (1-42) polyclonal antibody, and avidin were purchased from Thermo Scientific (Waltham, MA, USA). HP (Palo Alto, CA, USA) brand DVD-R discs were used as the grating substrate for plastic-templated metasurfaces. Gold (999.9) and silver (999.0) metals were obtained from Istanbul Gold Refinery (Istanbul, Turkey). All chemicals were used without any pre-processing, and water was supplied as distilled water from the UNAM facility.

3.2 FDTD Simulation of the Metasurface

The optical response of a DVD-templated metasurface was simulated using finite-difference time domain (FDTD) numerical software (Lumerical, Ansys) (Canonsburg, PA, USA). The simulation involved a three-dimensional grating structure of the

metasurface with specific dimensions (width = 450 nm, height = 25 nm, and period = 730 nm). The metasurface was composed of different layers on a substrate, including polycarbonate (n = 1.58), followed by titanium (10 nm), silver (30 nm), and gold (15 nm). The optical properties of the metal layers were determined using Palik's model for titanium [174] and Johnson and Christy's model for silver and gold [175]. The simulation used periodic boundary conditions in the x-direction, symmetrical conditions in the y-direction, and perfect matched layer conditions in the z-direction. A plane wave with p-polarization was employed as the light source, and refractive indices for both air (n = 1) and water (n = 1.33) were considered. The absorption spectrum of the metasurface was obtained by multiplying the normalized intensity of the reflection spectrum with the utilized lamp (OSL2IR, 400 - 1750 nm) (Thorlabs, Newton, NJ, USA) intensity, and then, subtracting the result from one (Equation 3.1).

$$1 - R = A + T, \qquad T = 0 \tag{3.1}$$

3.3 Plasmonic Metasurface Fabrication

Optical discs (DVDs) were chosen as a material for generating the required grating structure in this study. DVDs offer several advantages, including their availability, affordability, stability, and lack of brittleness, eliminating the need for complex surface patterning techniques such as lithography or nanoimprinting. DVDs consist of multiple layers: a polycarbonate (PC) substrate, a reflective layer, a recording layer, and a protective layer (Figure 3.1a). HP brand DVD-R model is utilized for DVD-templated metasurface fabrication in this study.

Initially, in order to prepare the PC substrate for the grating structure, the top protective layer is carefully separated from the underlying PC layer using a knife (Figure 3.1b). The resulting PC grating structure was then treated with an ethanol and methanol mixture (1:1) to remove the reflective layer. Subsequently, a chemical etching process was performed for 60 seconds to modify the nanoperiodicity (width, height, and slope). To harness the plasmonic properties, the PC substrate was coated with titanium (5 nm), silver (30 nm), and gold (15 nm) using a thermal evaporator (MiDAS PVD 3T, VAKSIS, Ankara, Turkey) (Figure 3.1c). Metal sources were evaporated using tungsten boats

(Midwest Tungsten Service) (Willowbrook, IL, USA) and the tooling factor of this instrument was individually optimized with the assistance of an optical interferometer for each material. Finally, the DVD metasurface was later cut into smaller pieces via scissors for the next step, i.e., the microfluidic integration (mostly 15 mm x 15 mm).

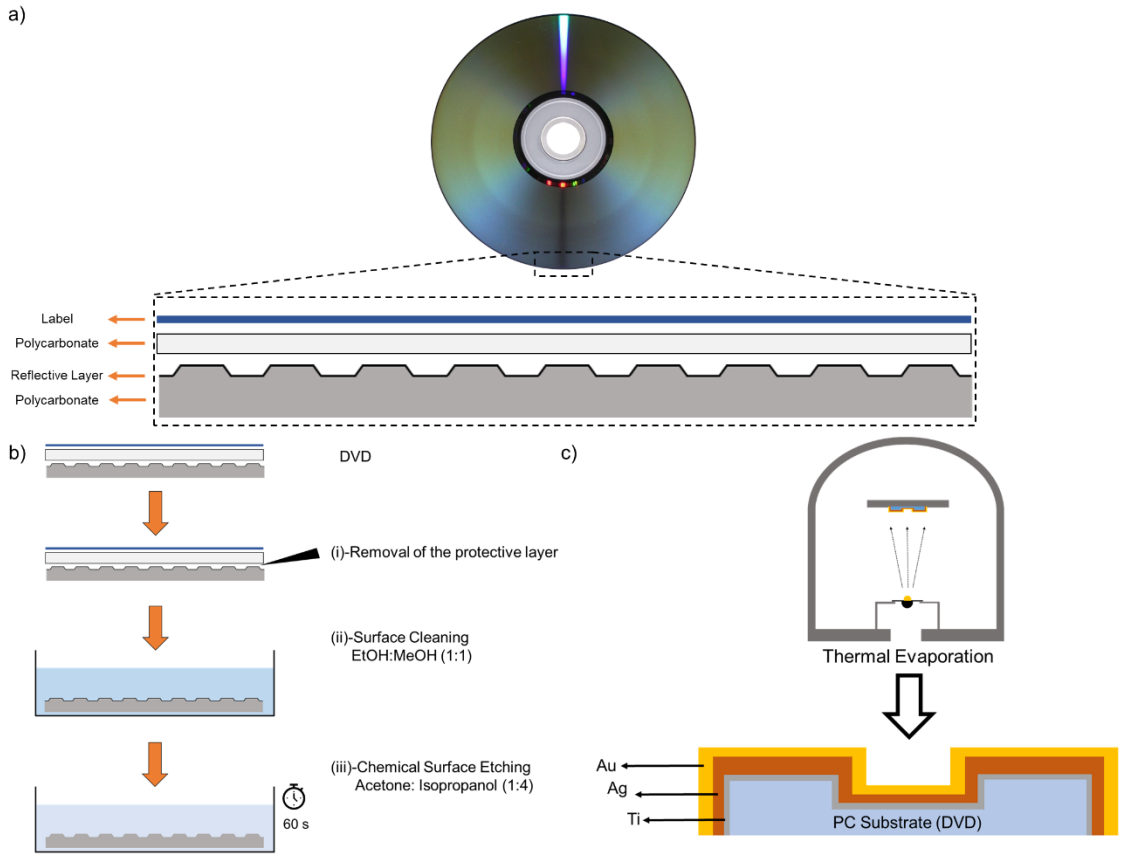

Figure 3.1: DVD-templated metasurface Fabrication. a) DVD layers, b) DVD substrate cleaning and chemical etching, and c) thermal evaporation of DVD substrate.

3.4 Microfluidic chip preparation

Microfluidic chips were produced via a non-lithography method, i.e., laser-cutting the substrates. Poly (methyl methacrylate) (PMMA, 2 mm of thickness) was chosen as the top transparent layer of the microfluidic channel, and a double-sided adhesive (DSA, 50 μm of thickness) layer was selected as the adherence layer between the metasurface and PMMA, thereby forming the channels on the metasurface. The design parameters

were drawn using RDWorks software (Thunder Laser, Dongguan City, Guangdong Province, China) and accordingly, DSA and PMMA were cut into desired shapes with a laser cutter (LazerFix) (Konya, Türkiye). A stretched hexagon was chosen as the shape of the microfluidic chamber, which was patterned (%15 power and 100 m/s speed) onto the DSA layer (Figure 3.2a, Right). Inlet and outlet holes were patterned (%40 power and 40 m/s leaser head speed) onto the PMMA layer for providing a continuous flow inside the microfluidic channel (Figure 3.2a, Left). The entire microfluidic chip was finalized by assembling PMMA, DSA, metasurface, tubing and syringe tips (Figure 3.2b). The tubings were attached to the PMMA inlet and outlet holes via epoxy (Pattex) (Henkel, Düsseldorf, Germany). For adjusting the flow inside the microfluidic channels in a controlled manner, a syringe pump (New Era Pump Systems Inc.) (Farmingdale, NY, USA) was utilized. The sampling and washing flow rates were both determined as 10 µL/min for keeping shear stress along the surface minimum and increasing the possibility of linker attachment to the metasurface.

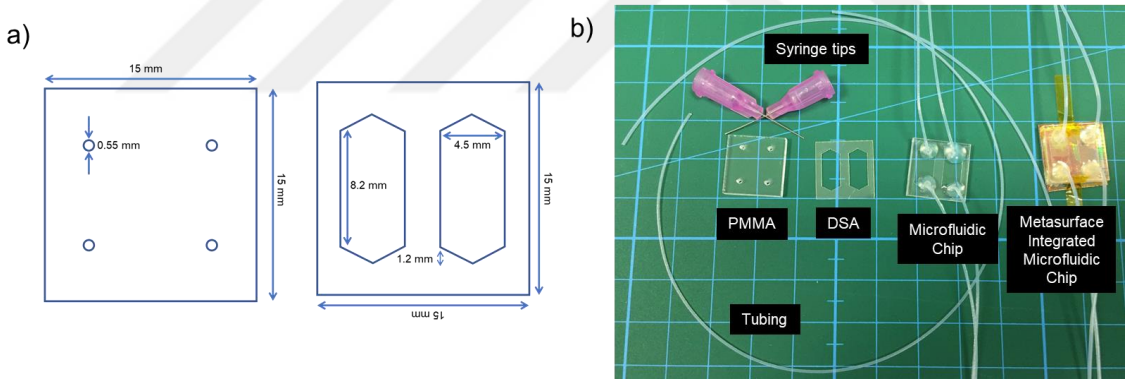

Figure 3.2: Integration of metasurface with microfluidic chip. (a) Schematic representation of the microfluidic chip design, with the left side showing the PMMA design and the right side illustrating the DSA design. (b) Components of the microfluidic chip and final assembled design.

3.5 Optical Setup and Software Interface for Data Measurement

While measuring the signals, we focused on the collection of reflected light through normal illumination from metasurface. In this regard, we monitored plasmonic resonance within the UV-VIS spectrum through a portable and in-house-built optical setup. This setup consists of three main components: (i) a portable Czerny-Turner charge-coupled device (CCD) spectrometer (CCS175/M, 500-1000 nm) (Thorlabs, Newton, NJ, USA), (ii) a fiber-coupled incoherent light source (OSL2IR, 400 - 1750 nm) (Thorlabs, Newton, NJ, USA), (iii) various optical components including aspheric lenses (A240, Thorlabs) (A240-A, Thorlabs) (Newton, NJ, USA), beam splitter (BS010, Thorlabs) (Newton, NJ, USA), linear polarizer (LPVISC050, Thorlabs) (Newton, NJ, USA) aperture (SM1D25, Thorlabs) (Newton, NJ, USA), and cosine corrector (CCSA1, Thorlabs) (Newton, NJ, USA) that were integrated into a 3D printed platform, and a real-time in-house data acquisition interface (MATLAB GUI code that flawlessly works together with Thorlabs OSA commercial software) [176].

Initial measurements were conducted using either distilled water or PBS, which provided a background signal. Once the background signals were collected, the analyte of interest was introduced into the chip. The binding of the analyte to the surface resulted in a change in the resonance signal, which was observed as a wavelength shift over time, represented by an association curve. Eventually, the association curve reached to a stable point, pointing out the saturation level of binding. To remove non-binding analytes from the surface, a washing step (either distilled water or PBS) was performed. The difference in wavelength between the background and after the washing step indicated the corresponding change in resonance signals at the measured point, which was then correlated to the concentration of the analyte applied.

3.6 Bulk Refractive Index Sensitivity Measurements

In order to assess the sensitivity, the metasurface was exposed to increasing concentrations of glycerol solutions (1%-70%). The absorbance measurements of the

glycerol concentrations were measured via the optical setup and the sequential increasing glycerol concentration formed a ladder-type plot with a red-shifted response. The total wavelength shift between water (0% of glycerol) and the highest glycerol concentration (70%) was utilized for the measurement of refractive index sensitivity (S) and figure of merit (FOM) values. These values were utilized as conventional performance metrics for the assessment of plasmonic platforms [177].

3.7 Surface Modifications

Different than conventional plasmonic measurements, plasmonic enhanced fluorescence was strategized in this study. In this manner, the separation distance between the fluorophores and metasurface was critical to enhance plasmonic signals on the metasurface. Hence, three different surface modifications were utilized for the integration of fluorescence conjugated proteins onto the metasurface. The configurations include three distinct linkers: (i) 3-MNHS as short-distance surface modification, (ii) thiol-PEG 600-Biotin as medium-distance surface modification, and (iii) thiol-PEG 2000-Biotin as long-distance surface modification.

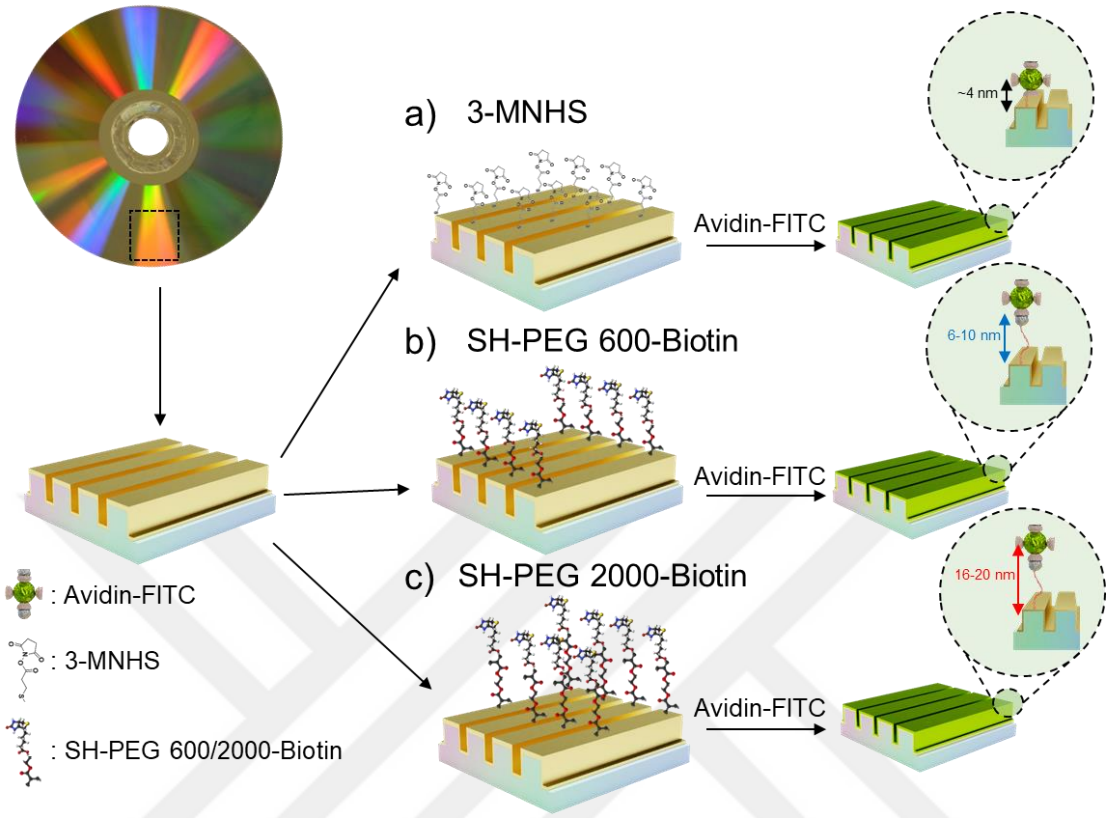

Figure 3.3: The surface modifications with different lengths. Short (3-MNHS), medium (SH-PEG-600-Biotin), and long (SH-PEG 2000-Biotin) are demonstrated from top to bottom.

The estimated length values of these linkers were ~4 nm, ~6-10 nm, and ~16-20 nm for short, medium, and long-distance modifications, respectively. These values were calculated using the size of avidin protein and the corresponding linker molecules. Briefly, 3-MNHS was negligibly smaller than the size of avidin protein. Therefore, the separation distance for short-distance modification was dominantly designated by the size of avidin, which is approximately 4 nm [178] (Figure 3.3. Short). The size of the avidin protein was determined using the Dynamic Light Scattering (DLS) method, yielding a measurement of 6.4 ± 1.1 nm. This value closely aligns with the literature value [178]. The length of medium and long-distance modifications was determined mostly by the molecular weight of the PEG polymer. The correlation between PEG molecular weight and the length of the polymer is determined in the following equation, where n is the number of repeating ethylene glycols [179] (Equation 3.2).

$$\mathrm{PEG}_{MW} = 18.02 + (44.05\ x\ n) \quad (3.2)$$

The size of each ethylene glycol changed between 0.278-0.358 depending on the molecular orientation [180]. By finding the n and multiplying it by the size of single ethylene glycol, the length of PEG polymers (MW=600 and MW=2000) was calculated. For instance, the molecular weight of PEG polymer is 600, and n is calculated as 13 units. The length of repeating 13 ethylene glycols is calculated as 3.61-4.65 nm. By implementing an avidin protein (~4 nm), the linker becomes 7.61-8.65 nm, representing ~6-10 nm (Figure 3.3, Medium). Likewise, the long-distance modification is calculated as 16.7-21.9 nm, pointing out ~16-20 nm (Figure 3.3, Long).

The surface modifications were performed by the following procedure. Briefly, 3-MNHS was prepared in ethanol solution (10 mM) and applied to metasurface by dip coating it over 12 hours at dark conditions. The thiol group at the end of 3-MNHS provides a dative metal bond between gold layer and sulfur atoms. The succinimide groups provide covalent immobilization of fluorophore conjugated proteins by amide linkages [181]. Both medium and long-distance modifications were prepared in distilled water (10 mM) and applied for 15 minutes of microfluidic flow (10 µL/min). These linkers were attached to the gold layer of metasurface via metal dative linker as same as with short-distance modification. Biotin group at the end of the linkers provided a connection element for the fluorophore conjugated proteins via avidin-biotin interactions. All of the surface modifications were self-assembled onto the metasurface. Once all the surface modification was achieved, the sensors were washed with distilled water for the further experiments.

3.8 Fluorophore Integration

Fluorophores (FITC, Texas Red, Qdot 525, and Qdot 625) were obtained as conjugated with either avidin (avidin-FITC and avidin-Texas Red) and streptavidin (streptavidin-Qdot 525 and streptavidin-Qdot 625). The fluorophore conjugated proteins bind to the surface modifications by amide-succinimide (short-distance modification) or avidin-biotin (medium and long-distance modifications) interactions. They were applied on top of surface modifications for either 3200 seconds (~53 minutes through 10 µL/min

of flow rate, avidin-FITC and avidin-Texas Red) and 600 seconds (5 minutes through 10 μL/min of flow rate, streptavidin-Qdot 525 and streptavidin-Qdot 625) depending on the association of the protein and the availability of material.

3.9 Antibody Integration

The antibodies (biotinylated anti-beta-Amyloid,1-42, polyclonal antibody) (Thermo Scientific) (Waltham, MA, USA) (biotinylated anti-Tau, 189-195) (Biolegend) (San Diego, CA, USA) were readily conjugated with biotin molecules for providing a binding with fluorophore conjugated avidin proteins. These antibodies (10 μL of volume and 25 μg/mL in PBS) were individually applied onto fluorophore conjugated avidin molecules through the microfluidic chamber via micropipettes, and they were then incubated at 4°C for overnight.

3.10 Biomarker Detection

In this study, recombinant Tau-441 (2N4R) (Biolegend) (San Diego, CA, USA) and Human β-Amyloid Peptide (1-42) (Biolegend) (San Diego, CA, USA) biomarkers were captured using a modified surface that integrated antibodies. Before the measurements, the solution inside microchannels were changed with PBS, and therefore, the background signal and washing step was conducted with PBS. The biomarkers were then applied to the sensor surfaces at a flow rate of 10 μL/min for a duration of 20 minutes. Additionally, the biomarkers were also studied in biological fluids, i.e., specifically normal human serum (Invitrogen) (Carlsbad, CA, USA). In this case, the surface was initially treated with BSA (1% prepared in PBS) for 20 minutes at a flow rate of 10 μL/min to prevent any non-specific binding. After this step, biomarkers were introduced to the sensors.

3.11 ELISA

Enzyme Linked-Immuno-Sorbent Assay (ELISA) is a high-throughput and quantitative biochemical tool for the detection of targets in biological specimens [182]. It

is a widely used tool in clinical diagnosis and considered as the gold standard for biomarker detection [183], [184]. The principle of ELISA depends on specific binding between target molecule and antibody as a recognition element. The assay is consisted of immobilized antibodies and signaling enzymes. The most common type of ELISA is solid phase sandwich method. In this study, two different ELISA kits (Amyloid beta 42 Human ELISA Kit, Thermo Scientific, Waltham, MA, USA; Human Tau colorimetric ELISA Kit, Novus Biologicals, Cambridge, UK) were used, each one specific to a single AD biomarker, tau-441 and aβ 1-42. Both of the kits involved mainly similar application procedure.

3.11.1 Aβ ELISA Kit Protocol

The 96 wells of Amyloid beta 42 Human ELISA kit (Thermo Scientific) (Waltham, MA, USA) were precoated with Aβ 1-42 specific capture antibodies (Figure 3.4. step I). Per the manufacturer's protocol, 50 µL of the standards, controls, and the unknown specimens were initially added into capture antibody immobilized wells (Figure 3.4. step II). Then, 50 µL of detection antibody was introduced to the wells for forming a sandwich structure (Figure 3.4. step III). The plate was then incubated for 3 hours at room temperature with a constant shaking. After the incubation, the wells were aspirated and washed with washing buffer for 4 times. Later, 100 µL of horseradish peroxide conjugated anti-Rabbit immunoglobulin G (IgG HRP) antibody was further added to the wells and incubated for 30 minutes at room temperature for completing three-member sandwich to four-member with secondary antibody. During each incubation step the wells were covered with a seal to prevent solvent evaporation. The excessive amount of IgG HRP was removed from the wells by aspiration and following washing step. Then, 100 µL of stabilizing chromogen—a compound that change color during oxidation, was added to the wells and incubated at room temperature at dark conditions for 30 minutes. This step enabled to remove the unbound HRP enzymes and produced a blue color with the bound enzymes (Figure 3.4. step IV). After the incubation, 100 µL of stop solution was added to the wells, which was later finalized color production, and the color turned from blue to yellow (Figure 3.4 step V). The absorbance values of the wells were measured at 450 nm using a plate reader (SpectraMax M5, Molecular Devices) (San Jose, CA, USA). The

color intensity inside wells presented a biomarker concentration proportional with the mean intensity of wells.

3.11.2 Tau ELISA Kit Protocol

The 96 wells of Human Tau colorimetric ELISA kit (Novus Biologicals) (Cambridge, UK) were precoated with tau-441 specific capture antibodies (Figure 3.4. step I). Similar to previous protocol, 100 µL of the standards, the controls, and the samples were added into separate wells (Figure 3.4. step II). After the addition, the plate was covered and samples were incubated at 37°C for 90 mins. Then, the wells were aspirated and 100 µL of biotinylated detection antibodies were added to the wells without any washing (Figure 3.4. step III). The plate was covered and incubated for an hour at 37°C. After incubation, the wells were aspirated and 350 µL wash buffer was applied to the wells for 3 times. 100 µL of HRP conjugated avidin proteins were added to the wells (Figure 3.4. step IV). Then, plate was covered and incubated for 30 minutes at 37°C. After incubation, the wells were again aspirated and washed for five times (350 µL wash buffer). 90 µL of enzyme substrate was added and incubated for 15 minutes at 37°C after the plate was sealed. Then, 50 µL of stop solution was added to each well (Figure 3.4. step V). Lastly, the optical density values of the wells were measured at 450 nm using a plate reader (SpectraMax M5, Molecular Devices) (San Jose, CA, USA).

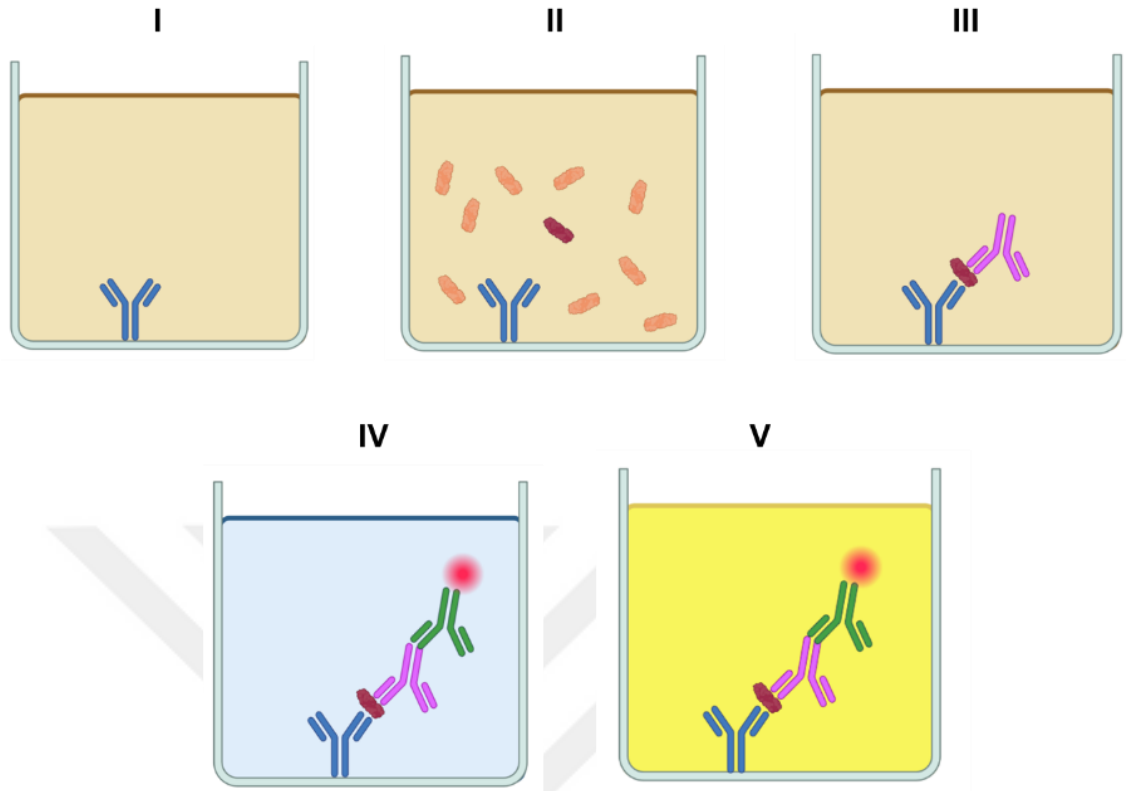

Figure 3.4: Main steps of the ELISA protocols: (I) immobilized capture antibody, (II) target addition, (III) addition of detection antibody, (IV) addition of HRP, and (V) target concentration specific color change (Created with Biorender®).

3.12 Characterization Methods

Characterization methods were applied for analyzing surface modifications, antibodies, separation distance, and fluorescence behavior of the protein conjugated surface modifications. The chemical investigation of surface modification was determined using X-ray Photoelectron Spectroscopy (XPS) and Fourier-Transform Infrared Spectroscopy (FTIR). The chemical investigation of antibodies was determined using FTIR. The separation distance was characterized using Atomic Force Microscopy (AFM) and Laser Scanning Confocal Microscopy (LSCM). The fluorescence spectrum of the fluorophore conjugated proteins was obtained using Time Resolved Fluorescence (TRF). The fluorescence images were captured using epifluorescence upright fluorescence microscope.

3.12.1 Fluorescence Image Acquisition and Analysis

The fluorescence intensity measurements of the conjugated proteins were measured with an epifluorescence upright fluorescence microscopy (Axio Observer, ZEISS) (Jena, Germany). In the system, a LED source with 475 nm (%20 intensity) was utilized for the excitation of avidin-FITC (Invitrogen) (Carlsbad, CA, USA) . The images were taken with 100x objective and 150 ms exposure time, and then, analyzed using Image J (National Institutes of Health, NIH) (Stapleton, NY, USA) software. The images of fluorescent proteins were isolated inside a 4x4 pixels region of interests (ROIs) after background subtraction (rolling ball radius: 50 pixels). The mean intensity values of 5 similar ROIs from each surface modifications were extracted using histogram analysis and compared with each other.

3.12.2 Fluorescence Spectra Measurement

The excitation and emission spectra of fluorophore-conjugated avidin proteins including avidin-FITC, avidin-Texas Red, streptavidin-Qdot 525, and streptavidin-Qdot 625) were characterized using Time-Resolved Fluorescence (TRF) (Fluorolog 3 FL-1057, HORIBA JVON, Edison, NJ, USA). The instrument employed a broad-spectrum Xenon lamp with a maximum emission at 467 nm. To determine the precise excitation and emission spectra of the conjugated proteins, company provided maximum excitation and maximum emission wavelengths were initially used as the estimated values. The estimated excitation maximum values were then used to measure the emission spectrum, and the resulting maximum emission wavelength was used to measure the excitation spectrum. The acquired excitation maximum wavelength was compared with the initial estimate. If they were not equal, the initial estimate was updated, and the process of finding emission spectrum was repeated. This process was continued until estimated excitation/emission maximum values became equal with the measured excitation/emission maximum values.

3.12.3 Dynamic Light Scattering (DLS) Analysis of Proteins

The size of avidin protein was measured using DLS instrument (Zetasizer Nano ZS, Malvern Panalytical) (Malvern, UK). This method determines the diffusion rate of the particles inside a solution using the fluctuation in the intensity of the scattered light. The fluctuation provides information over Brownian motion of the particles which is further correlated to a fit model. The model describes the hydrodynamic diameter, shape, and interactions of the particles with the surrounding medium. To accurately measure the particle sizes, the equipment used a blue color laser with a wavelength of 488 nm to scatter the particles. However, this laser wavelength caused emission from the fluorophore-conjugated particles, leading to misleading information over the size of conjugate proteins. Therefore, for the purpose of this study, only the control avidin protein was measured to avoid any confounding effects caused by the fluorophore conjugation. For the determination of the size of the avidin protein (100 nM), particle size distribution (Number PSD) and protein characterization software tools were utilized (Zetasizer Nano, Malvern Panalytical) (Malvern, UK). The data were plotted according to the Gauss Fit.

3.12.4 X-Ray Photoelectron Spectroscopy Analysis of Surface Modifications

The surface modifications were chemically investigated using X-Ray Photoelectron Spectroscopy (XPS) (K-Alpha, Thermo Scientific) (Waltham, MA, USA). Briefly, XPS is a widely used surface-sensitive analytical technique for the investigating chemistry formed on the surfaces [185]. The method relies on analyzing the kinetic energy of photoelectrons, which are emitted from the sample surface upon the impact of X-rays. Detected kinetic energies provide the essential information regarding to the chemical composition and chemical states of the studied surface. In this study, surface modifications, i.e., short, medium, and long-distance, on the metasurface were investigated. Herein, a comprehensive XPS survey was conducted, and individual spectrum peaks associated with Carbon (C), Oxygen (O), Sulfur (S), Nitrogen (N), and

Gold (Au) were also analyzed. The samples were prepared following the procedure described in the section of 3.7 Surface Modifications, and they were subsequently dried inside an oven at 40°C for an hour. Additionally, a flood gun was activated during the XPS analysis to neutralize any charges that may have built up on the metasurface during the analysis. For the data analysis, the peaks were first shifted according to the C 1s peak before conducting any data analysis. To determine the peak information related to different elements, a peak deconvolution method was applied.

3.12.5 Fourier Transform Infrared Spectroscopy Analysis of Surface Modification and Immobilized Antibodies

FTIR provides information over the chemical groups, chemical bonds and molecular vibrations found on the sample, by recording the transmitted or absorbed infrared light [186], [187]. In this study, attenuated total reflection (ATR) integrated FTIR instrument (Nicolet is50, Thermo Fisher) (Waltham, MA, USA) was utilized. ATR (Attenuated Total Reflection) provides direct surface analysis by utilizing the evanescent wave interaction between a crystal, such as diamond, and sample surface[188] . ATR simply eliminates the need for extensive sample preparation, and it is well-suited for surface characterization [189]. The FTIR spectrums of medium-distance modification (SH-PEG-600-Biotin, NANOCS) (New York, NY, USA), avidin-FITC (Invitrogen) (Carlsbad, CA, USA), and biotinylated anti-Tau (189-195) (Biolegend) (San Diego, CA, USA) were analyzed using the transmission mode. The samples were prepared following the procedure described in the sections of 3.7 Surface Modifications, 3.8 Fluorophore Integration, and 3.9 Antibody Integration. The results were averaged over 32 scans.

3.12.6 Contact Angle Analysis of Surface Modification and Antibody Immobilization

Contact angle measurements were utilized for evaluating surface wettability and analyzing the interaction between surface and water for studying the wetting behavior of surface chemistry, roughness, and coatings [190], [191]. The angle between the surface and water drop designates the hydrophilic or hydrophobic behavior of the surface [192]. In this study, the wetting behavior of surface modification and immunoassay was investigated using the contact angle instrument (OCA 30, DataPhysics Instruments) (Filderstadt, Germany) integrated with a sessile drop technique, which measures the contact angle formed at the interface phase boundary of liquid, solid, and air [193]. The wetting behaviors of medium-distance modification (SH-PEG-600-Biotin, NANOCS) (New York, NY, USA), avidin-FITC (Invitrogen) (Carlsbad, CA, USA), biotinylated anti-Tau (189-195) (Biolegend) (San Diego, CA, USA), and BSA (Sigma-Aldrich) (St Louis, MO, USA) integrated metasurfaces and bare metasurface were analyzed using sessile drop technique. For the technique, 5 μL of water was drop casted on the surface of the samples and the contact angles were measured using the instrument software. Each measurement was repeated for three times for obtaining accurate results. The samples were prepared following the procedure described in the sections of 3.7 Surface Modifications, 3.8 Fluorophore Integration, and 3.9 Antibody Integration.

3.12.7 Topography Analysis of Surface Modification and Antibody Immobilization (AFM, SEM and LSCM)

Scanning Electron Microscopy (SEM) and Atomic Force Microscopy (AFM) methods were utilized for surface imagining of the bare metasurface. SEM utilizes focused beams to excite inelastic scattering induced secondary electrons for generating high resolution and high depth of field images of micro and nanostructures [194]. The bare metasurface was imagined using SEM (Quanta 200 FEG, Field Electron and Ion Company, FEI) (Hillsboro, OR, USA) for observing the periodic structure. As the

metasurface is conductive, there was no need to apply a sputtering process for the analysis.

As a brief, AFM is a widely used high-resolution imaging technique, where a scanning probe is employed to visualize and analyze micro and nanostructures [195]. AFM offers diverse applications, including topography analysis [196], force spectroscopy [197], lithography [198], and even biosensing [199]. The scanning probe in AFM interacts with the sample surface, enabling precise imaging and characterization at the nanoscale.

Laser Scanning Confocal Microscopy (LSCM), on the other hand, eliminates out of focus light and provides non-destructive high lateral and axial resolution [200]. LSCM (VKX-100, Keyence) (Itasca, IL, USA) was used for the roughness analysis of the medium-distance modification (SH-PEG-600-Biotin, NANOCS) (New York, NY, USA), avidin-FITC (Invitrogen) (Carlsbad, CA, USA), biotinylated anti-Tau (189-195) (Biolegend) (San Diego, CA, USA), and BSA (Sigma-Aldrich) (St Louis, MO, USA) integrated metasurfaces and bare metasurface.

Both AFM and LSCM images were analyzed using open-source Gwyddion visualization software (Czech Metrology Institute, Czechia) [201] for analyzing the images, line profiles and surface roughness.

3.12.8 AFM Scratch of Surface Modification and Antibody Immobilization

In this study, the resultant film thicknesses due to antibody immobilization and surface modification on the metasurfaces were measured using Atomic Force Microscope (AFM) in contact mode. The experiment involved scratching the metasurface with an AFM tip to assess the change in height before and after the scratching process. This test has been used in the literature to determine the film thickness on contact mode AFM [202]. The metasurfaces employed in the study were comprised of silicon substrate metasurface, medium-distance modification (SH-PEG-600-Biotin, NANOCS) (New York, NY, USA), avidin-FITC (Invitrogen) (Carlsbad, CA, USA), Biotin-anti-Tau (189-195) (Biolegend) (San Diego, CA, USA), and BSA (Sigma-Aldrich) (St. Louis, MO,

USA). To ensure accurate measurements, the AFM scratch was applied on a silica substrate metasurface rather than on the original plastic-templated metasurfaces. The silica substrate was used due to the periodicity and roughness of plastic-templated metasurfaces, which can hinder precise measurements. The fabrication procedure for this metasurface was similar to that described in section 3.2 (Plasmonic Metasurface Fabrication), but a silicon wafer was used instead of a DVD. The AFM used in the study was a contact mode AFM (MFP-3D, Asylum Research, Oxford Instruments) (Abingdon, United Kingdom). The AFM operating parameters were adjusted for the scratching test. The changes were made to the Z voltage, deflection value, and scanning speed. The deflection value and Z voltage were updated to 3.5 and -10 V, respectively, to apply sufficient force to the surface during scratching. The scanning speed was reduced to 1.0 Hz to ensure precise scratching and measurement. On the other hand, the scratching tests were conducted over a distance ranging from 500 nm to 1 μm. AFM images were acquired from a 5 μm x 5 μm area for each test.

3.13 Statistical Analysis

The surface modification and biomarker detection results were analyzed using one-way Analysis of Variance (ANOVA) and Multivariate Analysis of Variance (MANOVA). For MANOVA analysis, Minitab Data Analysis software (Minitab) (State College, PA, USA) was utilized.

CHAPTER 4

4. FLUORESCENCE COUPLED PLASMONIC METASURFACES

4.1 Topographic Characterization of Metasurfaces

The topography of the metasurface was analyzed using SEM and AFM. The general observation of the metasurface was initially demonstrated with SEM (Figure 4.1 a-b), and the captured images designated a uniform surface periodicity of the grating structures at different scales. The height and period measurements of the metasurface was then performed using AFM (Figure 4.1 c-e). The measurements stated that the metasurfaces had ~769 nm of period and ~76.4 nm of height (Figure 4.1 e). The obtained height and period measurements provided structural information for the design parameters of electromagnetic simulation. Although DVD surfaces have generally 740 nm of periodicity, we measured this range more than expected. Approximately 4% of variations in measuring periodicity through AFM might be due to the scanning of small area, tip radius or potential issues in the calibration process.

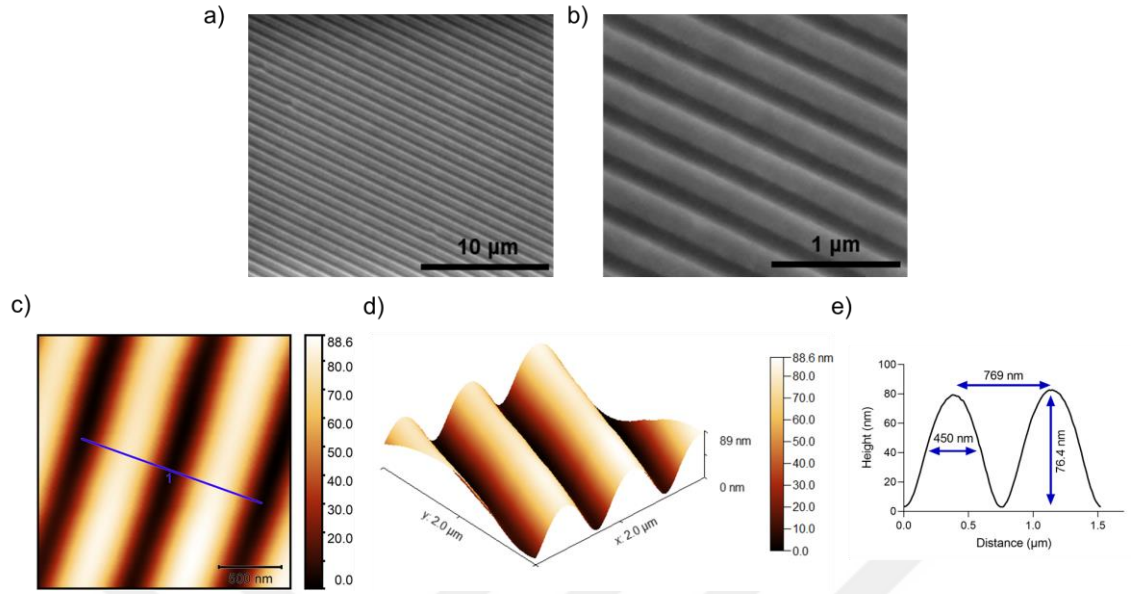

Figure 4.1: Topographic analysis. a) SEM image of the metasurface. b) Uniform periodicity of the metasurface. c) Images taken from AFM analysis (scale bar: 500 nm). d) 3D representation of the grating on the metasurface using AFM acquired data. e) Height and period measurements between two adjacent gratings.

4.2 Numerical Understanding of Plasmonic Response from Metasurface

The plasmonic response of the metasurface was determined using both numerical (FDTD) and experimental analysis. The results regarding the FDTD and experimental analysis were stated in the following sections.

4.2.1 Electromagnetic Simulation of the Metasurface

At the first glance, the metasurface was computationally studied to investigate the reflection and absorption spectrum of the metasurface. The metallic layers were arranged on a polycarbonate (n=1.58) grating structure in the order of titanium (10 nm), silver (30 nm), and gold (15 nm). The structural parameters were set as 730 nm of period, 25 nm of height, and 450 nm of width for the simulations (Figure 4.2 c). The simulated period and height values differed from AFM measurements since the simulated rectangle and conical AFM measurements had different geometries. Therefore, the period and height

parameters of the simulation were optimized until a peak was observed that closely matched the experimental results.

The numerical model pointed out a resonance peak at 575 nm on the course of applying water medium (n=1.33), which was associated with the metasurface plasmonic resonance. This numerical resonance output was compared with the experimental result, where the fabricated metasurface exhibited a resonance peak at 552 nm in water medium (n=1.33) (Figure 4.2 a). While the peak wavelengths showed similarities, the numerical model indicated a lower intensity of the plasmonic resonance and differed from the experimentally acquired the plasmonic resonance intensity. Furthermore, the behavior of the numerically obtained reflection spectra at different media, specifically air (n=1) and water (n=1.33), was also investigated (Figure 4.2 b). In the air medium (n=1), a sharp dip at 776 nm was determined; however, there were no plasmonic resonance was observed between 550 nm and 650 nm. In contrary, the metasurface in water medium exhibited a plasmonic dip at 575 nm, aligning with the absorption peak. An electromagnetic field enhancement of 11 (λ= 575 nm and n=1.33) was observed at the tips of grating structures, where they were formed an electromagnetic hot spot (Figure 4.2 d). The simulation results provided a critical understanding of the absorption and reflection spectrums on different mediums, and highlighted the distribution and enhancement of electromagnetic field on the metasurface.

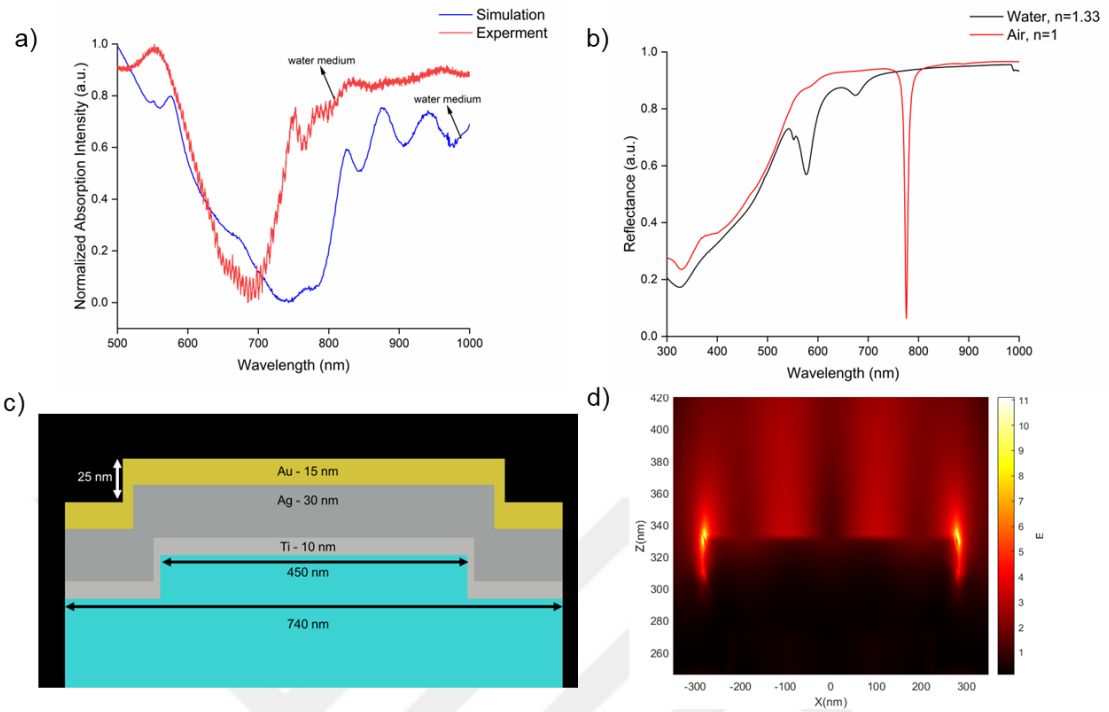

Figure 4.2: The results of the numerical modeling of metasurface plasmonic resonance. a) Normalized absorption spectrum plots in water medium (n=1.33), obtained from the experimental and numerical results. b) The reflectance spectrum of the simulated metasurface at water (n=1.33) and air (n=1) medium. c) A cross-sectional representation of the simulated metasurface. d) Electromagnetic field intensity distribution on the metasurface (λ=575 nm).

4.2.2 Bulk Sensitivity of the Metasurface

The bulk sensitivity of the metasurface was experimentally investigated using various concentrations of glycerol solutions, ranging from 1% to 70%. Since these solutions had different refractive index values, we were able to assess the metasurface's sensitivity. In order to monitor the real-time changes in resonance wavelength, a portable optical setup was utilized. The plasmonic resonance peak of the metasurface exhibited a red-shift in wavelength and a decrease in optical intensity while increasing the glycerol concentrations (Figure 4.3 a). The resonance wavelength revealed an average stepwise red-shift of 36.6 nm from water (0% glycerol) medium to 70% of glycerol concentration (Figure 4.3 b). As a note, this value slightly varied with each metasurface fabrication, typically falling within a range of ± 3 nm. Averaged values (based on 100 data points

from each concentration) for each glycerol concentration were obtained and fitted using a linear regression model (Figure 4.3 c).

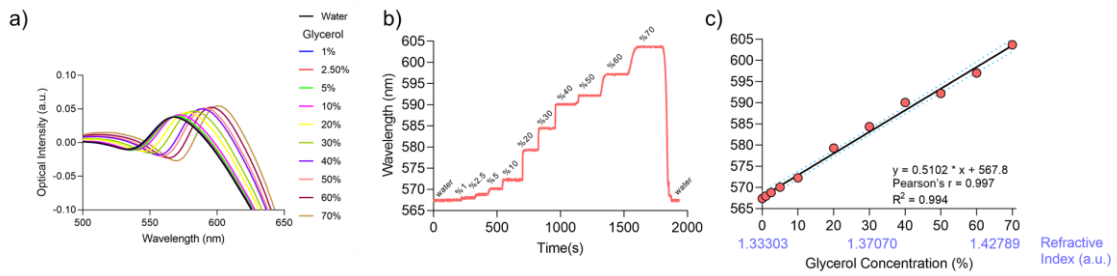

Figure 4.3: Refractive index dependent resonance changes on the metasurface. a) Absorption spectra of water and glycerol solutions (%1 - %70). b) Real-time changes in resonance wavelength with the respect to medium refractive index. c) The linear regression of average peak values of each glycerol solution.

On the other hand, refractive index sensitivity (S) is a critical optical parameter employed to quantify the bulk refractive index sensitivity of a plasmonic sensor [203]. It is calculated as the change in the plasmonic resonance divided by the corresponding change in the refractive index (Equation 4.1). In addition, the Figure of Merit (FOM) is another crucial metric to assess overall performance and sensitivity of an optical sensor. It is defined as the ratio of S to full width half maximum (FWHM) of the plasmonic resonance peak (Equation 4.2) [204]. FWHM—an indicator of the line width of resonance peak, is inversely proportional to the sensitivity and performance of the plasmonic sensor. As an example, higher FOM and S values indicate a better ability to track minute changes in the refractive index of the surrounding medium. Accordingly, the FOM values of the metasurface was calculated for each glycerol concentration as FWHM was changing for each change in the refractive index of the medium (Table 4.1).

$$\text{Refractive Index Sensitivity } (S) = \frac{\Delta\lambda}{\Delta n} \tag{4.1}$$

$$\text{FOM} = \frac{S}{FWHM} \tag{4.2}$$

Table 4.1: FWHM and FOM values of the metasurface for each glycerol concentration.

Glycerol Concentrations (%)	Refractive Index (RIU)	FWHM (nm)	FOM (1/RIU)
0	1.333	30.54	12.54912
1	1.334	30.28	12.65687
2.5	1.336	29.14	13.15202
5	1.339	28.58	13.40973
10	1.345	27.97	13.70218
20	1.358	27.32	14.02818
30	1.371	26.94	14.22606
40	1.384	26.01	14.73472
50	1.398	25.45	15.05894
60	1.413	24.9	15.39157
70	1.428	23.92	16.02216

4.3 Surface Modifications

The coupling effects between fluorescence and surface plasmon polaritons (SPPs) were determined upon two factors: (i) the seperation distance between metasurface and fluorophores, and (ii) the degree of spectral overlap between SPPs and fluorescence excitation/emission spectrum [205]. In this study, the separation distance was controlled by using three different surface modifications of varying separation distance through 3-MNHS (short), SH-PEG 600-Biotin (medium), and SH-PEG 2000-Biotin (long), providing ~4-6 nm, ~6-10 nm, and ~16-20 nm of estimated lenghts, respectively.

Briefly, at short-distance modification (~4-6 nm of separation distance), the FITC induced oscillations in the metal surface might form lossy surface waves that can not radiate to the far-field, wave propagation away from its source [141]. These lossy surface waves were described as the non-radiative energy dissipation of trapped plasmons to the metal surface via interband absorptions and decay of the plasmon radiations as heat instead of the far-field radiation. This energy transfer also quenches the fluorophore intensity which is found in the close vicinity of the metal surface by long-range dipole

and surface plasmon interaction [141], [206]. The rate of energy transfer between fluorophore and surface plasmons was inversely proportional to the seperation distance between fluorophore and metal surface with an exponential factor [141]. Considering the lengths of the medium (~6-10 nm) and the long-distance (~16-20 nm) modifications, these lossy surface waves that enables non-radiative energy transfer between metal surface and fluorophore might be replaced by the far-field plasmon radiation [207]. The change in the plasmonic resonance and the fluorescence intensity can provide critical information about the energy transfer via the integration of various surface modifications over the metasurface.

The effect of the seperation distance on the plasmonic resonance was investiaged using surface modifications on the metasurface and fixing a single fluorophore conjugated avidin protein (avidin-FITC). Avidin-FITC was compared with avidin proteins on short, medium, and long-distance modifications. In this manner, the effect of fluorescence signal on different separation distances was investigated by the changes in plasmonic resonance wavelength. The addition of avidin protein led to an average of 2.32 ± 0.08 nm wavelength shift at short-distance modification (3-MNHS, 100 nM), this value was decreased to 1.24 ± 0.09 nm by the addition of avidin-FITC (Figure 4.4 a). The presence of FITC decreased the normalized wavelength shift around 1.17 times when compared with solely avidin (Figure 4.4 g-h). This decline in wavelength shift implied that the presence of FITC non-radiatively coupled with the plasmonic radiation. The reason of this signal drop was suggested by the non-radiative energy transfer between fluorophore and surface plasmons at the height of short-distance modification (~4 nm) (Figure 4.4 b). The mean of plasmonic wavelength shift for avidin protein on the medium-distance modification (SH-PEG 600-Biotin, 1nM) was measured as 0.45 ± 0.14 nm, and this value was increased to 2.03 ± 0.11 nm when avidin-FITC was applied to medium-distance modification instead of avidin (Figure 4.4 c). The normalized wavelength shift increased in the presence of FITC around 4.4 times of signal enhancement on medium-distance modification (Figure 4.4 g-h). This result suggested the fluorescence-enhanced plasmonic signal formation on medium-distance modification which was attributed to the FITC induced far-field plasmonic radiation at ~6-10 nm separation distance (Figure 4.4 d). The avidin protein on long-distance modification caused a mean wavelength shift of 0.1 ± 0.11 nm, while avidin-FITC designated 0.88 ± 0.15 nm (Figure 4.4 e). The

normalized wavelength shifts was increased ~2.7 times in the prescence of FITC on long-distance modification (Figure 4.4 g-h). Likewise, this result was comparable to the fluorophore-enhanced plasmonic signal enhancement obtained at medium-distance modification. Overall, the highest signal enhancement was observed on the medium-distance modification. This result implied that the coupling effect between fluorophore and surface plasmons reduced while the length increased between ~6-10 nm and ~16-20 nm (Figure 4.4 f).

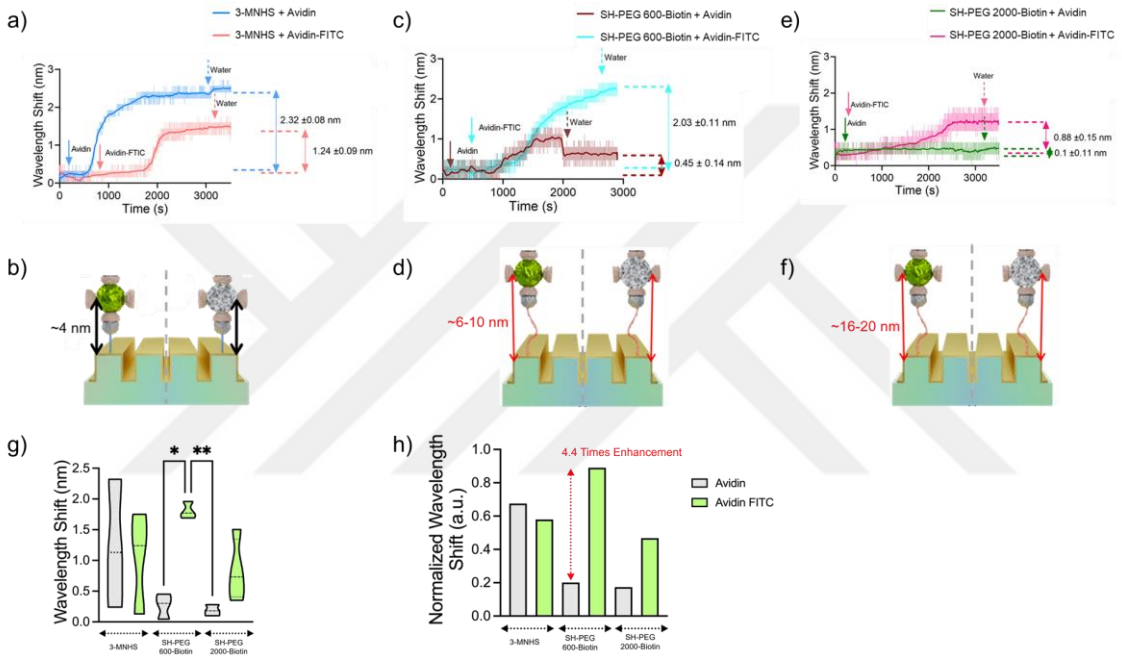

Figure 4.4: The plasmonic investigation of avidin and avidin-FITC on short, medium, and long-distance modifications. The mean plasmonic resonance shift of a) short, c) medium, and e) long-distance modifications. The representation of avidin-FITC (on left) and avidin (on right) on b) short, d) medium, and f) long-distance modifications. g) Comparison of wavelength shift values and h) normalized mean data of short, medium, and long-distance modifications. The statistical analysis was performed using a non-parametric Kruskal-Wallis analysis, and the statistical difference between data groups was shown as* $p<0.05$ and ** $p<0.01$.

4.4 Spectral Overlap Between Fluorescence and SPPs

The largest wavelength shifts in the presence of avidin-FITC were obtained while applying the medium-distance modifications that exhibit an fluorescence-enhancement over the plasmonic resonance through the coupling of fluorescence-SPPs. On the other hand, the spectral overlap between fluorescence excitation/emission and plasmonic resonance is also critical for utilizing the coupling effect between fluorescence most effectively and ultimately achieving the highest plasmonic resonance shifts [208], [209]. To investigate the spectral overlap between the plasmonic resonance and the fluorescence spectrum, different fluorophore-conjugated avidin and streptavidin proteins were used on medium-distance modification by keeping avidin protein as the control. Avidin-FITC, avidin-Texas Red, streptavidin-quantum dot 525 (Qdot 525), and streptavidin-Qdot 625 were utilized as conjugate proteins with medium-distance modifications.

4.4.1 Fluorescence Spectrums of Fluorophore Conjugated Proteins

Initially, the fluorecence spectrum of the fluorophore conjugated avidin and streptavidin proteins were individually measured using TRF, and their spectral overlaps with plasmonic resonance were compared accordingly.

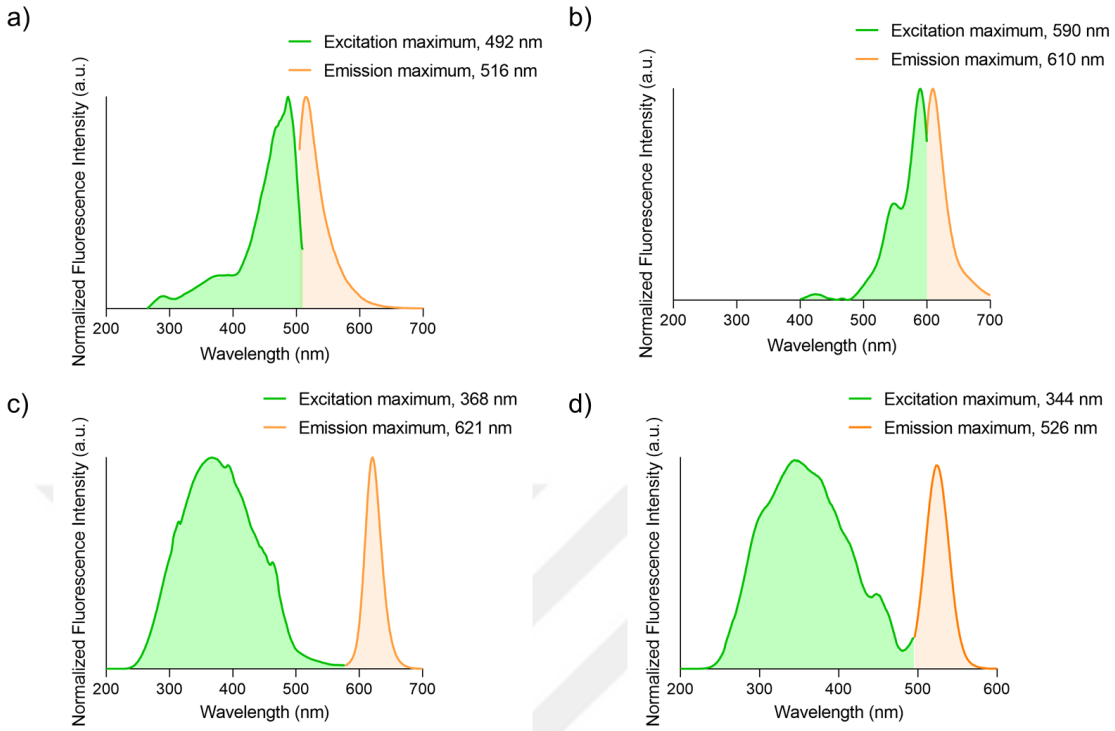

Figure 4.5: The normalized fluorescence spectrum of avidin conjugates. a) the fluorescence spectrum of avidin-FITC, b) avidin-Texas Red, c) streptavidin-Qdot 625, and d) streptavidin-Qdot 525.

Briefly, avidin-FITC displayed an excitation maximum at 492 nm and an emission maximum at 516 nm (Figure 4.5 a). Avidin-Texas Red exhibited an excitation maximum at 590 nm and an emission maximum at 610 nm (Figure 4.5 b). Streptavidin-Qdot 625 revealed an excitation maximum at 368 nm and an emission maximum at 621 nm (Figure 4.5 c). Streptavidin-Qdot 525 had an excitation maximum at 344 nm and an emission maximum at 526 nm (Figure 4.5 d). The emission spectra of avidin-FITC and avidin-Texas Red were broader than those of streptavidin-Qdot 525 and streptavidin-Qdot 625. Moreover, the excitation spectra of avidin-FITC and avidin-Texas Red were narrower than those of streptavidin-Qdot 525 and streptavidin-Qdot 625. These variances in the spectra were expected to potentially impact over the spectral overlap of plasmonic resonance. Considering the observations at the vicinity of plasmonic resonance, the excitation maximum of avidin-Texas Red and the emission maximums of avidin-FITC, avidin-Texas Red, streptavidin-Q dot 525, and streptavidin-Qdot 625 were estimated to couple with the plasmonic resonance of the metasurface (Figure 4.6).

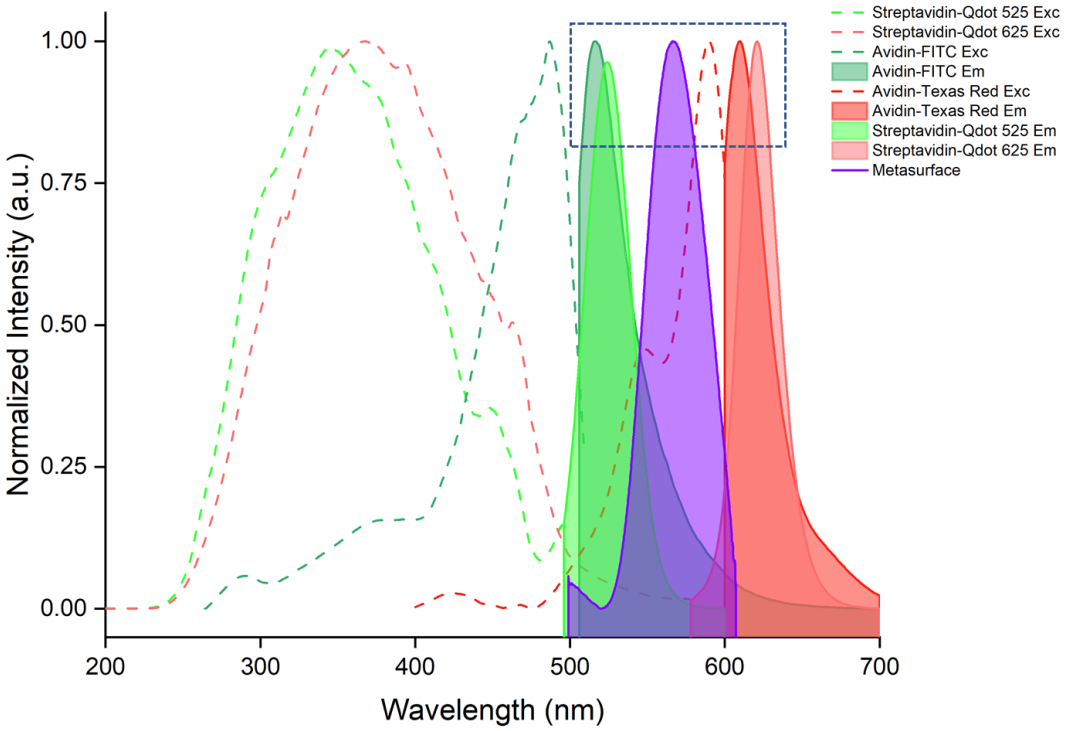

Figure 4.6: The spectral overlap between plasmonic resonance and the excitation and emission spectra of avidin-FITC, avidin-Texas Red, streptavidin-Qdot 525, and streptavidin-Qdot 625. The Blue dotted rectangle represented the estimated coupling region.

4.4.2. Plasmonic Response to the Changes in Spectral Overlap

The inclusion of fluorophore conjugated avidin and streptavidin proteins were adsorbed onto the biotin molecules in the case of the medium-distance modification. For investigating the spectral overlap changes, the surface modification was decided as the medium-distance modification (SH-PEG 600-Biotin).

Firstly, avidin-Texas Red (100 nM) was integrated on the medium-distance modification (Figure 4.7 a). The addition of avidin-Texas Red caused a mean wavelength shift of 0.57 ± 0.0.4 nm (Figure 4.7 b). Compared to the wavelength shift (0.45 ± 0.14 nm) of avidin on medium-distance modification, the wavelength shift through avidin-Texas Red determined ~1.3 times signal enhancement. This value was much smaller than

the avidin-FITC induced signal enhancement, ~4.4 times, and avidin-FITC demonstrated 2.5 times higher plasmonic signal enhancement than avidin-Texas Red(Figure 4.7 d). This result suggested that the excitation spectra of avidin-Texas Red (excitation maximum, 590 nm) coupled with SPPs and showed a lower $\rho_{LDOS}(\omega)$ value at plasmonic resonance wavelength (~550-570 nm) than avidin-FITC.

The integration of streptavidin-Qdot 525 (1 nM) and streptavidin-Qdot 625 (1 nM) (Figure 4.7 e) over medium-distance modification performed -0.35 ± 0.18 nm and -0.88 ± 0.58 nm blueshifts, respectively (Figure 4.7 f-g). The reason of blueshift observation instead of redshift was explained by the gain and longer lifetime properties of Qdots under broadband light source excitation [139]. The gain property of Qdots amplified the intensity of light on the metasurface and contributed to a negative local index change. The normalized plasmonic response of avidin was 5.1 and 1.8 times higher than streptavidin-Qdot 525 and streptavidin-Qdot 625, respectively (Figure 4.7 h). This result showed that the presence of Qdot-conjugated streptavidin proteins failed to achieve an optimum spectral overlap between the fluorescence spectrum and plasmonic resonance. The highest plasmonic signal enhancement, resulting in optimal spectral overlap, was observed while utilizing avidin-FITC with a medium-distance modification.

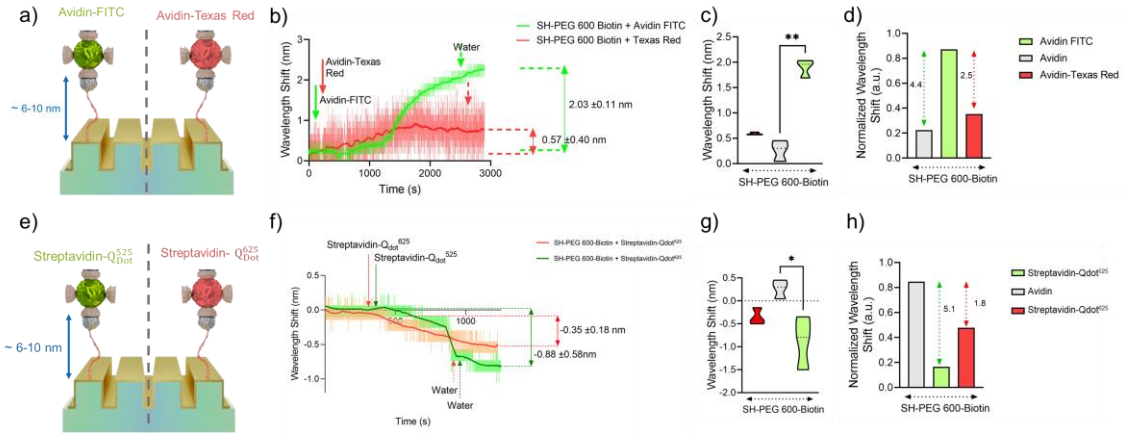

Figure 4.7: The spectral overlap between fluorescence and plasmonic signals was investigated using different fluorophore conjugates of avidin and streptavidin. a) Seperate integrations of avidin-FITC and avidin-Texas Red on medium-distance modification, b) Mean wavelength redshift values of avidin-FITC and avidin-Texas Red, c) Comparison of wavelength shift values, and d) normalized mean redshift data of avidin control, avidin-

FITC, and avidin-Texas Red. e) Separate integrations of streptavidin-Qdot 525 and streptavidin-Qdot 625 on medium-distance modification. f) Mean wavelength blueshift values of streptavidin-Qdot 525 and streptavidin-Qdot 625 and avidin-Texas Red. g) Comparison of wavelength shift values and h) normalized mean wavelength shift data of avidin control, streptavidin-Qdot 525, and streptavidin-Qdot 625. The statistical analysis was performed using a non-parametric Kruskal-Wallis analysis, and the statistical difference between data groups was shown as* $p<0.05$ and ** $p<0.01$.

4.5 Fluorescence Investigation of Fluorophore Coupled Metasurfaces

The distance dependant energy transfer between fluorophore and surface plasmon waves also alters the fluorescence intensity by the application of each surface modification [210]–[213]. Therefore, the change in of fluorescence intensity over the surface modifications (short, medium, and long-distance) was investigated using a fluorescence microscopy. Medium-distance modification provided the highest mean value of fluorescence intensity, followed by long- and short-distance modifications. The normalized fluorescence intensity of medium-distance modification was ~3.68 and ~2.61 times higher than short- and medium-distance modifications, respectively (Figure 4.8 a-b). This result was interpreted as the appearance metal enhanced fluorescence at medium-distance modification (Figure 4.8 d) with the respect to long- and short-distance modifications. The short-distance modification showed the lowest fluorescence intensity (Figure 4.8 c, i), suggesting the formation of lossy surface wave induced non-radiative energy transfer between metasurface and fluorescence. This result quenched the fluorescence intensity with the respect to medium- (Figure 4.8 c: ii) and long-distance (Figure 4.8 c: iii) modifications. The long-distance modification provided a fluorescence enhancement over the short-distance modification; yet, this was not strong as observed in the presence of medium-distance modification.

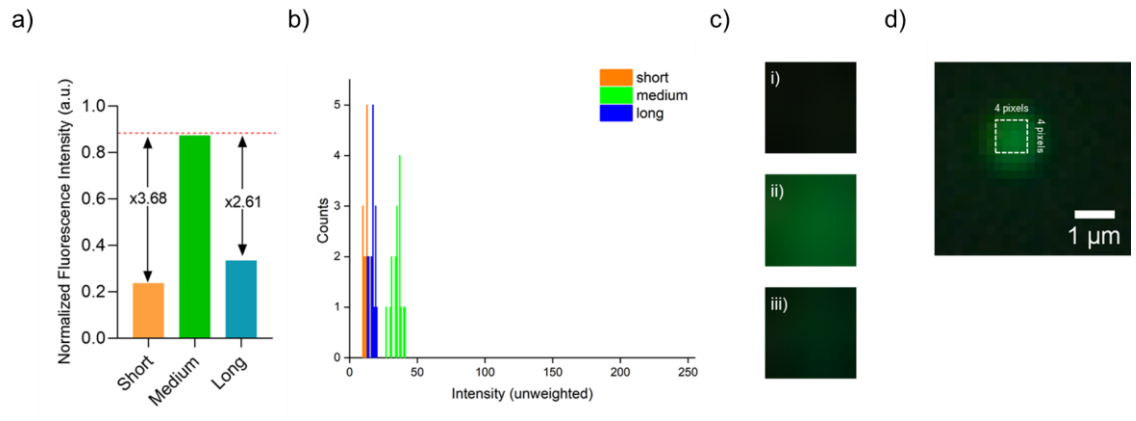

Figure 4.8: Fluorescence intensity measurements of avidin-FITC over surface modifications. a) Normalized fluorescence intensity comparisons of avidin-FITC over short, medium, and long-distance modifcations. b) Histogram values of avidin-FITC over short, medium, and long-distance modifications. c) 4x4 pixels sized Reigon of Interests (ROIs) of avidin-FITC proteins on short, medium, long-distance modifications. d) A single ROI of avidin-FITC on medium-distance modification.

Both the fluorescence intensity and the plasmonic resonance shift were found to be highest for the medium-distance modification, followed by long- and short-distance modifications, respectively. This suggests that both the fluorophore-enhanced plasmonic signal enhancement and metal-enhanced fluorescence were achieved most effectively with the medium-distance modification.

The fluorescence measurements showed the adsorption of the surface modifications over the metasurface. To investigate the coverage of fluorescence emitters (avidin-FITC) on medium-distance modification, the fluorescent intensity of the metasurface was analyzed before (bare DVD), during and after washing steps of avidin-FITC (Figure 4.9). The washing step was employed for preventing the analysis of non-adsorbed avidin-FITC proteins.

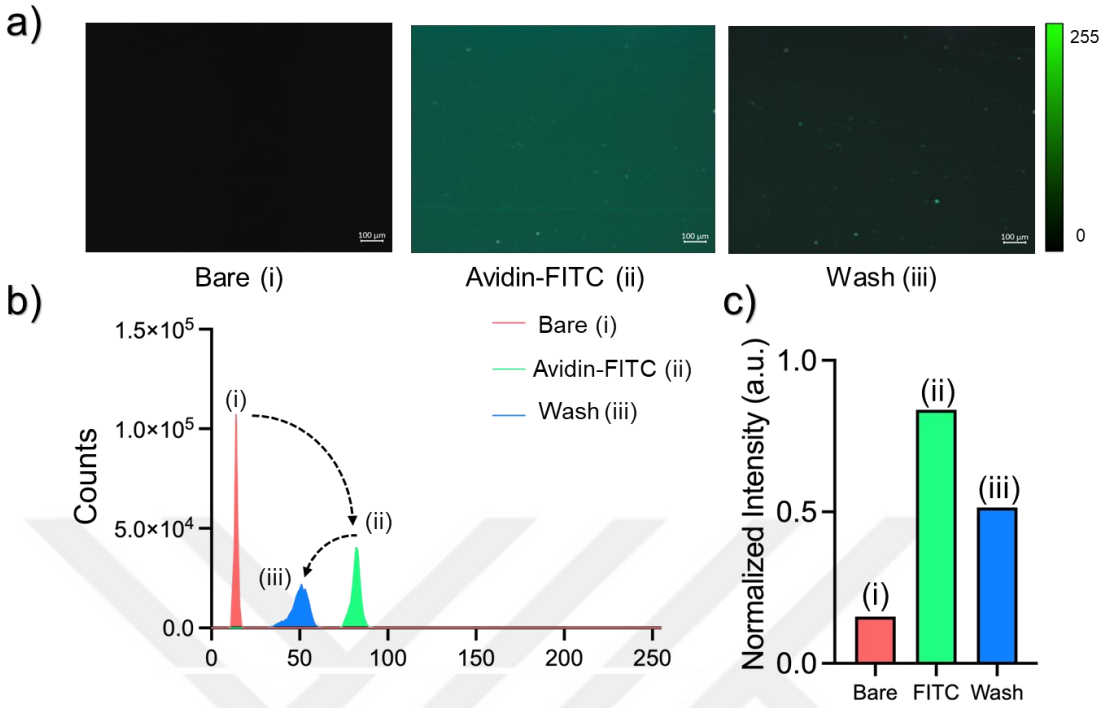

Figure 4.9: The fluorescence intensity investigation of avidin-FITC by the comparison of bare, avidin-FITC addition and after washing steps. a) Fluorescence images of bare (i), avidin-FITC (ii), and wash (iii) steps. b) Histogram plot of the steps combined. c) Normalized fluorescence intensity of bare (i), avidin-FITC (ii), and wash steps (iii).

The fluorescence intensity values of the bare DVD, avidin-FITC, and wash steps were compared with each other (Figure 4.9 a-b). The normalized fluorescence intensity values were 0.84, 0.51, and 0.15 for the steps of avidin-FITC addition, washed surface, and bare DVD, respectively (Figure 4.9 c). This indicated %60 of recovery in terms of fluorescence intensity after washing the surface, pointing out that the medium-distance modification was sufficiently covered with avidin-FITC. This was especially critical for maximizing the surface area of avidin-FITC molecules, which were subsequently functionalized with biotinylated antibodies to capture biomarkers in future experiments (Chapter 5).

4.6 XPS Characterization of the Surface Modifications

The elemental investigation of the surface modifications on the metasurface was demonstrated by using XPS analysis. In this study, C 1s, O 1s, N 1s, S 2p, and Au 4f regions of the binding energy spectrum were analysed for the surface modifications. Briefly, short-distance modification was formed by two different functional groups, thiol ending mercaptopropane group and N-hydroxysuccinimide (NHS) ester group. The C 1s results revealed the carbon bindings of C-C and/or C-H at 284.13 eV, C-N and/or -C-O-C at 284.13 eV and -C=O at 285.98 eV (Figure 4.10 a). The -C=O, C-O-C, C-N bindings were associated with NHS ester group which verifies the presence of surface modification on the metasurface. The O 1s scans revealed C=O and -C-O-C- bindings at 533.33 eV and 531.80 eV (Figure 4.10 b), respectively which were consistent with C 1s results. On the other hand, the N 1s results did not provide sufficient intensity to fit a peak (Figure 4.10 c). The metal dative bond formed between gold and sulphur (Au-S) was observed at 162.96 eV and the C-S bond was observed at 164.28 eV (Figure 4.10 d). The gold surface associated Au (0) $4f_{7/2}$ and Au (0) $4f_{5/2}$ peaks were observed at 87.21 eV and 83.53 eV (Figure 4.10 e). The obtained results represented the 3-MNHS adsorption on the metasurface and the peak informations were consistent with the literature [214]–[216]. The C 1s (43.85 %) possessed the highest atomic ratio of the short-distance modification followed by, O 1s (21.44 %), S 2p (8.89 %), and N 1s (0.65%).

The medium-distance modification consisted of PEG polymer chain (MW: 600 Da), thiol group and biotin molecule. The C 1s results were collected at 286.79 eV, 285.51 eV, and 284.07 eV for the associated bindings of C=O, -C-O-C, and C-C/C-H, respectively (Figure 4.10 g). The O 1s scans provided peaks at 531.82 eV and 530.22 eV for C=O and -C-O-C, respectively (Figure 4.10 h). The C=O groups were found on the biotin molecule [217] and the observed peaks on C 1s and O 1s were confirming its presence. The -C-O-C- groups were found at the backbone of PEG. The O 1s and C 1s peaks were complementary each other. The N 1s scan resulted with a peak at 398.8 eV (Figure 4.10 i) which was associated with amide group in biotin molecule [218], [219]. The S 2p scans demonstrated characteristic peaks at 162.65 eV and 161.25 eV for Au-S and S-C bonds, respectively (Figure 4.10 j). The peaks were associated with the thiol group found at the end of medium-distance modification. Au (0) $4f_{7/2}$ and Au (0) $4f_{5/2}$

were found at 86. 84 eV and 83.27 eV, respectively (Figure 4.10 k). The Au 4f results were similar with short-distance modification and showing the presence of metallic Au bond on the metasurface. Similar to short-distance modification, the C 1s (48.68 %) was determined as the highest atomic ratio on the medium-distance modification followed by, O 1s (14.17 %), S 2p (6.57 %), and N 1s (2.75%).

The long-distance modification was consisted of the same functional groups on medium-distance modification, instead the PEG polymer had longer ethylene glycol backbone (MW: 2000 Da). The C 1s results were collected at 287.15 eV, 285.54 eV, and 283.93 eV for the associated bindings of C=O, -C-O-C, and C-C/C-H, respectively (Figure 4.10 m). The O 1s scans provided peaks at 531.83 eV and 530.23 eV for C=O and -C-O-C, respectively (Figure 4.10 n). The biotin associated C 1s and O 1s peaks were on similar positions with the medium-distance modification. The N 1s scan resulted with a peak at 398.8 eV (Figure 4.10 o). The S 2p scans demonstrated characteristic peaks at 161.37 eV and 160.15 eV for Au-S and S-C bonds, respectively (Figure 4.10 p). Au (0) $4f_{7/2}$ and Au (0) $4f_{5/2}$ were found at 86. 84 eV and 83.27 eV, respectively (Figure 4.10 p). The results were similar with medium-distance modification. Likely medium-distance modification, the C 1s (48.68 %) was observed as the highest atomic ratio of the long-distance modification followed by, O 1s (14.17 %), N 1s (3.87 %), and S 2p (2.22%). Overall, these results verified successful immobilization of the surface modifications onto the metasurface.

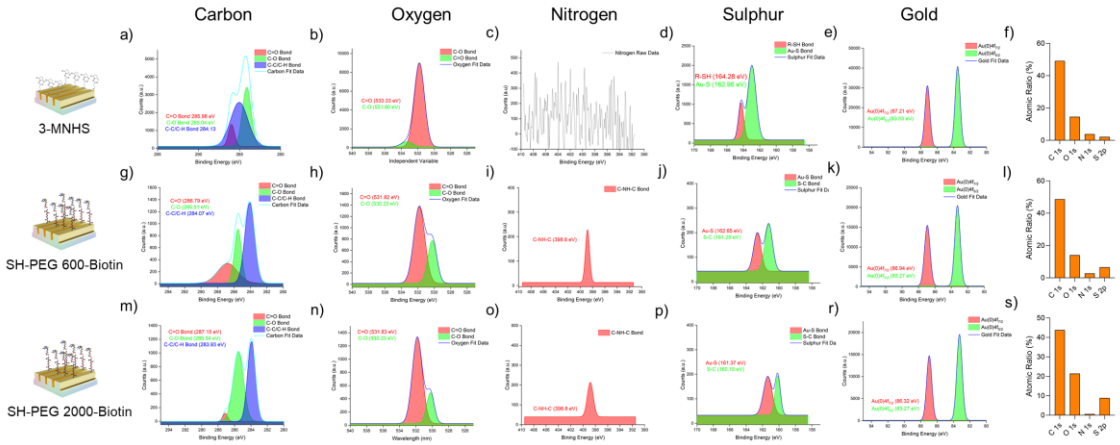

Figure 4.10: XPS measurements of surface modifications. The presence of 3-MNHS was analyzed using a) C1s, b) O1s, c) N1s, d) S2p, and e) Au4f scans, along with f) the corresponding atomic ratio. Similarly, g) C1s, h) O1s, i) N1s, j) S2p, and k) Au4f scans

were performed, and the corresponding l) atomic ratio was investigated for SH-PEG 600-Biotin. Finally, m) C1s, n) O1s, o) N1s, p) S2p, and r) Au4f scans were conducted, and the corresponding s) atomic ratio was determined for SH-PEG 2000-Biotin.

CHAPTER 5

5. DETECTION OF ALZHEIMER'S DISEASE BIOMARKERS WITH FLUORESCENCE COUPLED PLASMONIC METASURFACES

Avidin-FITC functionalized medium-distance modification was chosen as the building blocks for biosensing experiments in detecting AD biomarkers, since the highest fluorophore-induced plasmonic enhancement was observed on this configuration. Aβ 1-42 and tau-441 were chosen as model AD biomarkers. The avidin-FITC over medium-distance modification was then decorated with biotinylated anti-tau-441 antibody and biotinylated anti-Aβ 1-42 antibody for this regard. The detection of the biomarkers for the respective antibodies was monitored in a label-free manner by tracking the change in the plasmonic resonance.

5.1 ATR-FTIR analysis of Antibody Functionalized Medium-Distance Modification

To verify that the plasmonic wavelength signals were specific to the AD biomarkers, it was essential to ensure antibody immobilization on medium-distance modification. For this purpose, ATR-FTIR analysis was performed on each layer of the tau-441 capturing assay, which included bare metasurface, medium-distance modification, avidin-FITC, and biotinylated anti-tau (189-195) antibody.

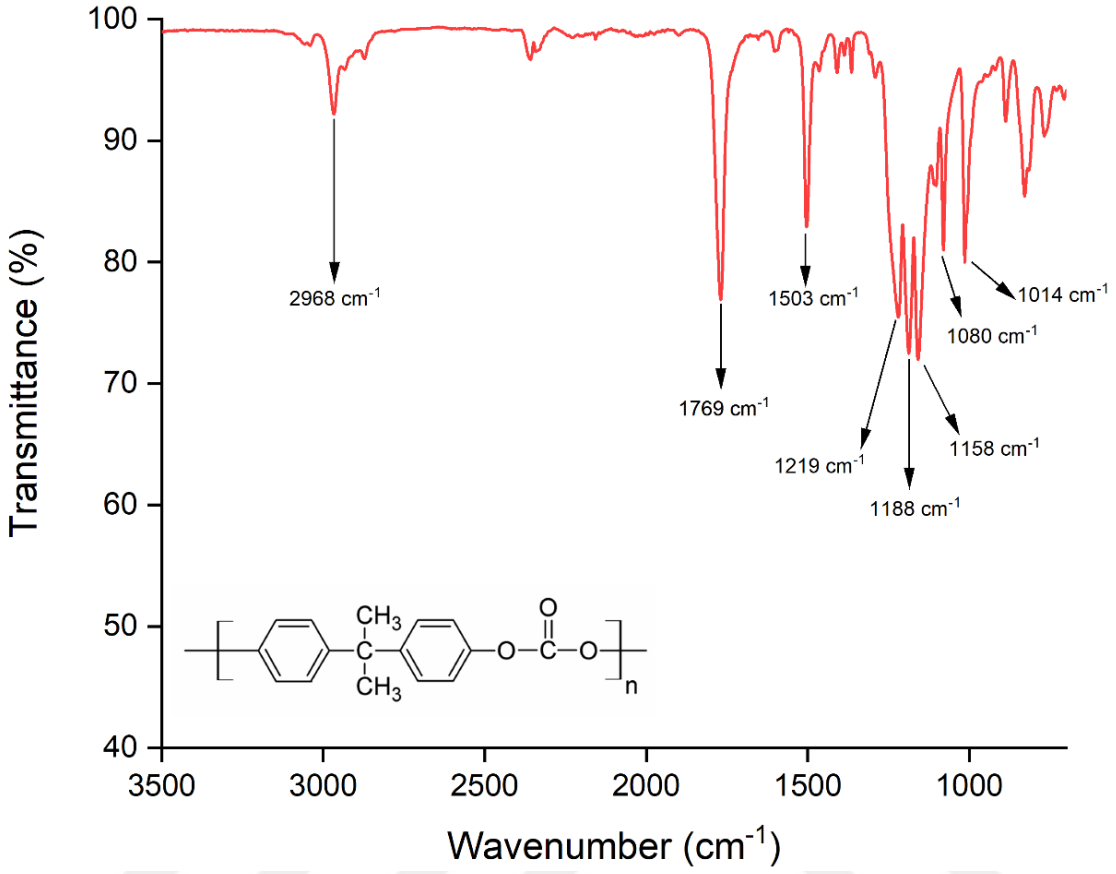

Figure 5.1: ATR-FTIR analysis of the polycarbonate templated DVD metasurface.

DVD metasurface was composed of mainly polycarbonate. The presence of the wavenumbers corresponding to the vibrational stretching of C-H bonds in -CH_3 groups at 2968 cm^{-1} and -CH_3 vibrations at 1080 cm^{-1} indicated the presence of methyl groups found in the polycarbonate backbone. In addition, the presence of the carbonate group in the polycarbonate backbone was obtained by the carbonate group vibrations (C=O) at 1769 cm^{-1}, asymmetric symmetric stretching of carbonate groups (O-C-O) between 1219-1158 cm^{-1}, and vibrational stretching of carbonate groups (O-C-O) at 1014 cm^{-1}. Moreover, the stretching of C=C double bonds in phenolic rings at 1503 cm^{-1} and vibration group specific to para (1 and 4) phenols at 828 cm^{-1} suggested the presence of characteristic phenolic rings in the polycarbonate backbone (Figure 5.1). These results agreed with the reported results for polycarbonate in the literature [220].

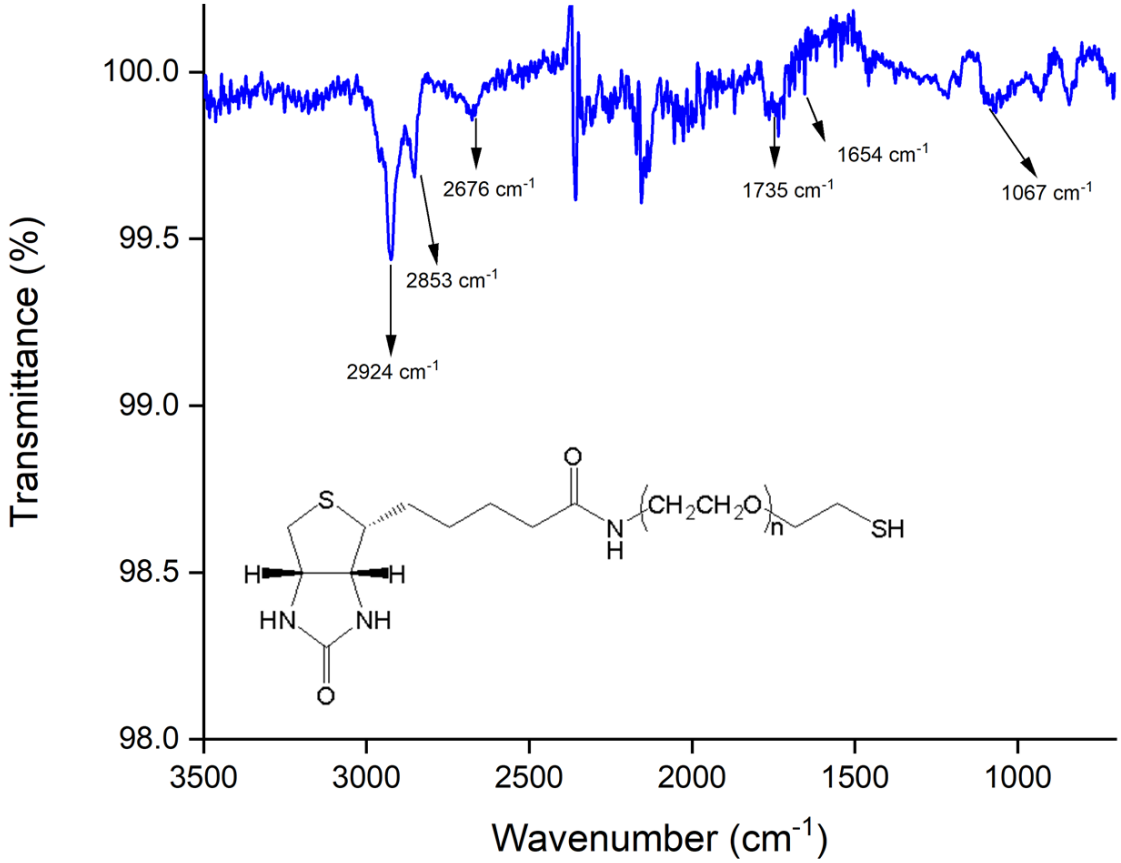

Figure 5.2: ATR-FTIR analysis for medium-distance modification (SH-PEG 600-Biotin).

Medium-distance modification (SH-PEG 600-Biotin) was composed of a thiol group, a polyethylene glycol backbone (MW: 600 Da), and a biotin molecule. It was applied to the metasurface for the immobilization of avidin-FITC proteins. The stretching of -CH_2- groups within the PEG moiety was observed at 2853 cm^{-1}. Further, the stretching of –SH groups were monitored at 2676 cm^{-1}, suggesting the presence of thiol group in the medium-distance modification. Moreover, the stretching of carbonyl ketone groups (R-(C=O)-R') at 1735 cm^{-1}, the stretching of the secondary amine group in biotin at 1654 cm^{-1}, and the stretching of the secondary amine at 1067 cm^{-1} revealed the presence of biotin moieties in the medium-distance modification (Figure 5.2). The obtained results were consisted with previously reported thiolated PEG and biotin molecules in the literature [221], [222]. In addition, vibrational stretching of C-H bonds in -CH_3 groups associated to the polycarbonate templated metasurface was observed at 2924 cm^{-1} (Figure 5.2).

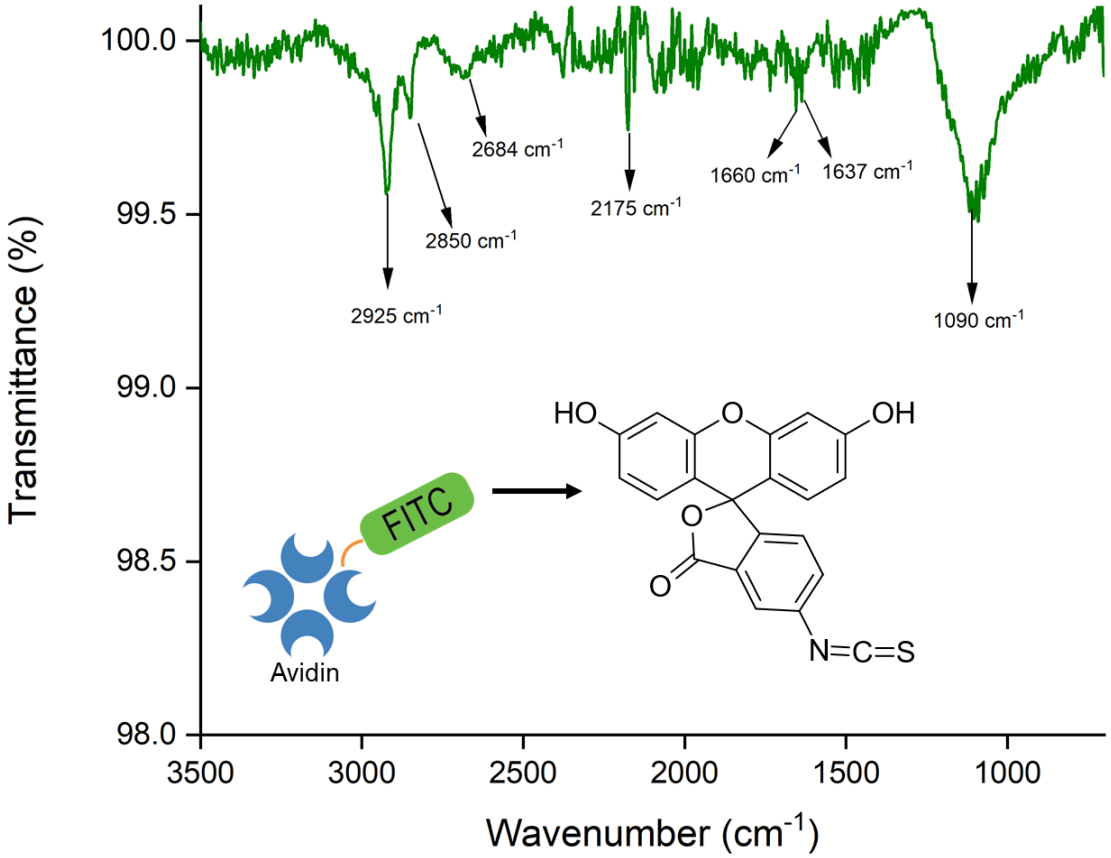

Figure 5.3: ATR-FTIR analysis of avidin-FITC over medium-distance modification.

Avidin-FITC is a conjugate molecule consisting of avidin protein and fluorochrome fluorescein isothiocyanate. The wavenumbers corresponding to avidin-FITC over medium-distance modification revealed more intense and broader amino group signals at 1090 cm^{-1} compared to the medium-distance modification (Figure 5.5) [223]. The observation of amid I at 1660 cm^{-1} and amid II at 1637 cm^{-1} suggested the occurrence of the avidin-biotin binding interaction (Figure 5.3) [224]. Moreover, the presence of isocyanate groups (N=C=O) were reported at 2175 cm^{-1} which was associated with the fluorochrome (Figure 5.3) [225]. In addition, the wavenumbers observed at 2925 cm^{-1}, 2850 cm^{-1}, and 2684 cm^{-1} showed similarities with those in Figure 5.2.

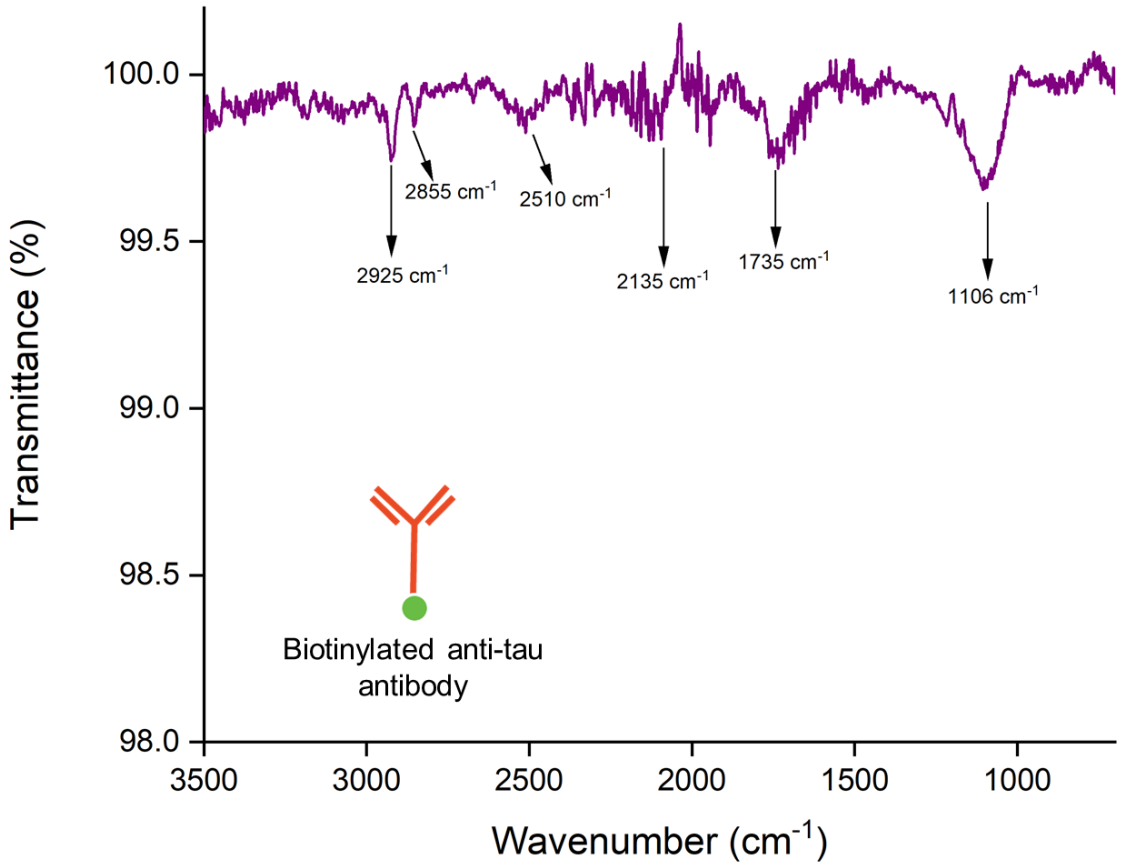

Figure 5.4: ATR-FTIR analysis of biotinylated anti-tau antibody over avidin-FITC functionalized medium-distance modification

Protein associated amid I (C=O) and amid II (N-H) are typically observed in the wave number range of 1700-1600 cm^{-1} and 1600-1500 cm^{-1}, respectively [226]. As observed in Figure 5.4, the broad signal in the range of 1500-1750 cm^{-1} with the peak at 1735 cm^{-1} indicates the binding of antibodies to the surface. In addition, the wavenumbers observed at 2925 cm^{-1}, 2855 cm^{-1}, 2510 cm^{-1}, 2135 cm^{-1}, and 1106 cm^{-1} showed similarities with those in Figure 5.3. The ATR-FTIR analysis of the bare metasurface, medium-distance modification (SH-PEG 600-Biotin), avidin-FITC, and biotinylated anti-tau antibody was designated in Figure 5.5 from top to bottom order.

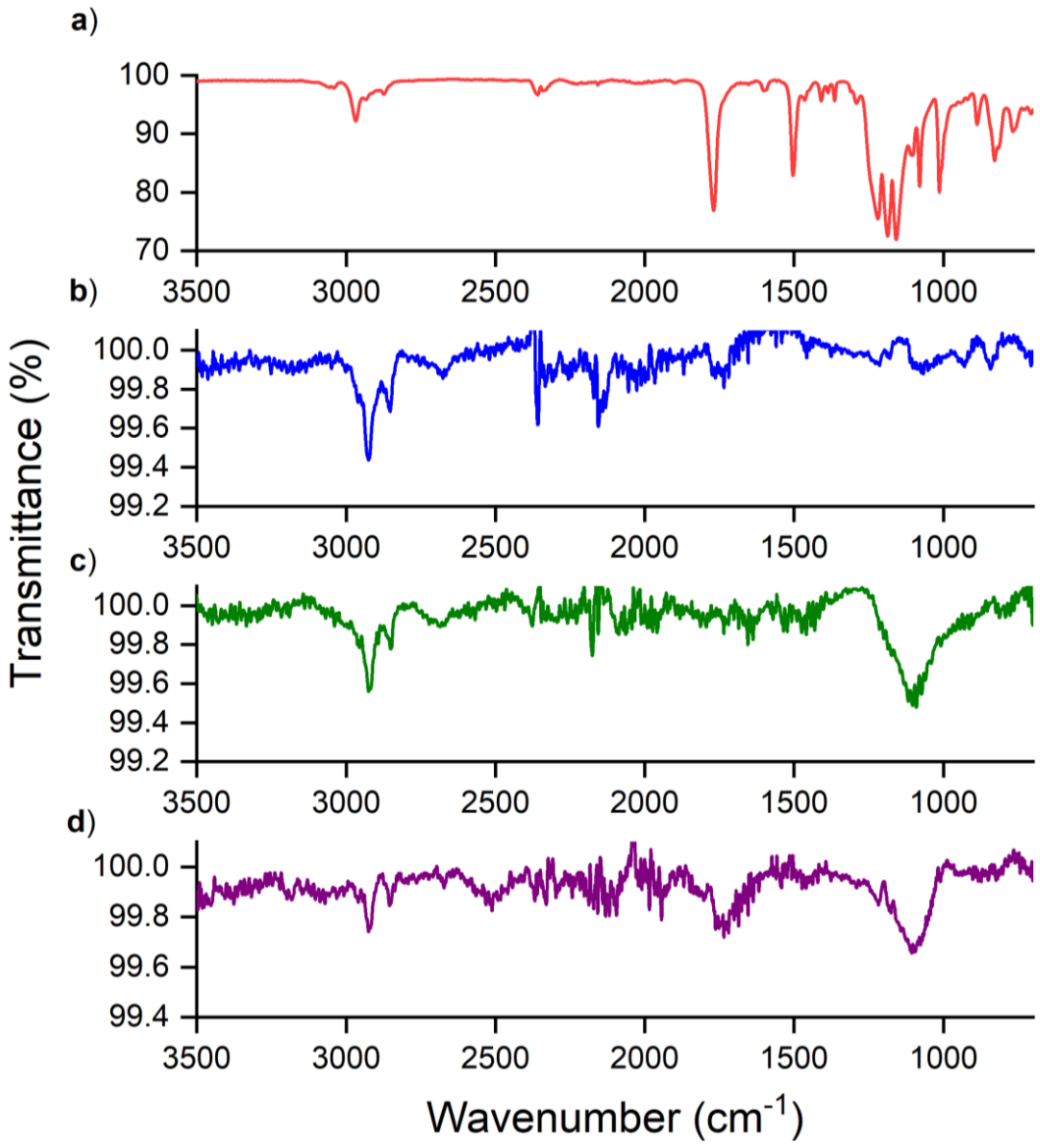

Figure 5.5: The ATR-FTRIR analysis of the functional layers applied on medium-distance modification for the capture of tau-441. a) Bare metasurface, b) medium-distance modification, c) avidin-FITC, and d) biotinylated anti-tau antibody associated peaks were summarized.

5.2 Contact Angle Analysis of Antibody Functionalized Medium-Distance Modification

The contact angle measurements were performed additional to the ATR-FTIR analysis of the antibody (biotinylated anti-tau antibody) functionalized medium-distance modification for understanding the hydrophilic and hydrophobic behavior of the metasurface. For this purpose, contact angle measurements were performed on each layer of the tau-441 in serum capturing assay, which included bare metasurface, medium-distance modification, avidin-FITC, biotinylated anti-tau (189-195) antibody, and BSA.

The bare metasurface exhibited an average contact angle of 81.67° ± 7.4° (Figure 5.6 a). This value is below 90°, indicating a hydrophilic surface [227]. The application of medium-distance modification (SH-PEG 600-Biotin) on metasurface reduced the contact angle to an average value of 60.1° ± 4.3° (Figure 5.6 b). The thiol functional end and PEG (CH_2-CH_2-O) backbone present in the medium-distance modification demonstrated a hydrophilic effect [228], while the biotin groups, on the other hand, contributed to a hydrophobic structure [229]. The decrease in the contact angle is due to the dominance of PEG molecules over the biotin groups. The application of avidin-FITC molecules on the surface increased the contact angle to 64.7° ± 3.4° (Figure 5.6 c). This increase in the contact angle could be attributed to the specific hydrophobic structure associated with avidin-biotin binding [229].

Integration of biotinylated anti-tau antibody decreased the contact angle of 42° ± 1.2° (Figure 5.6 d). The decrease in the contact angle indicated that the antibody structures were predominantly hydrophilic. This finding aligned with general polarity of the regions where antibodies specifically bind to antigens [230]. Subsequently, when BSA protein was applied to the surface (surface blocking), the corresponding contact angle further decreased to 31.6° ± 1.4° (Figure 5.6 e). This result designated the predominant presence of hydrophilic regions in BSA protein [231].

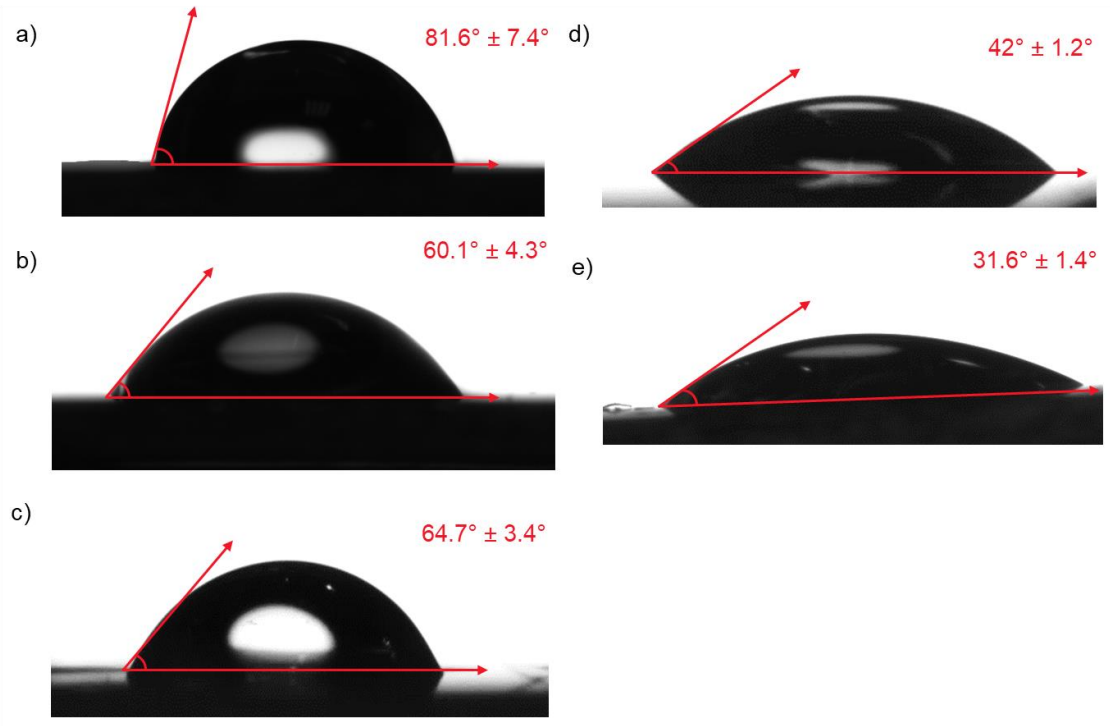

Figure 5.6: Contact angle measurements of the functional layers applied on medium-distance modification for the capture of tau-441. a) Bare metasurface, b) medium-distance modification, c) avidin-FITC, d) biotinylated anti-tau antibody, and e) BSA protein.

5.3 Surface Topography Analysis of Antibody Functionalized Medium-Distance Modification

The change in surface topography upon surface functionalization steps were intended to be investigated using LSCM. The surface functionalization steps were applied in the following order: bare metasurface, medium-distance modification, avidin-FITC, biotinylated anti-tau antibody, and BSA protein. The surface was marked with a reference scratch where all the measurements could be collected from the same region (Figure 5.7 a-b). The results were converted to root mean square (RMS) roughness values from a line of grating consisted of 100 nm (Figure 5.7 c-e). RMS results provided the variance in the height of selected grating which was utilized to obtain structural information of the functionalization steps and verify the immobilization of each functional layer through change in RMS value. The RMS roughness results were obtained as follows: 22.62 nm ± 5.41 nm for the bare metasurface, 21.66 nm ± 2.60 nm for the medium-distance

modification (SH-PEG 600-Biotin), 13.20 nm ± 1.95 nm for avidin-FITC, 21.06 nm ± 1.25 nm for biotinylated anti-tau antibody, and 30.5 nm ± 5.76 nm for BSA (Figure 5.7 f).

The RMS value of the medium-distance modification was slightly lower than that of the bare metasurface. After introducing avidin-FITC, a decrease in RMS roughness values was observed due to the effect of avidin-biotin interactions on the surface. Depending on the location of biotin on the antibody, an increase in the RMS value was observed due to the change in the orientation of the antibodies [232]. The BSA modification resulted in the highest RMS value.

The calculated difference in average height variances between the bare metasurface and BSA functionalization was 7.88 nm ± 5.41 nm. It was important to note that this value did not correspond to the thickness of the medium-distance modification. Instead, it indicated that the metasurface was structurally functionalized, and the height variance from the mean value was particularly significant between avidin-FITC and BSA protein.

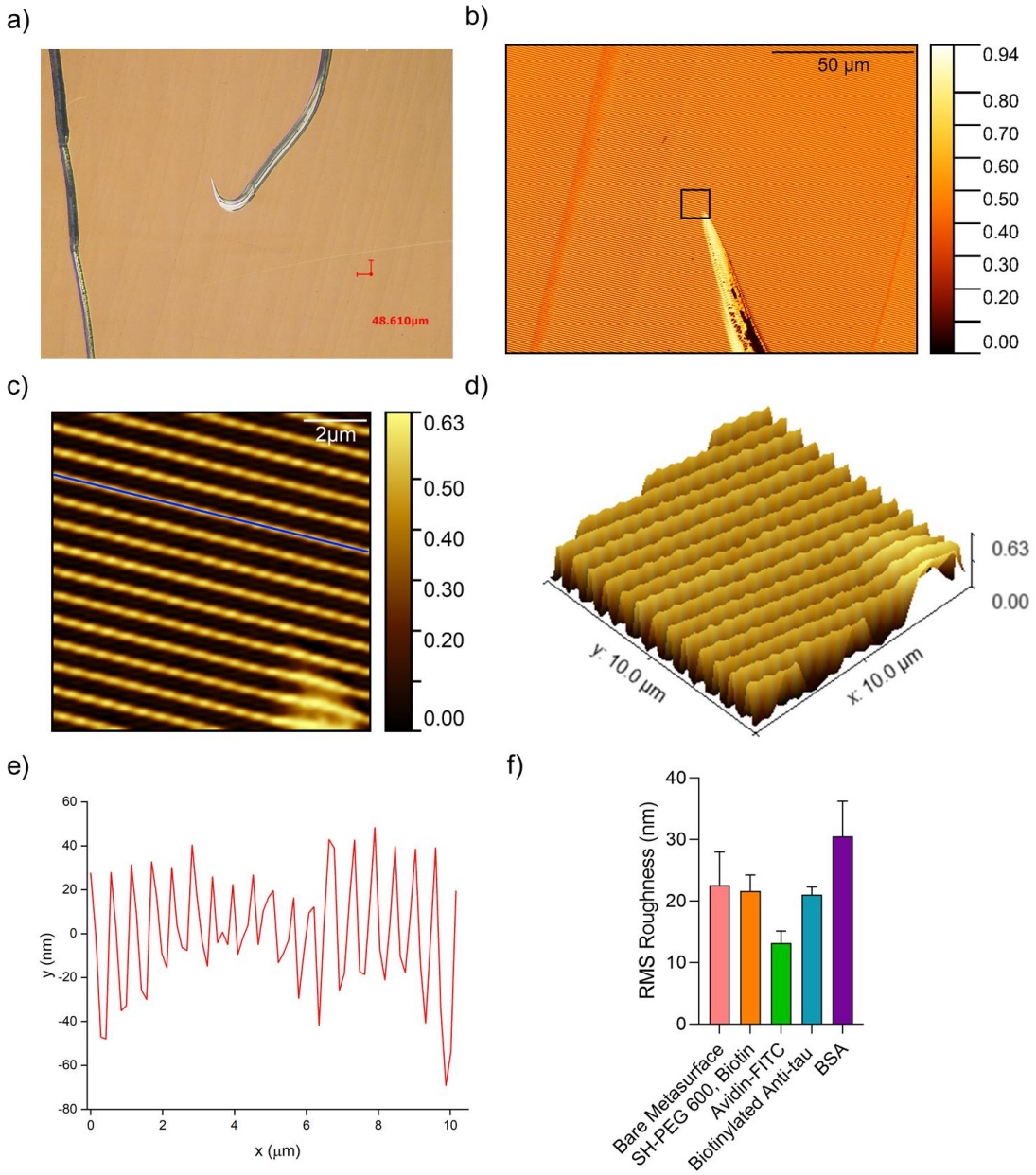

Figure 5.7: Surface topography and RMS roughness analysis of functionalized metasurface. a) The optical image of the metasurface was provided with a hook-shaped scratch which provided a reference marker for the measurement point (scale bar: 48.6 µm). b) Confocal laser microscopy acquired image (scale bar: 50 microns). c) Grating structures on the metasurface are shown (the region where data was taken for linear roughness analysis was marked as blue). d) The detailed 3D surface morphology of the measurement area. e) Linear roughness graph obtained from the line of a single grating. f) A comparison of RMS roughness values between surface functionalization steps were

designated. Statistical evaluations were reported using one-way analysis of variance (One-way ANOVA) with Tukey's post-hoc multiple comparison test (n=3; **: $p<0.01$).

The AFM scratch test was employed to measure the thickness of the medium-distance modification functionalized with biotinylated anti-tau antibody and BSA protein. The sample was dried before the application of the scratch test. The DVD-templated metasurface was replaced with a silicon wafer substrate which was coated with titanium (10 nm), silver (30 nm), and gold (15 nm) for replicating the metasurface without any grating structure. The reason of choosing a silicon substrate for the metasurface was simplifying the process of scratch test by removing the grating structures. The final thickness of biotinylated anti-tau antibody and BSA functionalized medium-distance surface modification was expected to be around to be 20-25 nm including the approximate size of antibody (10-15 nm) [233], [234]. The AFM scratch test utilized three steps to measure the thickness of the medium-distance modification functionalized with biotinylated anti-tau antibody and BSA protein. Primarily, the surface was scanned to obtain a baseline image of the surface (Figure 5.8 a). Secondly, a specific region of interest was chosen, and the scratch test was applied to this selected area. Finally, the surface was scanned again to capture the image of post-scratch surface (Figure 5.8 b). To ensure accurate measurements and eliminate any potential deviations (in this case, 1 μm), a reference point was selected. A surface artifact was chosen as the reference point in the measurements (Figure 5.8 c-d). By comparing the line profiles obtained from before and after scratch images, the scratch test revealed a height difference of 5.1 nm (Figure 5.8 e-f). The results suggested that PEG polymers were entangled with each other and precipitated, especially after drying, due to the lack of hydrophilic interactions in the PEG backbone. This can be attributed to the breaking of PEG polymers and intramolecular binding of PEG [235]. As a result, the resultant thickness (5.1 nm) differed from the expected thickness (20-25 nm).

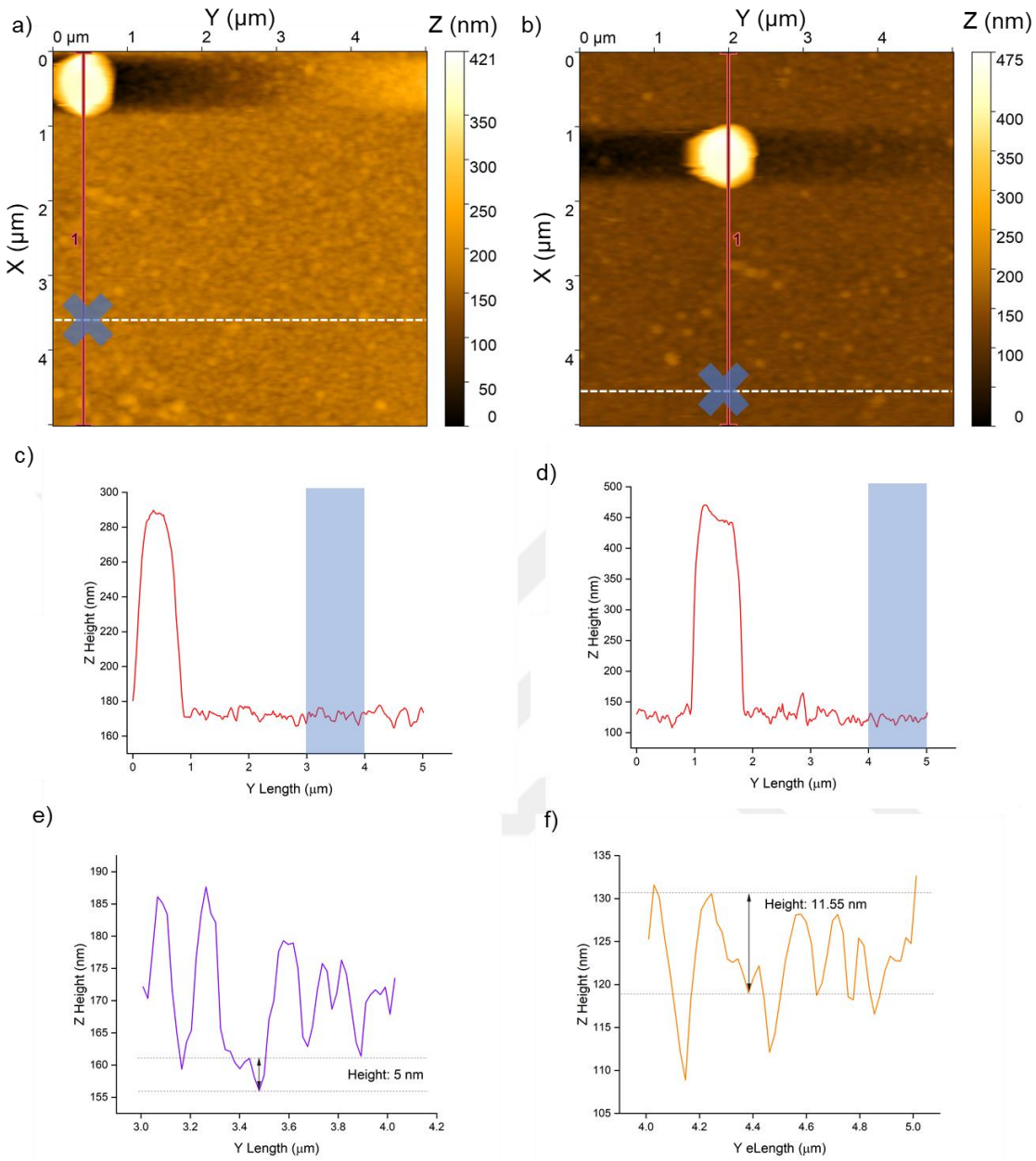

Figure 5.8: AFM scratch test of the biotinylated anti-tau antibody and BSA functionalized medium-distance modification over silica wafer templated metasurface. a) AFM image acquired before scratching. b) AFM image acquired after scratching. c) Line profile acquired from region of interest. d) Line profile acquired after scratching. Axial height obtained from line profile e) before and f) after scratching test.

The AFM tip used for the scratching test was analyzed using SEM and Energy-Dispersive X-ray (EDX) spectroscopy to verify the scratched surface modification on the AFM tip (Figure 5.9 a). EDX is capable of providing elemental analysis of the samples imagined

under SEM by collecting the surface-emitted X-rays. These X-rays were then used for the identification and quantitative analysis of the elements present on the surfaces. The EDX analysis of the AFM tip revealed the presence of shallow peaks (low counts, 20-200) associated with sulfur (S Lα, 0.14 keV), carbon (C Kα, 0.28 keV), and oxygen (O Kα, 0.51 keV) (Figure 5.9b). The AFM tip was composed of only Silicon (Si Kα, 1.75 keV) (high counts, ~1000) (Figure 5.9c). Therefore, the presence of O, S, and C elements suggested that the medium-distance surface modification was scratched from the silica wafer templated metasuface. These peak results were consistent with the literature [236]–[238]

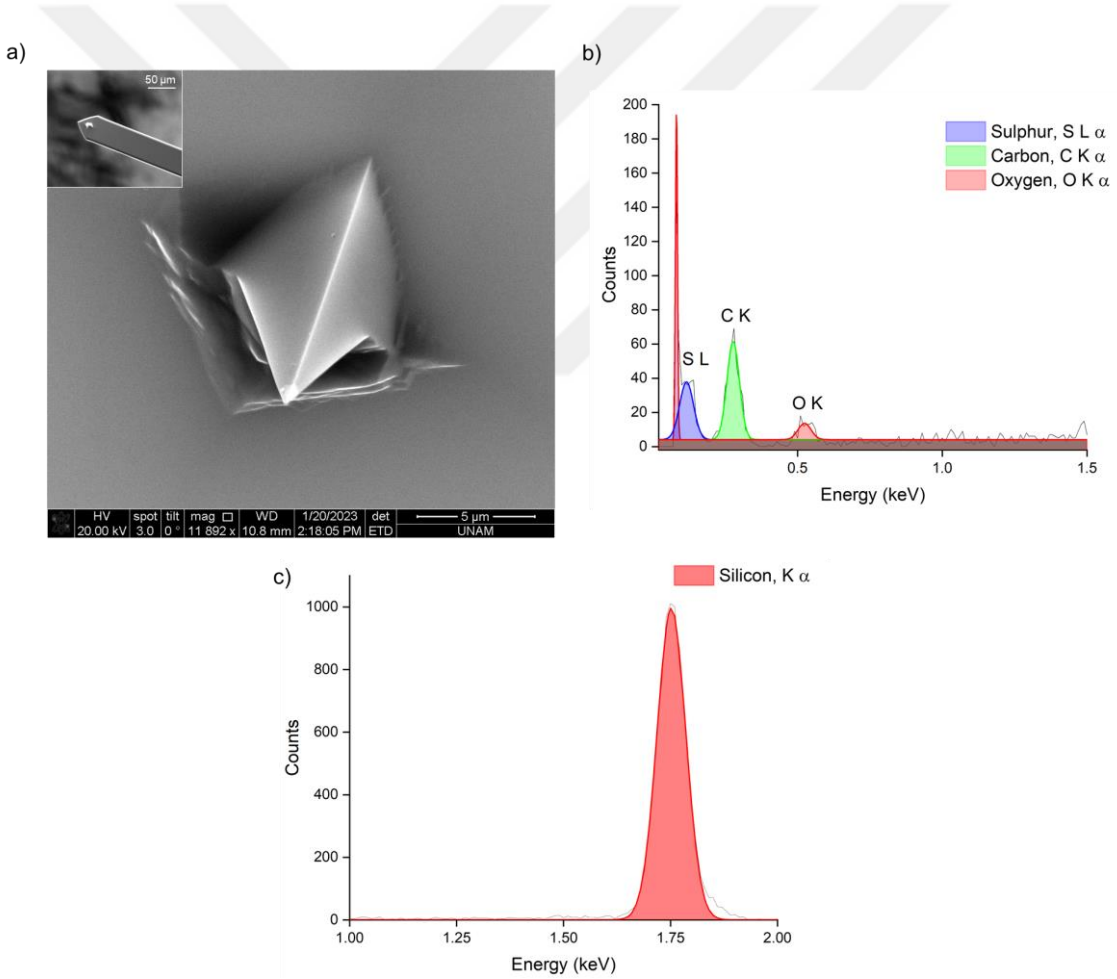

Figure 5.9: EDX Analysis for AFM tip used on the course of the scratch test. a) SEM image of AFM tip. b) H, S, C, and O associated peaks obtained from EDX analysis of the AFM tip. c) Si associated peak obtained from EDX analysis of the AFM tip.

5.4 Detection of Amyloid Beta 1-42

Biotinylated anti-Aβ 1-42 antibodies (25 μM) were immobilized over avidin-FITC functionalized medium-distance modification. Initially, PBS solution was used for the background measurement before detecting the biomarkers association peak. Different concentrations spanning from 100 to 400 μg/ml of Aβ 1-42 were introduced to these sensors, and then, the sensors were washed with PBS solution in order to remove any non-bound biomarkers from the surface. The average plasmonic wavelength shifts for different Aβ 1-42 concentrations were reported as follows: 0.14 ± 0.04 nm, 0.67 ± 0.08 nm, 1.11 ± 0.33 nm, 0.6 ± 0.11 nm for 100, 200, 300, and 400 μg/ml of Aβ 1-42, respectively (Figure 5.10 a-d). The highest mean value was observed in 300 μg/ml Aβ 1-42. This concentration value was further investigated in human serum for the evaluation of the immunoassay for clinical samples. The serum was diluted 1/1000 (v:v) for close-matching the refractive index of PBS and injected with 300 μg/ml Aβ 1-42. In serum samples, the surface was functionalized with BSA for preventing non-specific binding which may cause false positive results [239]. 300 μg/ml Aβ 1-42 in serum designated 0.36 ± 0.18 nm wavelength shift (Figure 5.10 e).

The mean wavelength shift values of Aβ 1-42 were compared with each other using point and violin plots (Figure 5.10 f-g). One-way analysis of variance (one way-ANOWA) with Tukey post hoc multiple comparison test was performed for determining statistical difference between the concentration groups (Figure 5.10 g).

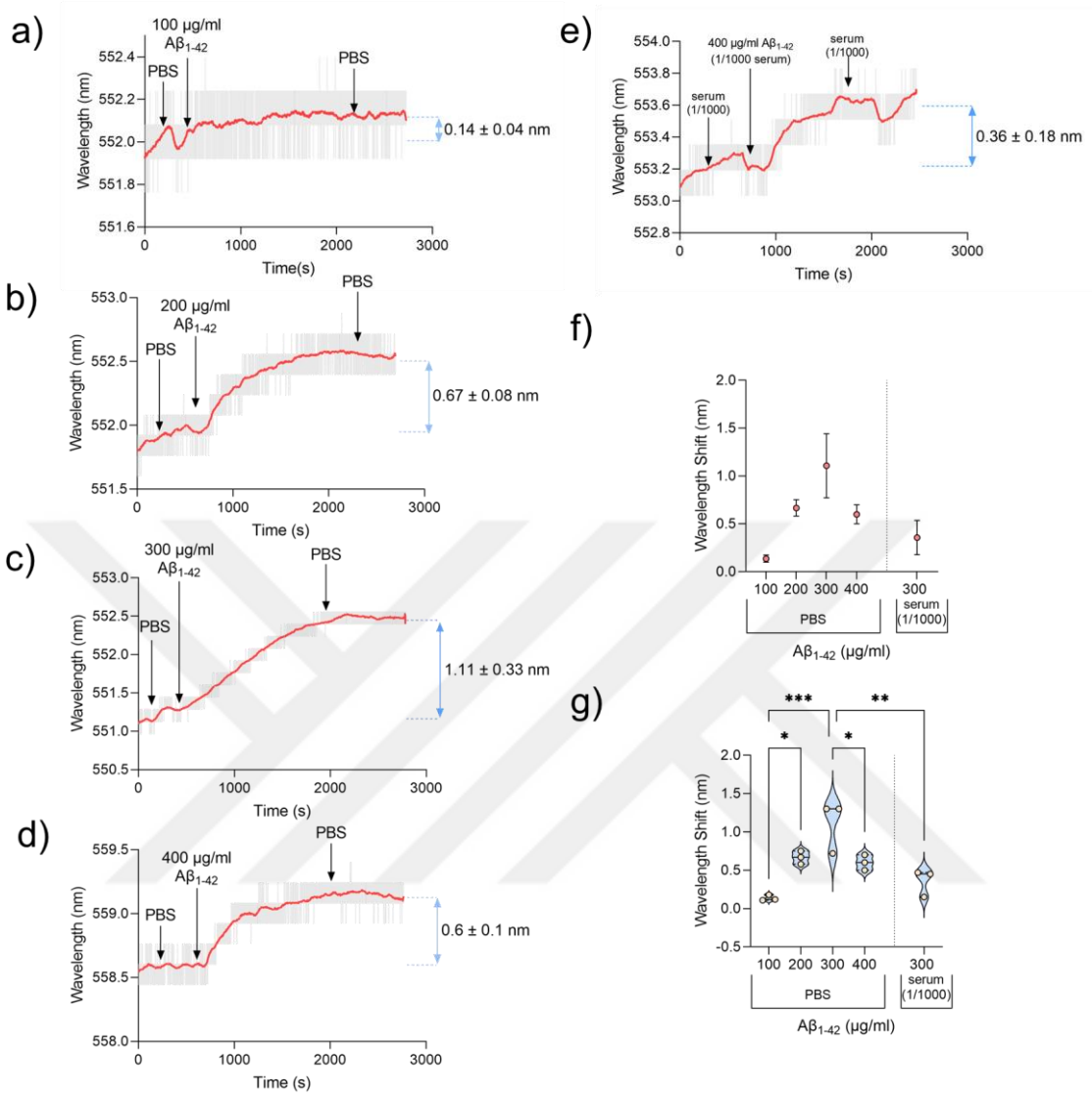

Figure 5.10: The real time changes in the plasmonic resonance wavelength of Aβ 1-42 at different concentrations were presented. The concentration values of Aβ 1-42 were determined as follows: a) 100 µg/ml, b) 200 µg/ml, c) 300 µg/ml, d) 400 µg/ml in PBS, and e) 300 µg/ml Aβ1-42 in serum. The wavelength shift results of Aβ 1-42 was demonstrated in f) a point plot and g) a violin plot. The statistical evaluations were reported on the violin plot using one-way analysis of variance (One-way ANOVA) with Tukey's post-hoc multiple comparison test (n=3; *: $p<0.05$; **: $p<0.01$; ***: $p<0.001$).

5.5 Detection of Tau-441

Biotinylated anti-tau (189-195) antibodies (25 μM) were immobilized on an avidin-FITC functionalized medium-distance surface modification to capture tau-441, similar to the immobilization of biotinylated anti-Aβ 1-42 antibodies. Different concentrations of tau-441 (5, 10, 15, and 20 μg/ml) were introduced to the antibody-functionalized sensor. The mean plasmonic wavelength shifts for tau-441 concentrations were followed as: 0.24 ± 0.23 nm, 0.30 ± 0.34 nm, 0.38 ± 0.17 nm, and 0.44 ± 0.2 nm for 5, 10, 15, and 20 μg/ml tau-441, respectively (Figure 5.11 a-d). The highest mean value was observed at 20 μg/ml tau-441, which was further investigated in human serum to evaluate the immunoassay for clinical samples. The serum was diluted 1/1000 to match the refractive index of PBS, and then 20 μg/ml tau-441 was injected, similarly to the detection of Aβ 1-42. The serum specimen injected with 20 μg/ml tau-441 designated a wavelength shift of 1.33 ± 0.6 nm (Figure 5.11 e).

Similar to Aβ 1-42 detection analysis, the mean wavelength shift values of tau-441 were also compared using point and violin plots, and one-way ANOVA with Tukey post hoc test was applied to determine significant differences between concentration groups of tau-441 (Figure 5.11 f-g).

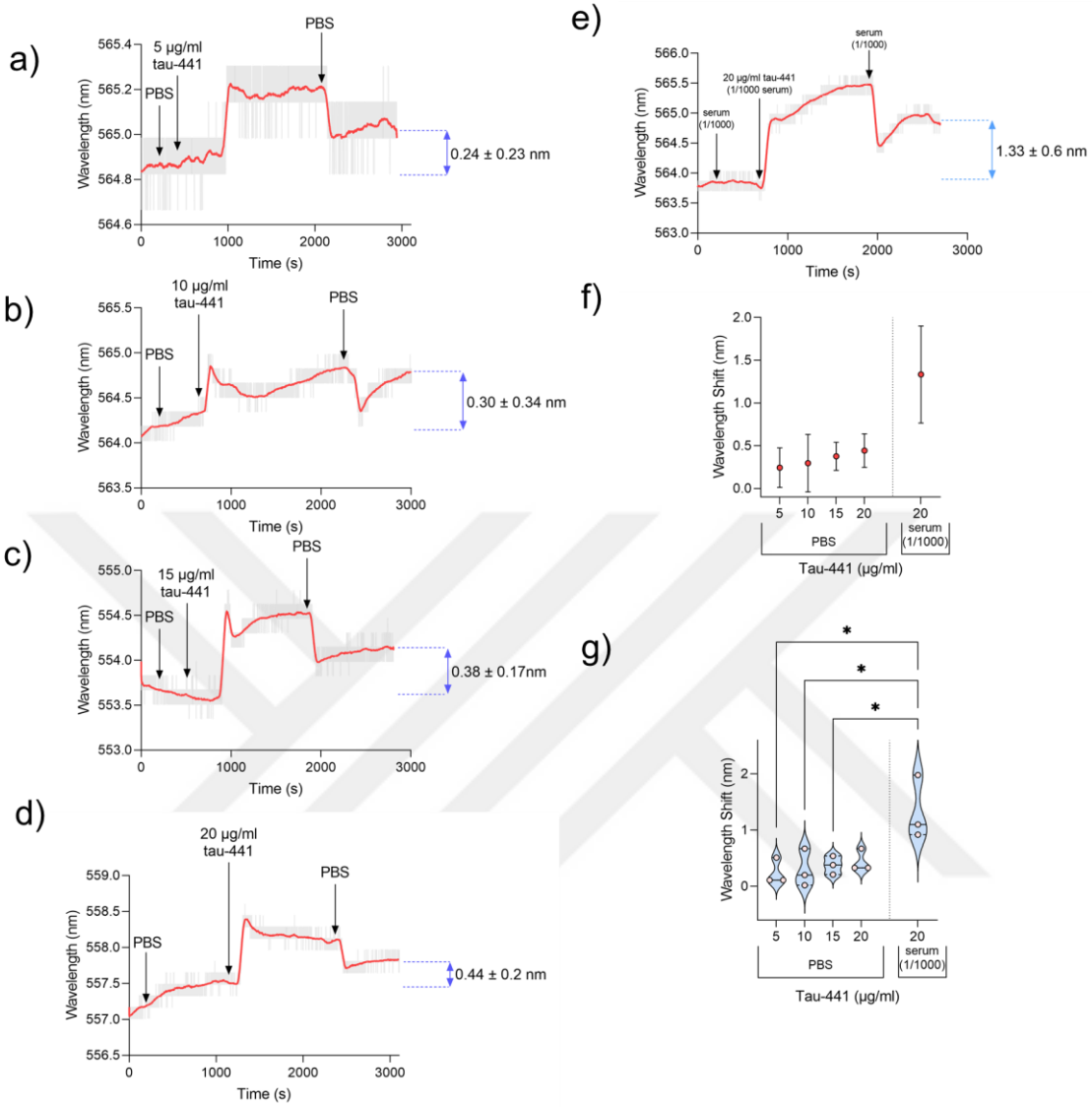

Figure 5.11: The real time changes in the plasmonic resonance wavelength of tau-441 at different concentrations were presented. The concentration values of Tau-441 was determined as follows: a) 100 µg/ml, b) 200 µg/ml, c) 300 µg/ml, d) 400 µg/ml in PBS, and e) 300 µg/ml tau-441 in serum. The wavelength shift results of tau-441 was demonstrated in f) a point plot and g) a violin plot. The statistical evaluations were reported on the violin plot using one-way analysis of variance (One-way ANOVA) with Tukey's post-hoc multiple comparison test (n=3; *: $p<0.05$; **: $p<0.01$; ***: $p<0.001$).

5.6 ELISA test of Amyloid Beta 1-42

Aβ 1-42 detection performance of the fluorescence-enhanced plasmonic metasurface was compared to the gold-standard method, i.e., ELISA (Amyloid beta 42 Human ELISA Kit). Briefly, ELISA method utilizes secondary labels for detecting biomarkers. Therefore, the sensitivity and the dynamic range of the ELISA kits would be down to pg/ml levels. As a result, the Aβ 1-42 samples analyzed with ELISA were serially diluted, in stepwise manner, by a factor of approximately one thousand (10^3) from μg/ml to pg/ml. A set of standard solutions (0-1000 pg/ml) was measured for obtaining a calibration curve and quantifying the concentration value of the samples (Figure 5.12 a). ELISA test was performed on both PBS and diluted human serum. In both solutions, 12 samples (3 replicates for each concentration value) were used with Aβ 1-42 concentrations of 200, 400, 600, and 800 pg/ml. Both the PBS and the human serum samples Aβ 1-42 designated a linear response with increasing concentration (Figure 5.12 b-c). One-way ANOVA with Tukey post hoc test was applied to the Aβ 1-42 concentration values in PBS and serum to determine the significant differences between concentration groups (Figure 5.12 d-e). For comparison of sample mediums, PBS and diluted serum were measured without any samples, and they showed no significant difference between each other, and also, demonstrated a significant difference with the lowest concentration (0 pg/ml Aβ 1-42) value of the standard solutions (Figure 5.12 f).

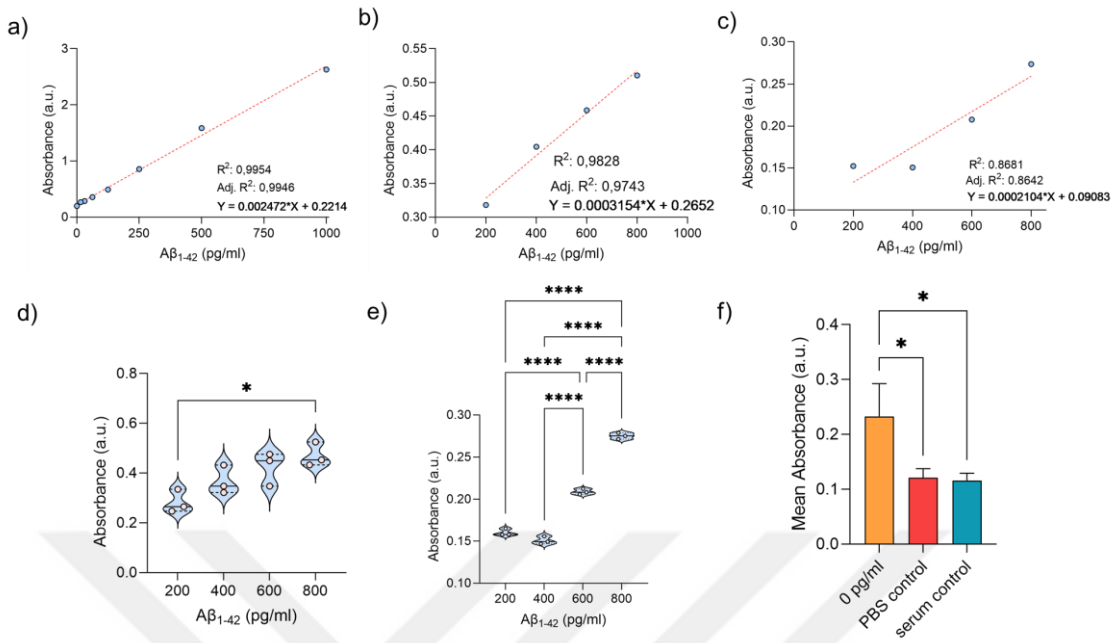

Figure 5.12: The ELISA results of Aβ 1-42. a) Linear response of standards. b) Linear response of samples in PBS. c) Linear response of samples in serum. Violin plots of d) PBS and e) serum samples. e) Signal comparison between 0 pg/ml standard solution, PBS control and serum control. The statistical evaluations were reported on the violin plot using one-way analysis of variance (One-way ANOVA) with Tukey's post-hoc multiple comparison test (n=3; *: $p<0.05$; ****: $p<0.0001$).

5.7 ELISA test of Tau-441

The tau-441 detection performance of the fluorescence-enhanced plasmonic metasurface was also compared with the ELISA test (Human Tau colorimetric ELISA Kit). Similar to the Aβ 1-42 ELISA detection, down to pg/ml concentration window was also projeccted for the detection tau-441. Initially, a set of standard solutions (0-1000 pg/ml) was measured (Figure 5.13 a). Then, PBS and serum samples of tau-441 were measured with concentration values of 75, 225, and 300 pg/ml. Both PBS and serum samples were detected with the ELISA kit, but serum samples failed to designated a linear response (Figure 5.13 c). One-way ANOVA with Tukey post hoc test was applied to the tau-441 concentration groups both in PBS and serum (Figure 5.13 d-e). Similar to the Aβ 1-42 ELISA detection, PBS and diluted serum solutions were measured without any samples, and they showed no significant difference between each other, and also,

demonstrated a significant difference with the lowest concentration (0 pg/ml tau-441) value of the standard solutions (Figure 5.13 f).

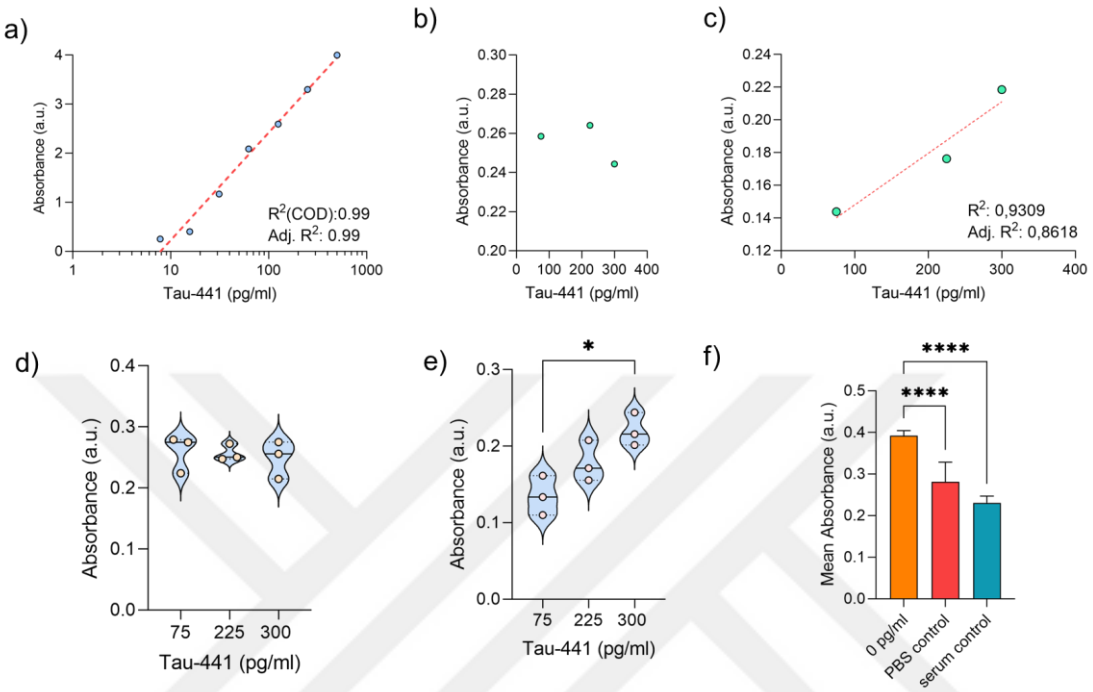

Figure 5.13: The ELISA results of Tau-441. a) Linear response of standards. b) Linear response of samples in PBS. c) Linear response of samples in serum. Violin plots of d) PBS and e) serum samples. e) Signal comparison between 0 pg/ml standard solution, PBS control and serum control. The statistical evaluations were reported on the violin plot using one-way analysis of variance (One-way ANOVA) with Tukey's post-hoc multiple comparison test (n=3; *: $p<0.05$; ****: $p<0.0001$)

CHAPTER 6

6. CONCLUSION AND FUTURE PROSPECTS

In this study, coupling effect between fluorophores and the surface plasmons was investigated in a distance-dependent manner. Herein, a DVD-templated plasmonic metasurface was fabricated and integrated with three different surface modifications varying in separation distances between the fluorophore molecules and the metasurface. The DVD-templated metasurface was chosen to reduce fabrication-related costs and provide scalable production of the end product. Therefore, the utility of DVD substrate eliminated the requirement of traditional nanoperiodic structure fabrication methods, such as FIB, photolithography, and e-beam lithography [120]. DVD surface readily contains a nanoperiodic grating, and hence, it does not require any additional steps for surface patterning. This has also paved the way to meet the criteria for developing POC devices according to the RE-ASSURED qualifications [240]. Besides, these devices need to maintain high sensitivity for the tracking of low concentration biomarkers. This is especially vital for the early diagnosis of AD, since the presence of AD biomarkers at early stages is low in concentration, especially in serum [241]. The current DVD-templated metasurfaces, hence, need to be integrated with signal amplification methods for achieving this goal. Among signal amplification methods, the coupling effect between fluorescence and surface plasmons holds great potential for strategizing next-generation POC biosensors [242].

This thesis projects to assess the optimum fluorescence-enhanced plasmonic condition on the DVD-templated metasurface, and at the same time, it aims to detect AD biomarkers from complex biospecimens. In Chapter 1, we elaborated on POC biosensors and plasmonic metasurfaces. We further discussed the integration of fluorescent proteins over the metasurfaces for developing fluorescence-enhanced plasmonic radiation. This signal enhancement was desired for the development of plasmonic POC biosensors. In Chapter 2, AD diagnosis and blood-based AD biomarkers were highlighted. AD was implemented as the model disease for the developed biosensor. In Chapter 3, we

introduced and explained the materials and methods used throughout the thesis. This chapter included details over the experimental protocols and characterization methods. On the other hand, the thesis was mainly structured on Chapter 4 and Chapter 5. Briefly, Chapter 4 describes the optical properties of the metasurface; explains the requirements of fluorescence-surface plasmon coupling; and examines the optimization conditions of a fluorescence-enhanced plasmonic metasurface. Chapter 5, on the other hand, provides the details on the detection of AD biomarkers using the optimized fluorescence-coupled plasmonic metasurface.

Particularly, in Chapter 4, it was aimed to integrate the metasurface with fluorescent proteins using different surface modifications and optimize spectral overlap between the fluorescent proteins and the plasmonic resonance of the metasurface. Initially, the plasmonic response of the metasurface was evaluated both numerically and experimentally. In this manner, the dimensions of the fabricated metasurface were characterized using AFM (Figure 4.1 e). The results were then transferred into an FDTD simulation model of the metasurface, and accordingly, the experimental and simulated reflection spectra of the metasurface in a water medium (n=1.33) were consistent with each other (Figure 4.2 a). The FDTD model designated a plasmonic resonance peak at 575 nm while experimental results indicated a peak at 552 nm. The peak position of the plasmonic resonance of the simulation and experiment results were close, and the difference would be possible fabrication challenges during the chemical etching steps and differentiation in metal coatings. Further, the FDTD model designated the confinement of electric field at the corners of the metasurface, these regions are known as electromagnetic hotspots (Figure 4.2 d). These hotspots are critical for providing a strong coupling between fluorescence and surface plasmons. Next, the bulk sensitivity of the plasmonic metasurface was analyzed while applying various concentrations of glycerol solutions. From this analysis, S and FOM values were calculated for obtaining a numerical value of the performance of the metasurface (Table 4.1). After the analysis of the optical properties, the metasurface was ready to couple with the fluorophores.

Moreover, the coupling effect requires two critical optimization factors for the development of fluorophore-enhanced plasmonics. These are the separation distance between the fluorophore and the metasurface and the spectral overlap between the fluorescent spectrum and plasmonic resonance [140], [141]. The changes in the

separation distance have two possible distinct outcomes: (i) At short separation distances, a non-radiative energy transfer between the fluorophore and the metasurface results in the formation of lossy surface waves [141]. These surface waves were trapped on the surface and cannot radiate to the far field, resulting in the quenching of the fluorophore. (ii) The other possible outcome was the coupling between the fluorescence and plasmonic resonance forming a far-field radiating plasmon radiation at longer separation distances [243]. Surface modifications were chosen to have distinct molecular lengths and functional sites for coupling fluorophore plasmonic metasurface in a controlled manner. Here, three different surface modifications were adapted through 3-MNHS (~4-6 nm), SH-PEG 600-Biotin (~6-10 nm), and SH-PEG 2000-Biotin (~16-20 nm) which were entitled as short, medium, and long-distance modifications, respectively. The length of these surface modifications was calculated by considering the molecular size of the surface modification building blocks, such as avidin protein, ethylene glycol, and biotin molecules as reported in the literature [179] (Figure 3.3). These surface modifications were further integrated with avidin-FITCs to functionalize the metasurface with fluorescent proteins. The effect of fluorescence-plasmonic coupling was investigated using the wavelength shifts in plasmonic resonance. In this manner, avidin and avidin-FITC integrated surface modifications were investigated and their response to the presence of fluorescent label (FITC) was analyzed. On the short-distance modification, avidin protein enabled 1.17 times higher plasmonic signals over the avidin-FITC (Figure 4.4 a, b, and h). This result designated that the non-radiative energy transfer was dominant on the short-distance modification which led to the entrapment of plasmon radiation to the plasmonic nanostructure, instead of the far-field. In contrary, avidin-FITC decorated on the medium-distance modification enabled 4.4 times of signal enhancements with the respect to the avidin counterparts (Figure 4.4 c, d, and h), suggesting fluorescence-enhanced plasmonic radiation on this modification. Moreover, the long-distance modification maintained the fluorescence-enhanced far-field plasmon radiation with ~2.7 times of signal enhancement (Figure 4.4 e, f, and h). However, the signal-enhancement was lower than medium-distance modification, pointed out the long-distance modification drifted apart from the optimum separation distance, ~6-10 nm . After collecting the signals, the surface modifications were characterized using XPS. For this step, each surface modification was analyzed with carbon, oxygen, nitrogen, sulfur, and

gold scans while looking at the binding energy spectrum (Figure 4.10). The peaks associated with the carbon, oxygen, nitrogen, and gold scans were utilized to verify the presence of surface modifications over the metasurface.

The separation distance between the fluorophore and surface plasmons has also an impact on the fluorescence intensity. This phenomenon is known as plasmon-enhanced fluorescence, and the fluorescence intensity can be enhanced near-surface plasmon with optimized separation distance. Therefore, the impact of surface modifications on the fluorescence intensity was also investigated. The highest fluorescence intensity of avidin-FITC was observed on medium-distance modification, following long- and short-distance modification. The medium-distance modification had 3.68 and 2.61 times higher normalized fluorescence intensity than short- and long-distance modifications, respectively (Figure 4.8 a). Therefore, the medium-distance modification provided the optimum separation distance between fluorophore and metasurface. Furthermore, the fluorescent intensity was investigated before, during, and after avidin-FITC immobilization over the medium-distance modification for investigating the surface coverage. This was an essential parameter for maximizing the surface area of immobilized biotinylated antibodies for biomarker studies. The fluorescence intensity was around 60% recovered after the washing step, and hence, more than half of the medium-distance modification was functionalized with avidin-FITC (Figure 4.9 c).

The spectral overlap between the fluorescence spectrum and plasmonic resonance is the second most critical parameter for obtaining fluorescence-enhanced far-field plasmonic radiation. The efficiency of both non-radiative energy transfer and fluorescence-coupled surface plasmon was significantly affected by the spectral overlap [140], [142]. The impact of spectral overlap on the fluorescence-enhanced plasmonic radiation was investigated by changing the fluorophore over the medium-distance modification. Herein, avidin-FITC, avidin-Texas Red, streptavidin-Qdot 525, and streptavidin-Qdot 625 were applied over the medium-distance modification, and the changes in wavelength shift were investigated with the respect to avidin. The wavelength shift of the avidin-Texas Red was recorded as 1.3 times higher than that of avidin protein (Figure 4.7 d). This signal enhancement was lower than the avidin-FITC integration (~4.4 times). Furthermore, avidin wavelength shift was observed to be 5.1 and 1.8 times higher than streptavidin-Qdot 525 and streptavidin-Qdot 625, respectively (Figure 4.7 h). This

designated a signal drop towards Qdot-conjugated streptavidins. The results designated the highest wavelength shift on avidin-FITC, followed by avidin-Texas Red, streptavidin-Qdot 625, and streptavidin-Qdot 525, respectively. In a nutshell, the optimization steps of the separation distance and spectral overlap provided the avidin-FITC functionalized medium-distance modification as the optimum condition for achieving the fluorescence-enhanced plasmonic radiation over the DVD-templated metasurface.

In Chapter 5, it was aimed to convert the fluorescence-enhanced plasmonic metasurface to a biosensor in order to detect AD biomarkers that can be further adapted into the POC settings. Therefore, this combination was further utilized for capturing AD biomarkers. In this manner, biotinylated anti-tau antibody and biotinylated anti-Aβ 1-42 antibody were immobilized over the avidin-FITC functionalized medium-distance modification. Tau-441 and Aβ 1-42 were utilized as the AD biomarkers, and the capture events were monitored using the change in plasmonic resonance. Aβ 1-42 was captured on the medium-distance modification with the concentration values of 100, 200, 300, and 400 μg/ml. The average plasmonic wavelength shifts towards Aβ 1-42 were 0.14 ± 0.04 nm, 0.67 ± 0.08 nm, 1.11 ± 0.33 nm, 0.6 ± 0.11 nm for 100, 200, 300, and 400 μg/ml Aβ 1-42, respectively (Figure 5.1 a-d). 300 μg/ml Aβ 1-42 was further prepared using a diluted serum and the capture of Aβ 1-42 in serum was also detected by tracking the shift in plasmonic resonance (Figure 5.1 f and g). Likewise, the capture events of tau-441 was monitored for the concentration values of 5, 10, 15, and 20 μg/ml. The average plasmonic wavelength shifts towards tau-441 were 0.24 ± 0.23 nm, 0.30 ± 0.34 nm, 0.38 ± 0.17 nm, and 0.44 ± 0.2 nm for 5, 10, 15, and 20 μg/mL tau-441, respectively (Figure 5.2a-d). 20 μg/ml tau-441 was further prepared in the diluted serum and the capture of tau-441 was also tracked with the plasmonic wavelength shift (Figure 5.2 f and g). The immobilization of the biotinylated antibodies was then investigated using ATR-FTIR, contact angle, surface topography analysis, and AFM etching tests. The first three analyses were performed on a layer-by-layer measurement method where each layer was analyzed individually before the addition of other layers. Therefore, the analysis was performed individually on the bare metasurface, medium-distance modification, avidin-FITC, and biotinylated anti-tau antibodies, respectively. The ATR-FTIR analysis confirmed the immobilization of biotinylated anti-tau antibodies over the medium-distance modification by the presence of the amid I and amid II groups (Figure 5.6) [226]. The contact angle

measurement depicted a drop in the contact angle after the addition of biotinylated anti-tau antibodies over the avidin-FITC functionalized medium-distance modification (Figure 5.4 d). This result suggested the immobilization of biotinylated anti-tau antibodies since the surface becomes more hydrophilic with the hydrophilic property of the antibodies at binding points [230]. The AFM etching test and surface topography analysis provided insights regarding the biotinylated anti-tau antibody's immobilization over the medium-distance modification and thickness of the medium-distance modification layer. In particular, the identification of the medium-distance modification and biotinylated anti-tau antibodies on the metasurface was confirmed by the EDX result obtained from the AFM tip which was utilized in the AFM scratching test (Figure 5.11).

The detection of Aβ 1-42 and tau-441 was confirmed and compared with the gold-standard method ELISA tests. In this experiment, Aβ 1-42 Human ELISA Kit and Human Tau colorimetric ELISA Kit were utilized using both PBS and serum samples. The concentration values applied to the ELISA kits were rearranged since the working range of the ELISA kits was in the 1-1000 pg/ml range. The Aβ 1-42 Human ELISA Kit determined 200, 400, 600, and 800 pg/ml for Aβ 1-42 both in PBS and serum with a linear range response in both types of sample (Figure 5.12). The Human Tau colorimetric ELISA Kit determined 100, 200, and 300 pg/ml for tau-441 both in PBS and serum with a linear range response for only serum samples (Figure 5.13). Our sensor platform has several advantages over the ELISA kits. The ELISA process consists of 8 steps in a multi-step detection protocol. These steps include sample incubation (1.5 hours), detection antibody incubation (1 hour), washing process (10 minutes), enzyme (HRP) incubation (30 minutes), washing process (10 minutes), color-generating substrate solution incubation (15-30 minutes), stop solution (5 minutes), and spectrometer measurement [244]–[246]. The total duration, varying from test to test, including sample preparation and washing steps, is approximately 5 hours (1 hour for standard and sample preparation, and 4 hours for the ELISA protocol). In contrary, our sensor requires only 3 steps (initial data measurement, sample application, and washing) and the biomarker can be detected within 20 minutes. Additionally, ELISA requires a large volume of antibodies and samples (100 μL of sample and 100 μL of antibody) [247], [248]. Moreover, our sensor is integrated with a microfluidic chip and requires much less sample and antibody volume (50-75 μL of sample and 10 μL of antibody). On the other hand, ELISA utilizes two

antibodies: one for capture and one for the detection of the biomarker. Our sensor requires only one antibody for the detection of AD biomarkers. Furthermore, ELISA kits are costly, with a complete kit costing around $750-1000, and the cost per well is approximately $9-10 (for 96 wells). Our sensor reduces the cost per sample to approximately $1.5, offering a platform 6-7 times cheaper alternative for ELISA kits.

In a nutshell, the coupling effect between fluorescence and plasmonic resonance was combined in a distance-dependent manner for obtaining a hybrid platform for the detection of biomolecules and biomarkers. Consequently, we aimed to develop a POC platform that follows RE-ASSURED qualifications for the detection of AD biomarkers. To provide an inexpensive biosensor platform, the metasurface was fabricated using off-shelf DVDs and integrated with lithography-free microfluidics. The sensitivity of the platform was aimed to be enhanced by the integration of fluorescent proteins on the metasurface. Therefore, the separation distance and spectral overlap were optimized accordingly. Our biosensor demonstrated sufficient analytical performance for the detection of AD biomarkers. The sensitivity of the metasurface platform was enhanced using fluorophores in a distance-dependent manner. The fluorophore-enhanced plasmonic metasurface demonstrated a linear response for the capture of tau-441; yet, it did not performed much sufficient for the case of Aβ 1-42. The LOD values were observed as 5 μg/mL for tau-441 and 100 μg/mL for Aβ 1-42. The detection ranges were 5-20 μg/mL for tau-441 and 100-400 μg/mL for Aβ 1-42. These LOD values could be further enhanced by increasing the refractive index sensitivity of the metasurface which can be obtained by changing the design of grating structures into finer nano-dimensional lattice geometries, such as nanopores, nanocrescent arrays, nanocavities, and asymmetric arrays. On the other hand, changing the fluorescence emitters that would enhance the plasmonic signals more would be another solution. Through such strategies, the LOD of the biosensor can be improved from μg/ml to lower concentration values such as, ng/ml or pg/ml, and this might extend dynamic linearity in the detection range. Selectivity is also a crucial element for preventing false-positive results. In this case, we applied serum samples including many other proteins rather than biomarkers of interest, and through our experiments, we did not encounter any significant wavelength shift towards the non-specific bound analytes rather than Aβ 1-42 and tau-441 in the serum experiments. This pointed out that our platform was selectively responding to the AD biomarkers and there

was no significant cross-reactivity observed. The repeatability of the biosensor at low concentrations was diminished, as indicated by the proximity of the error values to the wavelength shift values. This challenge can be improved by tracking refractive index of the biosensor while applying low concentrations of biomarkers. This platform paved the way for developing efficient and inexpensive methods for the diagnosis of AD. In addition, the idea of using fluorescent molecules integrated with different surface modifications for adjusting the separation distance can be utilized in also crystal vacancy investigation [249]. Furthermore, instead of using different surface modifications, a single aptamer can be also utilized for the fluorescence detection of biomarkers which provides a dynamic detection platform due to the conformational changes on the aptamer [135]. Therefore, this study provides new strategies for the integration of fluorophores on various platforms in a distance-controlled manner.

Bibliography

[1] E. P. Balogh, B. T. Miller, and J. R. Ball, “THE NATIONAL ACADEMIES PRESS Improving Diagnosis in Health Care,” 2015, doi: 10.17226/21794.

[2] “Point of Care Diagnostics Market Revenue Trends and Growth Drivers | MarketsandMarkets.” https://www.marketsandmarkets.com/Market-Reports/point-of-care-diagnostic-market-106829185.html (accessed May 24, 2023).

[3] “Mapping the landscape of diagnostics for sexually transmitted infections : key findings and recommendations / Hannah Kettler, Karen White, Sarah Hawkes.” https://apps.who.int/iris/handle/10665/68990 (accessed May 24, 2023).

[4] S. Smith, A. Oberholzer, K. Land, J. G. Korvink, and D. Mager, “Functional screen printed radio frequency identification tags on flexible substrates, facilitating low-cost and integrated point-of-care diagnostics,” *Flex. Print. Electron.*, vol. 3, no. 2, p. 025002, May 2018, doi: 10.1088/2058-8585/AABC8C.

[5] H. C. Ates *et al.*, “Integrated Devices for Non-Invasive Diagnostics,” *Adv. Funct. Mater.*, vol. 31, no. 15, 2021, doi: 10.1002/adfm.202010388.

[6] H. Sun, Y. Zheng, G. Shi, H. Haick, and M. Zhang, “Wearable Clinic: From Microneedle-Based Sensors to Next-Generation Healthcare Platforms,” *Small*, vol. 2207539, pp. 1–23, 2023, doi: 10.1002/smll.202207539.

[7] Y. Montes-Cebrián *et al.*, “‘Plug-and-Power’ Point-of-Care diagnostics: A novel approach for self-powered electronic reader-based portable analytical devices,” *Biosens. Bioelectron.*, vol. 118, pp. 88–96, Oct. 2018, doi: 10.1016/J.BIOS.2018.07.034.

[8] Y. Zhang, Y. Hu, N. Jiang, and A. K. Yetisen, “Wearable artificial intelligence biosensor networks,” *Biosens. Bioelectron.*, vol. 219, no. May 2022, p. 114825, 2023, doi: 10.1016/j.bios.2022.114825.

[9] M. Mayer and A. J. Baeumner, “A Megatrend Challenging Analytical Chemistry: Biosensor and Chemosensor Concepts Ready for the Internet of Things,” *Chem. Rev.*, vol. 119, no. 13, pp. 7996–8027, 2019, doi: 10.1021/acs.chemrev.8b00719.

[10] X. Jin, C. Liu, T. Xu, L. Su, and X. Zhang, “Artificial intelligence biosensors: Challenges and prospects,” *Biosens. Bioelectron.*, vol. 165, no. June, p. 112412, 2020, doi: 10.1016/j.bios.2020.112412.

[11] I. J. Higgins and C. R. Lowe, “Introduction to the principles and applications of biosensors,” *Philos. Trans. R. Soc. Lond. B. Biol. Sci.*, vol. 316, no. 1176, pp. 3–11, 1987, doi: 10.1098/rstb.1987.0013.

[12] J. D. Newman and S. J. Setford, “Enzymatic biosensors,” *Mol. Biotechnol.*, vol. 32, no. 3, pp. 249–268, 2006, doi: 10.1385/MB:32:3:249.

[13] P. R. Coulet, *Biosensor Principles and Applications: What is a biosensor?*, 1st ed., vol. 15. Boca Raton, Fluorida, 1991.

[14] Ö. Erdem, Y. Saylan, N. Cihangir, and A. Denizli, “Molecularly imprinted nanoparticles based plasmonic sensors for real-time Enterococcus faecalis detection,” *Biosens. Bioelectron.*, vol. 126, pp. 608–614, Feb. 2019, doi: 10.1016/J.BIOS.2018.11.030.

[15] Y. Aslan, M. Atabay, H. K. Chowdhury, I. Göktürk, Y. Saylan, and F. Inci, “Aptamer-Based Point-of-Care Devices: Emerging Technologies and Integration

of Computational Methods," *Biosens. 2023, Vol. 13, Page 569*, vol. 13, no. 5, p. 569, May 2023, doi: 10.3390/BIOS13050569.

[16] Q. Wang *et al.*, "Development of the DNA-based biosensors for high performance in detection of molecular biomarkers: More rapid, sensitive, and universal," *Biosens. Bioelectron.*, vol. 197, p. 113739, Feb. 2022, doi: 10.1016/J.BIOS.2021.113739.

[17] G. Rocchitta *et al.*, "Enzyme Biosensors for Biomedical Applications: Strategies for Safeguarding Analytical Performances in Biological Fluids," *Sensors 2016, Vol. 16, Page 780*, vol. 16, no. 6, p. 780, May 2016, doi: 10.3390/S16060780.

[18] H. J. Chang *et al.*, "Programmable receptors enable bacterial biosensors to detect pathological biomarkers in clinical samples," *Nat. Commun. 2021 121*, vol. 12, no. 1, pp. 1–12, Sep. 2021, doi: 10.1038/s41467-021-25538-y.

[19] H. Shafiee *et al.*, "Emerging technologies for point-of-care management of HIV infection," *Annu. Rev. Med.*, vol. 66, pp. 387–405, Jan. 2015, doi: 10.1146/ANNUREV-MED-092112-143017.

[20] S. Q. Wang, F. Inci, G. De Libero, A. Singhal, and U. Demirci, "Point-of-care assays for tuberculosis: Role of nanotechnology/microfluidics," *Biotechnol. Adv.*, vol. 31, no. 4, pp. 438–449, Jul. 2013, doi: 10.1016/J.BIOTECHADV.2013.01.006.

[21] S. Viswanathan *et al.*, "Graphene–protein field effect biosensors: glucose sensing," *Mater. Today*, vol. 18, no. 9, pp. 513–522, Nov. 2015, doi: 10.1016/J.MATTOD.2015.04.003.

[22] A. Sadana and N. Sadana, "Modeling and Theory," *Handb. Biosens. Biosens. Kinet.*, pp. 15–33, 2011, doi: 10.1016/b978-0-444-53262-6.00002-4.

[23] A. Singh *et al.*, "Recent Advances in Electrochemical Biosensors: Applications, Challenges, and Future Scope," *Biosens. 2021, Vol. 11, Page 336*, vol. 11, no. 9, p. 336, Sep. 2021, doi: 10.3390/BIOS11090336.

[24] C. Chen and J. Wang, "Optical biosensors: An exhaustive and comprehensive review," *Analyst*. 2020, doi: 10.1039/c9an01998g.

[25] F. Narita *et al.*, "A Review of Piezoelectric and Magnetostrictive Biosensor Materials for Detection of COVID-19 and Other Viruses," *Adv. Mater.*, vol. 33, no. 1, p. 2005448, Jan. 2021, doi: 10.1002/ADMA.202005448.

[26] M. Khorshid, S. B. Sichani, P. Cornelis, G. Wackers, and P. Wagner, "The hot-wire concept: Towards a one-element thermal biosensor platform," *Biosens. Bioelectron.*, vol. 179, p. 113043, May 2021, doi: 10.1016/J.BIOS.2021.113043.

[27] L. Wang and J. Lin, "Recent advances on magnetic nanobead based biosensors: From separation to detection," *TrAC Trends Anal. Chem.*, vol. 128, p. 115915, Jul. 2020, doi: 10.1016/J.TRAC.2020.115915.

[28] J. Peña-Bahamonde, H. N. Nguyen, S. K. Fanourakis, and D. F. Rodrigues, "Recent advances in graphene-based biosensor technology with applications in life sciences," *J. Nanobiotechnology 2018 161*, vol. 16, no. 1, pp. 1–17, Sep. 2018, doi: 10.1186/S12951-018-0400-Z.

[29] L. C. Clark and C. Lyons, "ELECTRODE SYSTEMS FOR CONTINUOUS MONITORING IN CARDIOVASCULAR SURGERY," *Ann. N. Y. Acad. Sci.*, vol. 102, no. 1, pp. 29–45, Oct. 1962, doi: 10.1111/J.1749-6632.1962.TB13623.X.

[30] S. N. Raja and J. W. Severinghaus, "The Invention and Development of Blood Gas Analysis Apparatus," *Anesthesiology*, vol. 97, no. 1, pp. 253–256, Jul. 2002, doi: 10.1097/00000542-200207000-00031.

[31] R. Álvarez-DIduk, J. Orozco, and A. Merkoçi, “Paper strip-embedded graphene quantum dots: A screening device with a smartphone readout,” *Sci. Rep.*, vol. 7, no. 1, pp. 1–9, Dec. 2017, doi: 10.1038/S41598-017-01134-3.

[32] J. Krämer, L. M. Grimm, C. Zhong, M. Hirtz, and F. Biedermann, “A supramolecular cucurbit[8]uril-based rotaxane chemosensor for the optical tryptophan detection in human serum and urine,” *Nat. Commun.*, vol. 14, no. 1, pp. 1–15, Jan. 2023, doi: 10.1038/s41467-023-36057-3.

[33] G. Oudeng *et al.*, “Droplet Microarray Based on Nanosensing Probe Patterns for Simultaneous Detection of Multiple HIV Retroviral Nucleic Acids,” *ACS Appl. Mater. Interfaces*, vol. 12, no. 50, pp. 55614–55623, Dec. 2020, doi: 10.1021/ACSAMI.0C16146/ASSET/IMAGES/LARGE/AM0C16146_0008.JPEG.

[34] D. H. Shin, X. Yang, and S. Caneva, “Single-Molecule Protein Fingerprinting with Photonic Hexagonal Boron Nitride Nanopores,” *Accounts Mater. Res.*, vol. 2023, p. 310, Apr. 2023, doi: 10.1021/ACCOUNTSMR.3C00016/ASSET/IMAGES/LARGE/MR3C00016_0003.JPEG.

[35] J. Fan, S. Zhang, F. Li, Y. Yang, and M. Du, “Recent advances in cellulose-based membranes for their sensing applications,” *Cellul. 2020 2716*, vol. 27, no. 16, pp. 9157–9179, Sep. 2020, doi: 10.1007/S10570-020-03445-7.

[36] K. Bethke *et al.*, “Functionalized Cellulose for Water Purification, Antimicrobial Applications, and Sensors,” *Adv. Funct. Mater.*, vol. 28, no. 23, p. 1800409, Jun. 2018, doi: 10.1002/ADFM.201800409.

[37] S. Kim, A. N. Mitropoulos, J. D. Spitzberg, H. Tao, D. L. Kaplan, and F. G. Omenetto, “Silk inverse opals,” vol. 6, no. 12, Nov. 2012, Accessed: May 29, 2023. [Online]. Available: https://www.nature.com/articles/nphoton.2012.264.

[38] A. Bolotsky *et al.*, “Two-Dimensional Materials in Biosensing and Healthcare: From in Vitro Diagnostics to Optogenetics and beyond,” *ACS Nano*, vol. 13, no. 9, pp. 9781–9810, May 2019, doi: 10.1021/ACSNANO.9B03632/ASSET/IMAGES/LARGE/NN9B03632_0009.JPEG.

[39] R. Rao *et al.*, “Carbon Nanotubes and Related Nanomaterials: Critical Advances and Challenges for Synthesis toward Mainstream Commercial Applications,” *ACS Nano*, vol. 12, no. 12, pp. 11756–11784, Dec. 2018, doi: 10.1021/ACSNANO.8B06511/ASSET/IMAGES/LARGE/NN-2018-06511Q_0006.JPEG.

[40] T. Pinheiro *et al.*, “Paper-Based Biosensors for COVID-19: A Review of Innovative Tools for Controlling the Pandemic,” *ACS Omega*, vol. 6, no. 44, pp. 29268–29290, Nov. 2021, doi: 10.1021/ACSOMEGA.1C04012/ASSET/IMAGES/LARGE/AO1C04012_0010.JPEG.

[41] C. Parolo *et al.*, “Tutorial: design and fabrication of nanoparticle-based lateral-flow immunoassays,” *Nat. Protoc.*, vol. 15, no. 12, pp. 3788–3816, 2020, doi: 10.1038/s41596-020-0357-x.

[42] M. Artigues, J. Gilabert-Porres, R. Texidó, S. Borrós, J. Abellà, and S. Colominas, “Analytical Parameters of a Novel Glucose Biosensor Based on Grafted PFM as a Covalent Immobilization Technique,” *Sensors 2021, Vol. 21, Page 4185*, vol. 21, no. 12, p. 4185, Jun. 2021, doi: 10.3390/S21124185.

[43] Y. Mazouzi *et al.*, "Design and Analytical Performances of a Diclofenac Biosensor for Water Resources Monitoring," *ACS Sensors*, vol. 6, no. 9, pp. 3485–3493, Sep. 2021, doi: 10.1021/ACSSENSORS.1C01607/ASSET/IMAGES/LARGE/SE1C01607_0008.JPEG.
[44] A. Sadana and N. Sadana, "Biosensor Performance Parameters and their Enhancement," *Fractal Anal. Bind. Dissociation Kinet. Differ. Anal. Biosens. Surfaces*, pp. 19–53, Jan. 2008, doi: 10.1016/B978-044453010-3.50004-9.
[45] Á. Lavín *et al.*, "On the Determination of Uncertainty and Limit of Detection in Label-Free Biosensors," *Sensors 2018, Vol. 18, Page 2038*, vol. 18, no. 7, p. 2038, Jun. 2018, doi: 10.3390/S18072038.
[46] A. Belushkin *et al.*, "Rapid and Digital Detection of Inflammatory Biomarkers Enabled by a Novel Portable Nanoplasmonic Imager," *Small*, vol. 16, no. 3, 2020, doi: 10.1002/smll.201906108.
[47] N. Verma and A. Bhardwaj, "Biosensor Technology for Pesticides—A review," *Appl. Biochem. Biotechnol.*, vol. 175, no. 6, pp. 3093–3119, Mar. 2015, doi: 10.1007/S12010-015-1489-2/FIGURES/6.
[48] G. Figueroa-Miranda *et al.*, "Aptamer-based electrochemical biosensor for highly sensitive and selective malaria detection with adjustable dynamic response range and reusability," *Sensors Actuators B Chem.*, vol. 255, pp. 235–243, Feb. 2018, doi: 10.1016/J.SNB.2017.07.117.
[49] L. C. Chen *et al.*, "Improving the reproducibility, accuracy, and stability of an electrochemical biosensor platform for point-of-care use," *Biosens. Bioelectron.*, vol. 155, p. 112111, May 2020, doi: 10.1016/J.BIOS.2020.112111.
[50] J. F. Masson, "Consideration of Sample Matrix Effects and 'biological' Noise in Optimizing the Limit of Detection of Biosensors," *ACS Sensors*, vol. 5, no. 11, pp. 3290–3292, Nov. 2020, doi: 10.1021/ACSSENSORS.0C02254/ASSET/IMAGES/MEDIUM/SE0C02254_0001.GIF.
[51] S. Gupta, A. Sharma, and R. S. Verma, "Polymers in biosensor devices for cardiovascular applications," *Curr. Opin. Biomed. Eng.*, vol. 13, pp. 69–75, Mar. 2020, doi: 10.1016/J.COBME.2019.10.002.
[52] D. A. Armbruster and T. Pry, "Limit of Blank, Limit of Detection and Limit of Quantitation," *Clin. Biochem. Rev.*, vol. 29, no. Suppl 1, p. S49, Aug. 2008, Accessed: Jul. 20, 2023. [Online]. Available: /pmc/articles/PMC2556583/.
[53] S. B. VanEngelenburg and A. E. Palmer, "Fluorescent biosensors of protein function," *Curr. Opin. Chem. Biol.*, vol. 12, no. 1, pp. 60–65, Feb. 2008, doi: 10.1016/J.CBPA.2008.01.020.
[54] O. Simoska and K. J. Stevenson, "Electrochemical sensors for rapid diagnosis of pathogens in real time," *Analyst*, vol. 144, no. 22, pp. 6461–6478, Nov. 2019, doi: 10.1039/C9AN01747J.
[55] V. Vogiazi, A. De La Cruz, S. Mishra, V. Shanov, W. R. Heineman, and D. D. Dionysiou, "A Comprehensive Review: Development of Electrochemical Biosensors for Detection of Cyanotoxins in Freshwater," *ACS Sensors*, vol. 4, no. 5, pp. 1151–1173, May 2019, doi: 10.1021/ACSSENSORS.9B00376/ASSET/IMAGES/LARGE/SE-2019-003768_0004.JPEG.
[56] M. Feyziazar *et al.*, "Recent advances on the piezoelectric, electrochemical, and

optical biosensors for the detection of protozoan pathogens," *TrAC Trends Anal. Chem.*, vol. 157, p. 116803, Dec. 2022, doi: 10.1016/J.TRAC.2022.116803.

[57] G. G. Guilbault and J. M. Jordan, "Analytical Uses of Piezoelectric Crystals: A Review," *http://dx.doi.org/10.1080/10408348808542806*, vol. 19, no. 1, pp. 1–28, 2008, doi: 10.1080/10408348808542806.

[58] M. Soler, C. S. Huertas, and L. M. Lechuga, "Label-free plasmonic biosensors for point-of-care diagnostics: a review," *Expert Rev. Mol. Diagn.*, vol. 19, no. 1, pp. 71–81, 2019, doi: 10.1080/14737159.2019.1554435.

[59] L. G. Carrascosa, C. S. Huertas, and L. M. Lechuga, "Prospects of optical biosensors for emerging label-free RNA analysis," *TrAC Trends Anal. Chem.*, vol. 80, pp. 177–189, Jun. 2016, doi: 10.1016/J.TRAC.2016.02.018.

[60] R. Peltomaa, B. Glahn-Martínez, E. Benito-Peña, and M. C. Moreno-Bondi, "Optical Biosensors for Label-Free Detection of Small Molecules," *Sensors 2018, Vol. 18, Page 4126*, vol. 18, no. 12, p. 4126, Nov. 2018, doi: 10.3390/S18124126.

[61] S. M. Yoo and S. Y. Lee, "Optical Biosensors for the Detection of Pathogenic Microorganisms," *Trends Biotechnol.*, vol. 34, no. 1, pp. 7–25, Jan. 2016, doi: 10.1016/j.tibtech.2015.09.012.

[62] V. Gaudin, "Advances in biosensor development for the screening of antibiotic residues in food products of animal origin – A comprehensive review," *Biosens. Bioelectron.*, vol. 90, pp. 363–377, Apr. 2017, doi: 10.1016/J.BIOS.2016.12.005.

[63] H. Malekzad *et al.*, "Noble metal nanostructures in optical biosensors: Basics, and their introduction to anti-doping detection," *TrAC Trends Anal. Chem.*, vol. 100, pp. 116–135, Mar. 2018, doi: 10.1016/J.TRAC.2017.12.006.

[64] E. J. Heller, R. L. Sundberg, and D. Tanner1, "Simple Aspects of Raman Scattering," *J. Phys. Chem*, vol. 86, pp. 1822–1833, 1982, Accessed: Jul. 20, 2023. [Online]. Available: https://pubs.acs.org/sharingguidelines.

[65] B. T. Hakan Inana, Muhammet Poyraza, b, Fatih Incia, Mark A. Lifsona, Murat Badaya and and U. D. Cunninghamc, "Photonic crystals: emerging biosensors and their promise for point-of-care applications," *Physiol. Behav.*, vol. 176, no. 5, pp. 139–148, 2017, doi: 10.1039/c6cs00206d.Photonic.

[66] D. Yu, M. Humar, K. Meserve, R. C. Bailey, S. N. Chormaic, and F. Vollmer, "Whispering-gallery-mode sensors for biological and physical sensing," *Nat. Rev. Methods Prim. 2021 11*, vol. 1, no. 1, pp. 1–22, Dec. 2021, doi: 10.1038/s43586-021-00079-2.

[67] A. Mataji-Kojouri, M. O. Ozen, M. Shahabadi, F. Inci, and U. Demirci, "Entangled Nanoplasmonic Cavities for Estimating Thickness of Surface-Adsorbed Layers," *ACS Nano*, vol. 14, no. 7, pp. 8518–8527, Jul. 2020, doi: 10.1021/acsnano.0c02797.

[68] F. Inci *et al.*, "Enhancing the nanoplasmonic signal by a nanoparticle sandwiching strategy to detect viruses," *Appl. Mater. Today*, vol. 20, p. 100709, Sep. 2020, doi: 10.1016/j.apmt.2020.100709.

[69] P. Fechner, G. Gauglitz, and G. Proll, "Through the looking-glass - Recent developments in reflectometry open new possibilities for biosensor applications," *TrAC Trends Anal. Chem.*, vol. 156, p. 116708, Nov. 2022, doi: 10.1016/J.TRAC.2022.116708.

[70] L. Möckl and W. E. Moerner, "Super-resolution Microscopy with Single Molecules in Biology and Beyond-Essentials, Current Trends, and Future Challenges," *J. Am. Chem. Soc.*, vol. 142, no. 42, pp. 17828–17844, Oct. 2020,

doi: 10.1021/JACS.0C08178/ASSET/IMAGES/LARGE/JA0C08178_0006.JPEG.
[71] H. He, C. Wu, M. Saqib, and R. Hao, "Single-molecule fluorescence methods for protein biomarker analysis," *Anal. Bioanal. Chem.*, vol. 415, no. 18, pp. 3655–3669, Jul. 2023, doi: 10.1007/S00216-022-04502-9/FIGURES/4.
[72] S. Kasetsirikul, M. J. A. Shiddiky, and N. T. Nguyen, "Challenges and perspectives in the development of paper-based lateral flow assays," *Microfluid. Nanofluidics 2020 242*, vol. 24, no. 2, pp. 1–18, Feb. 2020, doi: 10.1007/S10404-020-2321-Z.
[73] J. Budd *et al.*, "Lateral flow test engineering and lessons learned from COVID-19," *Nat. Rev. Bioeng. 2023 11*, vol. 1, no. 1, pp. 13–31, Jan. 2023, doi: 10.1038/s44222-022-00007-3.
[74] T. Mahmoudi, M. de la Guardia, and B. Baradaran, "Lateral flow assays towards point-of-care cancer detection: A review of current progress and future trends," *TrAC Trends Anal. Chem.*, vol. 125, p. 115842, Apr. 2020, doi: 10.1016/J.TRAC.2020.115842.
[75] T. Mahmoudi, M. de la Guardia, B. Shirdel, A. Mokhtarzadeh, and B. Baradaran, "Recent advancements in structural improvements of lateral flow assays towards point-of-care testing," *TrAC Trends Anal. Chem.*, vol. 116, pp. 13–30, Jul. 2019, doi: 10.1016/J.TRAC.2019.04.016.
[76] O. Tokel, F. Inci, and U. Demirci, "Advances in plasmonic technologies for point of care applications," *Chem. Rev.*, vol. 114, no. 11, pp. 5728–5752, 2014, doi: 10.1021/cr4000623.
[77] F. Inci *et al.*, "Multitarget, quantitative nanoplasmonic electrical field-enhanced resonating device (NE2RD) for diagnostics.," *Proc. Natl. Acad. Sci. U. S. A.*, vol. 112, no. 32, pp. E4354-63, Aug. 2015, doi: 10.1073/pnas.1510824112.
[78] F. Inci, Y. Saylan, A. M. Kojouri, M. G. Ogut, A. Denizli, and U. Demirci, "A disposable microfluidic-integrated hand-held plasmonic platform for protein detection," *Appl. Mater. Today*, vol. 18, no. xxxx, pp. 14–16, 2020, doi: 10.1016/j.apmt.2019.100478.
[79] X. Guo, "Surface plasmon resonance based biosensor technique: A review," *J. Biophotonics*, vol. 5, no. 7, pp. 483–501, 2012, doi: 10.1002/jbio.201200015.
[80] N. Andam, S. Refki, S. Hayashi, and Z. Sekkat, "Plasmonic mode coupling and thin film sensing in metal–insulator–metal structures," *Sci. Reports 2021 111*, vol. 11, no. 1, pp. 1–12, Jul. 2021, doi: 10.1038/s41598-021-94143-2.
[81] L. Tao, S. Deng, H. Gao, H. Lv, X. Wen, and M. Li, "Experimental Investigation of the Dielectric Constants of Thin Noble Metallic Films Using a Surface Plasmon Resonance Sensor," *Sensors 2020, Vol. 20, Page 1505*, vol. 20, no. 5, p. 1505, Mar. 2020, doi: 10.3390/S20051505.
[82] G. Zheng *et al.*, "Discrete metal nanoparticles with plasmonic chirality," *Chem. Soc. Rev.*, vol. 50, no. 6, pp. 3738–3754, Mar. 2021, doi: 10.1039/C9CS00765B.
[83] F. Fathi, M. R. Rashidi, and Y. Omidi, "Ultra-sensitive detection by metal nanoparticles-mediated enhanced SPR biosensors," *Talanta*, vol. 192, pp. 118–127, Jan. 2019, doi: 10.1016/J.TALANTA.2018.09.023.
[84] D. T. Nurrohman, Y. H. Wang, and N. F. Chiu, "Exploring Graphene and MoS2 Chips Based Surface Plasmon Resonance Biosensors for Diagnostic Applications," *Front. Chem.*, vol. 8, p. 566658, Aug. 2020, doi: 10.3389/FCHEM.2020.00728/BIBTEX.
[85] S. Kaushik, U. K. Tiwari, A. Deep, and R. K. Sinha, "Two-dimensional transition

metal dichalcogenides assisted biofunctionalized optical fiber SPR biosensor for efficient and rapid detection of bovine serum albumin," *Sci. Reports 2019 91*, vol. 9, no. 1, pp. 1–11, May 2019, doi: 10.1038/s41598-019-43531-w.

[86] Q. Wu *et al.*, "A 2D transition metal carbide MXene-based SPR biosensor for ultrasensitive carcinoembryonic antigen detection," *Biosens. Bioelectron.*, vol. 144, p. 111697, Nov. 2019, doi: 10.1016/J.BIOS.2019.111697.

[87] H. Wang *et al.*, "Recent progress in terahertz biosensors based on artificial electromagnetic subwavelength structure," *TrAC Trends Anal. Chem.*, vol. 158, p. 116888, Jan. 2023, doi: 10.1016/J.TRAC.2022.116888.

[88] A. Guha *et al.*, "Direct detection of small molecules using a nano-molecular imprinted polymer receptor and a quartz crystal resonator driven at a fixed frequency and amplitude," *Biosens. Bioelectron.*, vol. 158, p. 112176, Jun. 2020, doi: 10.1016/J.BIOS.2020.112176.

[89] P. Steglich and R. B. M. Schasfoort, "Surface Plasmon Resonance Imaging (SPRi) and Photonic Integrated Circuits (PIC) for COVID-19 Severity Monitoring," *COVID 2022, Vol. 2, Pages 389-397*, vol. 2, no. 3, pp. 389–397, Mar. 2022, doi: 10.3390/COVID2030027.

[90] B. Wang and B. Park, "Immunoassay Biosensing of Foodborne Pathogens with Surface Plasmon Resonance Imaging: A Review," *J. Agric. Food Chem.*, vol. 68, no. 46, pp. 12927–12939, Nov. 2020, doi: 10.1021/ACS.JAFC.0C02295/ASSET/IMAGES/LARGE/JF0C02295_0007.JPEG.

[91] A. Uniyal, G. Srivastava, A. Pal, S. Taya, and A. Muduli, "Recent Advances in Optical Biosensors for Sensing Applications: a Review," *Plasmon. 2023 182*, vol. 18, no. 2, pp. 735–750, Feb. 2023, doi: 10.1007/S11468-023-01803-2.

[92] A. John-Herpin *et al.*, "Infrared Metasurface Augmented by Deep Learning for Monitoring Dynamics between All Major Classes of Biomolecules," *Adv. Mater.*, vol. 33, no. 14, p. 2006054, Apr. 2021, doi: 10.1002/ADMA.202006054.

[93] Y. Jahani *et al.*, "Imaging-based spectrometer-less optofluidic biosensors based on dielectric metasurfaces for detecting extracellular vesicles," *Nat. Commun.*, vol. 12, no. 1, pp. 4–13, May 2021, doi: 10.1038/s41467-021-23257-y.

[94] H. Lísalová *et al.*, "Ultralow-Fouling Behavior of Biorecognition Coatings Based on Carboxy-Functional Brushes of Zwitterionic Homo- and Copolymers in Blood Plasma: Functionalization Matters," *Anal. Chem.*, vol. 89, no. 6, pp. 3524–3531, Mar. 2017, doi: 10.1021/ACS.ANALCHEM.6B04731/SUPPL_FILE/AC6B04731_SI_001.PDF.

[95] H. Altug, S. H. Oh, S. A. Maier, and J. Homola, "Advances and applications of nanophotonic biosensors," *Nat. Nanotechnol.*, vol. 17, no. 1, pp. 5–16, 2022, doi: 10.1038/s41565-021-01045-5.

[96] G. Atam Akceoglu, Y. Saylan, F. Inci, G. A. Akceoglu, Y. Saylan, and F. Inci, "A Snapshot of Microfluidics in Point-of-Care Diagnostics: Multifaceted Integrity with Materials and Sensors," *Adv. Mater. Technol.*, vol. 6, no. 7, p. 2100049, Jul. 2021, doi: 10.1002/admt.202100049.

[97] S. Ansaryan *et al.*, "High-throughput spatiotemporal monitoring of single-cell secretions via plasmonic microwell arrays," *Nat. Biomed. Eng. 2023*, pp. 1–16, Apr. 2023, doi: 10.1038/s41551-023-01017-1.

[98] W. L. Barnes, A. Dereux, and T. W. Ebbesen, "Surface plasmon subwavelength optics," *Nature*, vol. 424, no. 6950, pp. 824–830, 2003, doi: 10.1038/nature01937.

[99] W. Xu *et al.*, "Gold Nanoparticle-Based Terahertz Metamaterial Sensors: Mechanisms and Applications," *ACS Photonics*, vol. 3, no. 12, pp. 2308–2314, Dec. 2016, doi: 10.1021/ACSPHOTONICS.6B00463/ASSET/IMAGES/LARGE/PH-2016-00463Z_0005.JPEG.

[100] K. T. Tsai *et al.*, "Looking into meta-atoms of plasmonic nanowire metamaterial," *Nano Lett.*, vol. 14, no. 9, pp. 4971–4976, Sep. 2014, doi: 10.1021/NL501283C/SUPPL_FILE/NL501283C_SI_001.PDF.

[101] N. Vasilantonakis, M. E. Nasir, W. Dickson, G. A. Wurtz, and A. V. Zayats, "Bulk plasmon-polaritons in hyperbolic nanorod metamaterial waveguides," *Laser Photon. Rev.*, vol. 9, no. 3, pp. 345–353, May 2015, doi: 10.1002/LPOR.201400457.

[102] K. Yang *et al.*, "Large-Area Plasmonic Metamaterial with Thickness-Dependent Absorption," *Adv. Opt. Mater.*, vol. 9, no. 1, p. 2001375, Jan. 2021, doi: 10.1002/ADOM.202001375.

[103] B. J. Roxworthy and K. C. Toussaint, "Simultaneously tuning the electric and magnetic plasmonic response using capped bi-metallic nanoantennas," *Nanoscale*, vol. 6, no. 4, pp. 2270–2274, Jan. 2014, doi: 10.1039/C3NR05536A.

[104] M. R. Shcherbakov, M. I. Dobynde, T. V. Dolgova, D. P. Tsai, and A. A. Fedyanin, "Full Poincaré sphere coverage with plasmonic nanoslit metamaterials at Fano resonance," *Phys. Rev. B - Condens. Matter Mater. Phys.*, vol. 82, no. 19, p. 193402, Nov. 2010, doi: 10.1103/PHYSREVB.82.193402/FIGURES/4/MEDIUM.

[105] N. Fang, H. Lee, C. Sun, and X. Zhang, "Sub-diffraction-limited optical imaging with a silver superlens," *Science (80-.).*, vol. 308, no. 5721, pp. 534–537, Apr. 2005, doi: 10.1126/SCIENCE.1108759/SUPPL_FILE/FANG.SOM.PDF.

[106] Z. Li, M. Mutlu, and E. Ozbay, "Chiral metamaterials: from optical activity and negative refractive index to asymmetric transmission," *J. Opt.*, vol. 15, no. 2, p. 023001, Jan. 2013, doi: 10.1088/2040-8978/15/2/023001.

[107] H. Yu, Y. Peng, Y. Yang, and Z. Y. Li, "Plasmon-enhanced light–matter interactions and applications," *npj Comput. Mater. 2019 51*, vol. 5, no. 1, pp. 1–14, Apr. 2019, doi: 10.1038/s41524-019-0184-1.

[108] R. Liu, C. Ji, J. J. Mock, J. Y. Chin, T. J. Cui, and D. R. Smith, "Broadband ground-plane cloak," *Science (80-.).*, vol. 323, no. 5912, pp. 366–369, Jan. 2009, doi: 10.1126/SCIENCE.1166949/SUPPL_FILE/LIUS5.MOV.

[109] C. Wu *et al.*, "Fano-resonant asymmetric metamaterials for ultrasensitive spectroscopy and identification of molecular monolayers," *Nat. Mater. 2011 111*, vol. 11, no. 1, pp. 69–75, Nov. 2011, doi: 10.1038/nmat3161.

[110] M. Boutria, R. Oussaid, D. Van Labeke, and F. I. Baida, "Tunable artificial chirality with extraordinary transmission metamaterials," *Phys. Rev. B - Condens. Matter Mater. Phys.*, vol. 86, no. 15, p. 155428, Oct. 2012, doi: 10.1103/PHYSREVB.86.155428/FIGURES/7/MEDIUM.

[111] J. Valentine *et al.*, "Three-dimensional optical metamaterial with a negative refractive index," *Nat. 2008 4557211*, vol. 455, no. 7211, pp. 376–379, Aug. 2008, doi: 10.1038/nature07247.

[112] A. Arbabi, E. Arbabi, Y. Horie, S. M. Kamali, and A. Faraon, "Planar metasurface retroreflector," *Nat. Photonics 2017 117*, vol. 11, no. 7, pp. 415–420, Jun. 2017, doi: 10.1038/nphoton.2017.96.

[113] M. Decker, N. Feth, C. M. Soukoulis, S. Linden, and M. Wegener, "Retarded long-range interaction in split-ring-resonator square arrays," *Phys. Rev. B - Condens. Matter Mater. Phys.*, vol. 84, no. 8, p. 085416, Aug. 2011, doi: 10.1103/PHYSREVB.84.085416/FIGURES/9/MEDIUM.
[114] I. Hwang *et al.*, "Ultrasensitive Molecule Detection Based on Infrared Metamaterial Absorber with Vertical Nanogap," *Small Methods*, vol. 5, no. 8, p. 2100277, Aug. 2021, doi: 10.1002/SMTD.202100277.
[115] J. Biener, G. W. Nyce, A. M. Hodge, M. M. Biener, A. V. Hamza, and S. A. Maier, "Nanoporous Plasmonic Metamaterials," *Adv. Mater.*, vol. 20, no. 6, pp. 1211–1217, Mar. 2008, doi: 10.1002/ADMA.200701899.
[116] Y. Jahani *et al.*, "Imaging-based spectrometer-less optofluidic biosensors based on dielectric metasurfaces for detecting extracellular vesicles," *Nat. Commun. 2021 121*, vol. 12, no. 1, pp. 1–10, May 2021, doi: 10.1038/s41467-021-23257-y.
[117] J. Zhu, Z. Wang, S. Lin, S. Jiang, X. Liu, and S. Guo, "Low-cost flexible plasmonic nanobump metasurfaces for label-free sensing of serum tumor marker," *Biosens. Bioelectron.*, vol. 150, p. 111905, Feb. 2020, doi: 10.1016/J.BIOS.2019.111905.
[118] D. Conteduca, S. D. Quinn, and T. F. Krauss, "Dielectric metasurface for high-precision detection of large unilamellar vesicles," *J. Opt.*, vol. 23, no. 11, p. 114002, Oct. 2021, doi: 10.1088/2040-8986/AC2DD7.
[119] F. Li *et al.*, "Exploring near-field sensing efficiency of complementary plasmonic metasurfaces for immunodetection of tumor markers," *Biosens. Bioelectron.*, vol. 203, p. 114038, May 2022, doi: 10.1016/J.BIOS.2022.114038.
[120] R. Ahmed *et al.*, "Tunable Fano-Resonant Metasurfaces on a Disposable Plastic-Template for Multimodal and Multiplex Biosensing," *Adv. Mater.*, vol. 32, no. 19, pp. 1–11, May 2020, doi: 10.1002/adma.201907160.
[121] J. Stevenson-Hoare *et al.*, "Plasma biomarkers and genetics in the diagnosis and prediction of Alzheimer's disease," *Brain*, vol. 146, no. 2, pp. 690–699, Feb. 2023, doi: 10.1093/BRAIN/AWAC128.
[122] K. Sagdic and F. Inci, "Smart Material-Integrated Systems for Isolation and Profiling of Rare Cancer Cells and Emboli," *Adv. Eng. Mater.*, vol. 24, no. 3, pp. 1–18, Nov. 2022, doi: 10.1002/adem.202100857.
[123] S. Z. Shirejini and F. Inci, "The Yin and Yang of exosome isolation methods: conventional practice, microfluidics, and commercial kits," *Biotechnol. Adv.*, vol. 54, no. August, p. 107814, Jan. 2022, doi: 10.1016/j.biotechadv.2021.107814.
[124] F. Arcadio *et al.*, "A Plasmonic Biosensor Based on Light-Diffusing Fibers Functionalized with Molecularly Imprinted Nanoparticles for Ultralow Sensing of Proteins," *Nanomater. 2022, Vol. 12, Page 1400*, vol. 12, no. 9, p. 1400, Apr. 2022, doi: 10.3390/NANO12091400.
[125] R. Ameling and H. Giessen, "Microcavity plasmonics: Strong coupling of photonic cavities and plasmons," *Laser Photonics Rev.*, vol. 7, no. 2, pp. 141–169, Mar. 2013, doi: 10.1002/lpor.201100041.
[126] V. Flauraud *et al.*, "Mode Evolution in Strongly Coupled Plasmonic Dolmens Fabricated by Templated Assembly," *ACS Photonics*, vol. 4, no. 7, pp. 1661–1668, 2017, doi: 10.1021/acsphotonics.6b01026.
[127] E. S. Melby *et al.*, "Cascading Effects of Nanoparticle Coatings: Surface Functionalization Dictates the Assemblage of Complexed Proteins and Subsequent Interaction with Model Cell Membranes," *ACS Nano*, vol. 11, no. 6, pp. 5489–5499, Jun. 2017, doi: 10.1021/ACSNANO.7B00231/ASSET/IMAGES/NN-2017-

002319_M001.GIF.
[128] S.-G. Park *et al.*, "Self-Assembly of Nanoparticle-Spiked Pillar Arrays for Plasmonic Biosensing," *Adv. Funct. Mater.*, vol. 29, no. 43, p. 1904257, Oct. 2019, doi: 10.1002/ADFM.201904257.
[129] Z. Yi, X. Y. Li, F. J. Liu, P. Y. Jin, X. Chu, and R. Q. Yu, "Design of label-free, homogeneous biosensing platform based on plasmonic coupling and surface-enhanced Raman scattering using unmodified gold nanoparticles," *Biosens. Bioelectron.*, vol. 43, no. 1, pp. 308–314, May 2013, doi: 10.1016/J.BIOS.2012.12.002.
[130] F. Stein, A. Schielke, S. Barcikowski, and C. Rehbock, "Influence of Gold/Silver Ratio in Ablative Nanoparticles on Their Interaction with Aptamers and Functionality of the Obtained Conjugates," *Bioconjug. Chem.*, vol. 32, no. 11, pp. 2439–2446, Nov. 2021, doi: 10.1021/ACS.BIOCONJCHEM.1C00468/ASSET/IMAGES/LARGE/BC1C00468_0005.JPEG.
[131] F. Liang, Y. Guo, S. Hou, and Q. Quan, "Photonic-plasmonic hybrid single-molecule nanosensor measures the effect of fluorescent labels on DNA-protein dynamics," *Sci. Adv.*, vol. 3, no. 5, May 2017, doi: 10.1126/SCIADV.1602991/SUPPL_FILE/1602991_SM.PDF.
[132] J. Liu *et al.*, "Spatially defined molecular emitters coupled to plasmonic nanoparticle arrays," *Proc. Natl. Acad. Sci. U. S. A.*, vol. 116, no. 13, pp. 5925–5930, Mar. 2019, doi: 10.1073/PNAS.1818902116/SUPPL_FILE/PNAS.1818902116.SAPP.PDF.
[133] Y. Ji *et al.*, "Supersensitive sensing based on upconversion nanoparticles through cascade photon amplification at single-particle level," *Sensors Actuators B Chem.*, vol. 367, p. 132125, Sep. 2022, doi: 10.1016/J.SNB.2022.132125.
[134] F. Zou, H. Zhou, T. Van Tan, J. Kim, K. Koh, and J. Lee, "Dual-Mode SERS-Fluorescence Immunoassay Using Graphene Quantum Dot Labeling on One-Dimensional Aligned Magnetoplasmonic Nanoparticles," *ACS Appl. Mater. Interfaces*, vol. 7, no. 22, pp. 12168–12175, Jun. 2015, doi: 10.1021/ACSAMI.5B02523/SUPPL_FILE/AM5B02523_SI_001.PDF.
[135] A. Minopoli *et al.*, "Ultrasensitive antibody-aptamer plasmonic biosensor for malaria biomarker detection in whole blood," *Nat. Commun.*, vol. 11, no. 1, pp. 1–10, Dec. 2020, doi: 10.1038/s41467-020-19755-0.
[136] D. Zhang, K. Wang, W. Wei, Y. Liu, and S. Liu, "Multifunctional Plasmonic Core-Satellites Nanoprobe for Cancer Diagnosis and Therapy Based on a Cascade Reaction Induced by MicroRNA," *Anal. Chem.*, vol. 93, no. 27, pp. 9521–9530, Jul. 2021, doi: 10.1021/ACS.ANALCHEM.1C01539/ASSET/IMAGES/LARGE/AC1C01539_0006.JPEG.
[137] S. M. Sundaresan, S. M. Fothergill, T. A. Tabish, M. Ryan, and F. Xie, "Aptamer biosensing based on metal enhanced fluorescence platform: A promising diagnostic tool," *Appl. Phys. Rev.*, vol. 8, no. 4, Dec. 2021, doi: 10.1063/5.0065833.
[138] K. R. Spring, "Detectors for fluorescence microscopy," *Scanning Microsc.*, vol. 5, no. 1, pp. 63–69, Mar. 1991, doi: 10.1007/978-1-4614-7513-2_3/COVER.
[139] T. T. Nguyen, V. T. Tran, J. S. Seok, J. H. Lee, and H. Ju, "Quantum Dot-Induced Blue Shift of Surface Plasmon Spectroscopy," *Nanomaterials*, vol. 12, no. 12, p.

2076, Jun. 2022, doi: 10.3390/nano12122076.
[140] M. Li, S. K. Cushing, and N. Wu, “Plasmon-enhanced optical sensors: A review,” *Analyst*, vol. 140, no. 2, pp. 386–406, Dec. 2015, doi: 10.1039/c4an01079e.
[141] J. R. Lakowicz, “Radiative decay engineering 5: Metal-enhanced fluorescence and plasmon emission,” *Anal. Biochem.*, vol. 337, no. 2, pp. 171–194, 2005, doi: 10.1016/j.ab.2004.11.026.
[142] J. R. Lakowicz *et al.*, “Advances in Surface-Enhanced Fluorescence,” vol. 14, no. 4, pp. 425–441, 2004.
[143] J. R. Lakowicz, “Plasmonics in biology and plasmon-controlled fluorescence,” *Plasmonics*, vol. 1, no. 1, pp. 5–33, 2006, doi: 10.1007/s11468-005-9002-3.
[144] G. W. Ford and W. H. Weber, “Electromagnetic interactions of molecules with metal surfaces,” *Phys. Rep.*, vol. 113, no. 4, pp. 195–287, Nov. 1984, doi: 10.1016/0370-1573(84)90098-X.
[145] Q. Su, C. Jiang, D. Gou, and Y. Long, “Surface Plasmon-Assisted Fluorescence Enhancing and Quenching: From Theory to Application,” *ACS Appl. Bio Mater.*, vol. 4, no. 6, pp. 4684–4705, Jun. 2021, doi: 10.1021/ACSABM.1C00320/ASSET/IMAGES/LARGE/MT1C00320_0017.JPEG.
[146] C. D. Geddes and J. R. Lakowicz, “Metal-Enhanced Fluorescence,” *J. Fluoresc.*, vol. 12, no. 2, pp. 121–129, Jun. 2002, doi: 10.1023/A:1016875709579/METRICS.
[147] Y. C. Tsai, C. F. Lin, and J. W. Chang, “Controlling spontaneous emission with the local density of states of honeycomb photonic crystals,” *Opt. Rev. 2009 163*, vol. 16, no. 3, pp. 347–350, Jun. 2010, doi: 10.1007/S10043-009-0065-9.
[148] M. A. Badshah, N. Y. Koh, A. W. Zia, N. Abbas, Z. Zahra, and M. W. Saleem, “Recent Developments in Plasmonic Nanostructures for Metal Enhanced Fluorescence-Based Biosensing,” *Nanomater. 2020, Vol. 10, Page 1749*, vol. 10, no. 9, p. 1749, Sep. 2020, doi: 10.3390/NANO10091749.
[149] Y. Chen, K. Munechika, and D. S. Ginger, “Dependence of fluorescence intensity on the spectral overlap between fluorophores and plasmon resonant single silver nanoparticles,” *Nano Lett.*, vol. 7, no. 3, pp. 690–696, Mar. 2007, doi: 10.1021/NL062795Z/SUPPL_FILE/NL062795ZSI20070202_075909.PDF.
[150] A. Haleem, M. Javaid, R. P. Singh, R. Suman, and S. Rab, “Biosensors applications in medical field: A brief review,” *Sensors Int.*, vol. 2, p. 100100, Jan. 2021, doi: 10.1016/J.SINTL.2021.100100.
[151] “Dementia.” https://www.who.int/news-room/fact-sheets/detail/dementia (accessed Jun. 09, 2023).
[152] “Dementia statistics | Alzheimer’s Disease International (ADI).” https://www.alzint.org/about/dementia-facts-figures/dementia-statistics/ (accessed Jun. 09, 2023).
[153] R. Dahm, “Alzheimer’s discovery,” *Curr. Biol.*, vol. 16, no. 21, pp. R906–R910, Nov. 2006, doi: 10.1016/J.CUB.2006.09.056.
[154] G. F. Chen *et al.*, “Amyloid beta: Structure, biology and structure-based therapeutic development,” *Acta Pharmacol. Sin.*, vol. 38, no. 9, pp. 1205–1235, 2017, doi: 10.1038/aps.2017.28.
[155] S. E. Lesné *et al.*, “Brain amyloid-β oligomers in ageing and Alzheimer’s disease,” *Brain*, vol. 136, no. 5, pp. 1383–1398, 2013, doi: 10.1093/brain/awt062.
[156] T. Jiang, Q. Sun, and S. Chen, “Oxidative stress: A major pathogenesis and

potential therapeutic target of antioxidative agents in Parkinson's disease and Alzheimer's disease," *Prog. Neurobiol.*, vol. 147, pp. 1–19, Dec. 2016, doi: 10.1016/J.PNEUROBIO.2016.07.005.
[157] Y. Ju and K. Tam, "Pathological mechanisms and therapeutic strategies for Alzheimer's disease," *Neural Regen. Res.*, vol. 17, no. 3, pp. 543–549, Mar. 2022, doi: 10.4103/1673-5374.320970.
[158] M. Prinz, S. Jung, and J. Priller, "Microglia Biology: One Century of Evolving Concepts," *Cell*, vol. 179, no. 2, pp. 292–311, Oct. 2019, doi: 10.1016/J.CELL.2019.08.053.
[159] M. A. Busche and B. T. Hyman, "Synergy between amyloid-β and tau in Alzheimer's disease," *Nat. Neurosci. 2020 2310*, vol. 23, no. 10, pp. 1183–1193, Aug. 2020, doi: 10.1038/s41593-020-0687-6.
[160] K. R. Brunden, J. Q. Trojanowski, and V. M. Y. Lee, "Advances in tau-focused drug discovery for Alzheimer's disease and related tauopathies," *Nat. Rev. Drug Discov.*, vol. 8, no. 10, pp. 783–793, 2009, doi: 10.1038/nrd2959.
[161] R. C. Petersen, "How early can we diagnose Alzheimer disease (and is it sufficient)?," *Neurology*, vol. 91, no. 9, pp. 395–402, Aug. 2018, doi: 10.1212/WNL.0000000000006088.
[162] G. M. McKhann *et al.*, "The diagnosis of dementia due to Alzheimer's disease: Recommendations from the National Institute on Aging-Alzheimer's Association workgroups on diagnostic guidelines for Alzheimer's disease," *Alzheimer's Dement.*, vol. 7, no. 3, pp. 263–269, May 2011, doi: 10.1016/J.JALZ.2011.03.005.
[163] S. Palmqvist *et al.*, "Detailed comparison of amyloid PET and CSF biomarkers for identifying early Alzheimer disease," *Neurology*, vol. 85, no. 14, pp. 1240–1249, Oct. 2015, doi: 10.1212/WNL.0000000000001991.
[164] J. P. Chhatwal *et al.*, "Temporal T807 binding correlates with CSF tau and phospho-tau in normal elderly," *Neurology*, vol. 87, no. 9, pp. 920–926, Aug. 2016, doi: 10.1212/WNL.0000000000003050.
[165] F. de Vos *et al.*, "Combining multiple anatomical MRI measures improves Alzheimer's disease classification," *Hum. Brain Mapp.*, vol. 37, no. 5, p. 1920, May 2016, doi: 10.1002/HBM.23147.
[166] W. Jagust, B. Reed, D. Mungas, W. Ellis, and C. DeCarli, "What does fluorodeoxyglucose PET imaging add to a clinical diagnosis of dementia?," *Neurology*, vol. 69, no. 9, pp. 871–877, Aug. 2007, doi: 10.1212/01.WNL.0000269790.05105.16.
[167] C. Wattmo, K. Blennow, and O. Hansson, "Cerebro-spinal fluid biomarker levels: Phosphorylated tau (T) and total tau (N) as markers for rate of progression in Alzheimer's disease," *BMC Neurol.*, vol. 20, no. 1, pp. 1–12, Jan. 2020, doi: 10.1186/S12883-019-1591-0/FIGURES/3.
[168] B. Dubois *et al.*, "Clinical diagnosis of Alzheimer's disease: recommendations of the International Working Group," *Lancet Neurol.*, vol. 20, no. 6, pp. 484–496, 2021, doi: 10.1016/S1474-4422(21)00066-1.
[169] C. R. Jack *et al.*, "NIA-AA Research Framework: Toward a biological definition of Alzheimer's disease," *Alzheimer's Dement.*, vol. 14, no. 4, pp. 535–562, Apr. 2018, doi: 10.1016/J.JALZ.2018.02.018.
[170] B. L. C. Wright, J. T. F. Lai, and A. J. Sinclair, "Cerebrospinal fluid and lumbar puncture: A practical review," *J. Neurol.*, vol. 259, no. 8, pp. 1530–1545, Aug. 2012, doi: 10.1007/S00415-012-6413-X/TABLES/5.

[171] O. Hansson *et al.*, "The Alzheimer's Association appropriate use recommendations for blood biomarkers in Alzheimer's disease," *Alzheimer's Dement.*, vol. 18, no. 12, pp. 2669–2686, Dec. 2022, doi: 10.1002/ALZ.12756.
[172] H. Hampel *et al.*, "Blood-based biomarkers for Alzheimer disease: mapping the road to the clinic," *Nat. Rev. Neurol.*, vol. 14, no. 11, pp. 639–652, 2018, doi: 10.1038/s41582-018-0079-7.
[173] C. E. Teunissen *et al.*, "Blood-based biomarkers for Alzheimer's disease: towards clinical implementation," *Lancet Neurol.*, vol. 21, no. 1, pp. 66–77, Jan. 2022, doi: 10.1016/S1474-4422(21)00361-6.
[174] Edward D. Palik, "Handbook of Optical Constants of Solids - Google Books," *Academic Press*, 1996. https://books.google.com.tr/books?hl=en&lr=&id=nxoqxyoHfbIC&oi=fnd&pg=PA3&dq=E.+D.+Palik,+Handbook+of+Optical+Constants,+Academic+Press+Inc.,+San+Diego&ots=EG4THBp6dd&sig=keTRgQDGzyB9jzB8kX8UBTwqKOg&redir_esc=y#v=onepage&q=E. D. Palik%2C Handbook of Optical Constants%2C Academic Press Inc.%2C San Diego&f=false (accessed Jul. 23, 2023).
[175] P. B. Johnson and R. W. Christy, "Optical Constants of the Noble Metals," *Phys. Rev. B*, vol. 6, no. 12, p. 4370, Dec. 1972, doi: 10.1103/PhysRevB.6.4370.
[176] E. Derin, "Biomaterial-integrated metasurfaces for biomarker detection," *Bilkent Univ.*, no. August, 2022, [Online]. Available: http://hdl.handle.net/11693/110468.
[177] S. H. Oh and H. Altug, "Performance metrics and enabling technologies for nanoplasmonic biosensors," *Nat. Commun.*, vol. 9, no. 1, pp. 1–5, 2018, doi: 10.1038/s41467-018-06419-3.
[178] C. J. Van Oss, R. F. Giese, P. M. Bronson, A. Docoslis, P. Edwards, and W. T. Ruyechan, "Macroscopic-scale surface properties of streptavidin and their influence on aspecific interactions between streptavidin and dissolved biopolymers," *Colloids Surfaces B Biointerfaces*, vol. 30, no. 1–2, pp. 25–36, 2003, doi: 10.1016/S0927-7765(03)00025-0.
[179] S. M. Sedlak *et al.*, "Monodisperse measurement of the biotin-streptavidin interaction strength in a well-defined pulling geometry," *PLoS One*, vol. 12, no. 12, pp. 1–16, 2017, doi: 10.1371/journal.pone.0188722.
[180] F. Oesterhelt, M. Rief, and H. E. Gaub, "Single molecule force spectroscopy by AFM indicates helical structure of poly(ethylene-glycol) in water," *New J. Phys.*, vol. 1, 1999, doi: 10.1088/1367-2630/1/1/006.
[181] P. Jonkheijm, D. Weinrich, H. Schröder, C. M. Niemeyer, and H. Waldmann, "Chemical strategies for generating protein biochips," *Angew. Chemie - Int. Ed.*, vol. 47, no. 50, pp. 9618–9647, 2008, doi: 10.1002/anie.200801711.
[182] C. S. Chen and H. Zhu, "Protein microarrays," *Biotechniques*, vol. 40, no. 4, pp. 423–429, May 2006, doi: 10.2144/06404TE01/ASSET/IMAGES/LARGE/FIGURE4.JPEG.
[183] E. Mohit, Z. Rostami, and H. Vahidi, "A comparative review of immunoassays for COVID-19 detection," *https://doi.org/10.1080/1744666X.2021.1908886*, vol. 17, no. 6, pp. 573–599, 2021, doi: 10.1080/1744666X.2021.1908886.
[184] S. Tharakan, O. Faqah, W. Asghar, and A. Ilyas, "Microfluidic Devices for HIV Diagnosis and Monitoring at Point-of-Care (POC) Settings," *Biosens. 2022, Vol. 12, Page 949*, vol. 12, no. 11, p. 949, Nov. 2022, doi: 10.3390/BIOS12110949.
[185] D. N. G. Krishna and J. Philip, "Review on surface-characterization applications

of X-ray photoelectron spectroscopy (XPS): Recent developments and challenges," *Appl. Surf. Sci. Adv.*, vol. 12, p. 100332, Dec. 2022, doi: 10.1016/J.APSADV.2022.100332.

[186] H. Yang, S. Yang, J. Kong, A. Dong, and S. Yu, "Obtaining information about protein secondary structures in aqueous solution using Fourier transform IR spectroscopy," *Nat. Protoc. 2015 103*, vol. 10, no. 3, pp. 382–396, Feb. 2015, doi: 10.1038/nprot.2015.024.

[187] C. Singh *et al.*, "A Review: Drug Excipient Iincompatiblity by Ftir Spectroscopy," *Curr. Pharm. Anal.*, vol. 19, no. 5, pp. 371–378, Feb. 2023, doi: 10.2174/1573412919666230228102158.

[188] M. M. Blum and H. John, "Historical perspective and modern applications of Attenuated Total Reflectance – Fourier Transform Infrared Spectroscopy (ATR-FTIR)," *Drug Test. Anal.*, vol. 4, no. 3–4, pp. 298–302, Mar. 2012, doi: 10.1002/DTA.374.

[189] J. Bell, P. Nel, and B. Stuart, "Non-invasive identification of polymers in cultural heritage collections: evaluation, optimisation and application of portable FTIR (ATR and external reflectance) spectroscopy to three-dimensional polymer-based objects," *Herit. Sci.*, vol. 7, no. 1, pp. 1–18, Dec. 2019, doi: 10.1186/S40494-019-0336-0/TABLES/7.

[190] S. M. Lößlein, F. Mücklich, and P. G. Grützmacher, "Topography versus chemistry – How can we control surface wetting?," *J. Colloid Interface Sci.*, vol. 609, pp. 645–656, Mar. 2022, doi: 10.1016/J.JCIS.2021.11.071.

[191] J. W. Drelich, "Contact angles: From past mistakes to new developments through liquid-solid adhesion measurements," *Adv. Colloid Interface Sci.*, vol. 267, pp. 1–14, May 2019, doi: 10.1016/J.CIS.2019.02.002.

[192] F. Wang and T. Fang, "Retraction dynamics of water droplets after impacting upon solid surfaces from hydrophilic to superhydrophobic," *Phys. Rev. Fluids*, vol. 5, no. 3, p. 033604, Mar. 2020, doi: 10.1103/PHYSREVFLUIDS.5.033604/FIGURES/16/MEDIUM.

[193] M. Ponomar *et al.*, "Sessile Drop Method: Critical Analysis and Optimization for Measuring the Contact Angle of an Ion-Exchange Membrane Surface," *Membr. 2022, Vol. 12, Page 765*, vol. 12, no. 8, p. 765, Aug. 2022, doi: 10.3390/MEMBRANES12080765.

[194] S. Sharma, S. Jaiswal, B. Duffy, and A. K. Jaiswal, "Nanostructured Materials for Food Applications: Spectroscopy, Microscopy and Physical Properties," *Bioeng. 2019, Vol. 6, Page 26*, vol. 6, no. 1, p. 26, Mar. 2019, doi: 10.3390/BIOENGINEERING6010026.

[195] S. R. Falsafi, H. Rostamabadi, E. Assadpour, and S. M. Jafari, "Morphology and microstructural analysis of bioactive-loaded micro/nanocarriers via microscopy techniques; CLSM/SEM/TEM/AFM," *Adv. Colloid Interface Sci.*, vol. 280, p. 102166, Jun. 2020, doi: 10.1016/J.CIS.2020.102166.

[196] Y. F. Dufrêne, A. Viljoen, J. Mignolet, and M. Mathelié-Guinlet, "AFM in cellular and molecular microbiology," *Cell. Microbiol.*, vol. 23, no. 7, p. e13324, Jul. 2021, doi: 10.1111/CMI.13324.

[197] A. Viljoen *et al.*, "Force spectroscopy of single cells using atomic force microscopy," *Nat. Rev. Methods Prim. 2021 11*, vol. 1, no. 1, pp. 1–24, Sep. 2021, doi: 10.1038/s43586-021-00062-x.

[198] K. Xu and J. Chen, "High-resolution scanning probe lithography technology: a

review," *Appl. Nanosci.*, vol. 10, no. 4, pp. 1013–1022, Apr. 2020, doi: 10.1007/S13204-019-01229-5/FIGURES/5.
[199] C. Lissandrello, F. Inci, M. Francom, M. R. Paul, U. Demirci, and K. L. Ekinci, "Nanomechanical motion of Escherichia coli adhered to a surface," *Appl. Phys. Lett.*, vol. 105, no. 11, Sep. 2014, doi: 10.1063/1.4895132/13307132/113701_1_ACCEPTED_MANUSCRIPT.PDF.
[200] D. B. Hovis and A. H. Heuer, "The use of laser scanning confocal microscopy (LSCM) in materials science," *J. Microsc.*, vol. 240, no. 3, pp. 173–180, Dec. 2010, doi: 10.1111/J.1365-2818.2010.03399.X.
[201] D. Nečas and P. Klapetek, "Gwyddion: An open-source software for SPM data analysis," *Cent. Eur. J. Phys.*, vol. 10, no. 1, pp. 181–188, Feb. 2012, doi: 10.2478/S11534-011-0096-2/MACHINEREADABLECITATION/RIS.
[202] G. M. Harbers *et al.*, "Functionalized poly(ethylene glycol)-based bioassay surface chemistry that facilitates bio-immobilization and inhibits nonspecific protein, bacterial, and mammalian cell adhesion," *Chem. Mater.*, vol. 19, no. 18, pp. 4405–4414, Sep. 2007, doi: 10.1021/CM070509U/SUPPL_FILE/CM070509USI20070620_125315.PDF.
[203] N. L. Kazanskiy, S. N. Khonina, and M. A. Butt, "Plasmonic sensors based on Metal-insulator-metal waveguides for refractive index sensing applications: A brief review," *Phys. E Low-dimensional Syst. Nanostructures*, vol. 117, p. 113798, Mar. 2020, doi: 10.1016/J.PHYSE.2019.113798.
[204] J. Qin *et al.*, "Ultrahigh Figure-of-Merit in Metal-Insulator-Metal Magnetoplasmonic Sensors Using Low Loss Magneto-optical Oxide Thin Films," *ACS Photonics*, vol. 4, no. 6, pp. 1403–1412, Jun. 2017, doi: 10.1021/ACSPHOTONICS.7B00091/ASSET/IMAGES/LARGE/PH-2017-00091R_0004.JPEG.
[205] P. C. Ray, Z. Fan, R. A. Crouch, S. S. Sinha, and A. Pramanik, "Nanoscopic optical rulers beyond the FRET distance limit: fundamentals and applications," *Chem. Soc. Rev.*, vol. 43, no. 17, pp. 6370–6404, Aug. 2014, doi: 10.1039/C3CS60476D.
[206] J. R. Lakowicz, *Principles of Fluorescence Spectroscopy*. 2006.
[207] X. Zambrana-Puyalto, N. Maccaferri, P. Ponzellini, G. Giovannini, F. De Angelis, and D. Garoli, "Site-selective functionalization of plasmonic nanopores for enhanced fluorescence emission rate and Förster resonance energy transfer," *Nanoscale Adv.*, vol. 1, no. 6, pp. 2454–2461, 2019, doi: 10.1039/c9na00077a.
[208] A. S. Zalogina *et al.*, "Purcell effect in active diamond nanoantennas," *Nanoscale*, vol. 10, no. 18, pp. 8721–8727, May 2018, doi: 10.1039/C7NR07953B.
[209] T. Itoh, Y. S. Yamamoto, and Y. Ozaki, "Plasmon-enhanced spectroscopy of absorption and spontaneous emissions explained using cavity quantum optics," *Chem. Soc. Rev.*, vol. 46, no. 13, pp. 3904–3921, Jul. 2017, doi: 10.1039/C7CS00155J.
[210] G. Sun and J. B. Khurgin, "Enhancement of optical properties of nanoscaled objects by metal nanoparticles," *JOSA B, Vol. 26, Issue 12, pp. B83-B95*, vol. 26, no. 12, pp. B83–B95, Dec. 2009, doi: 10.1364/JOSAB.26.000B83.
[211] D. V. Guzatov, S. V. Vaschenko, V. V. Stankevich, A. Y. Lunevich, Y. F. Glukhov, and S. V. Gaponenko, "Plasmonic enhancement of molecular fluorescence near silver nanoparticles: Theory, modeling, and experiment," *J. Phys. Chem. C*, vol. 116, no. 19, pp. 10723–10733, May 2012, doi: 10.1021/JP301598W/ASSET/IMAGES/JP-2012-01598W_M022.GIF.

[212] P. A. Dmitriev *et al.*, "Hybrid Dielectric-Plasmonic Nanoantenna with Multiresonances for Subwavelength Photon Sources," *ACS Photonics*, vol. 10, no. 3, pp. 582–594, Mar. 2023, doi: 10.1021/ACSPHOTONICS.2C01332/ASSET/IMAGES/LARGE/PH2C01332_0004.JPEG.
[213] B. Peng *et al.*, "Quantum dots on vertically aligned gold nanorod monolayer: plasmon enhanced fluorescence," *Nanoscale*, vol. 6, no. 11, pp. 5592–5598, May 2014, doi: 10.1039/C3NR06341K.
[214] M. Algarra *et al.*, "Optical and Physicochemical Characterizations of a Cellulosic/CdSe-QDs@S-DAB5 Film," *Nanomaterials*, vol. 12, no. 3, p. 484, Feb. 2022, doi: 10.3390/NANO12030484/S1.
[215] M. Algarra, B. B. Campos, B. Alonso, C. M. Casado, J. C. G. Esteves Da Silva, and J. Benavente, "Inclusion of thiol DAB dendrimer/CdSe quantum dots based in a membrane structure: Surface and bulk membrane modification," *Electrochim. Acta*, vol. 89, pp. 652–659, Feb. 2013, doi: 10.1016/J.ELECTACTA.2012.10.143.
[216] C. Battocchio *et al.*, "Gold nanoparticles stabilized with aromatic thiols: Interaction at the molecule-metal interface and ligand arrangement in the molecular shell investigated by SR-XPS and NEXAFS," *J. Phys. Chem. C*, vol. 118, no. 15, pp. 8159–8168, Apr. 2014, doi: 10.1021/JP4126057/SUPPL_FILE/JP4126057_SI_001.PDF.
[217] C. M. Pradier, M. Salmain, L. Zheng, and G. Jaouen, "Specific binding of avidin to biotin immobilised on modified gold surfaces: Fourier transform infrared reflection absorption spectroscopy analysis," *Surf. Sci.*, vol. 502–503, pp. 193–202, Apr. 2002, doi: 10.1016/S0039-6028(01)01932-X.
[218] G. Han, Y. Kim, K. Kang, B. S. Lee, and J. K. Lee, "Protein-patterning on functionalized, non-biofouling poly[N-acryloxysuccinimide-co-oligo(ethylene glycol) methyl ether methacrylate] film-coated PET surfaces," *Macromol. Res.*, vol. 26, no. 3, pp. 263–269, Mar. 2018, doi: 10.1007/S13233-018-6035-Y/METRICS.
[219] P. Ihalainen *et al.*, "Application of Paper-Supported Printed Gold Electrodes for Impedimetric Immunosensor Development," *Biosens. 2013, Vol. 3, Pages 1-17*, vol. 3, no. 1, pp. 1–17, Dec. 2012, doi: 10.3390/BIOS3010001.
[220] A. L. De la Colina-Martínez, G. Martínez-Barrera, C. E. Barrera-Díaz, L. I. ávila-Córdoba, and F. Ureña-Núñez, "Characterization of recycled polycarbonate from electronic waste and its use in hydraulic concrete: Improvement of compressive performance," *Adv. Concr. Constr.*, vol. 5, no. 6, pp. 563–573, Dec. 2017, doi: 10.12989/ACC.2017.5.6.563.
[221] J. Liu, R. Q. Chen, C. P. Wang, Y. J. Zhao, and F. X. Chu, "Synthesis and characterization of polyethylene glycol-phenol-formaldehyde based polyurethane composite," *Sci. Reports 2019 91*, vol. 9, no. 1, pp. 1–9, Dec. 2019, doi: 10.1038/s41598-019-56147-x.
[222] H.-S. Jung *et al.*, "Polydopamine Encapsulation of Fluorescent Nanodiamonds for Biomedical Applications," *Adv. Funct. Mater.*, vol. 28, no. 33, p. 1801252, Aug. 2018, doi: 10.1002/ADFM.201801252.
[223] A. G. Young, A. J. McQuillan, and D. P. Green, "In situ IR spectroscopic studies of the avidin-biotin bioconjugation reaction on CdS particle films," *Langmuir*, vol. 25, no. 13, pp. 7416–7423, Jul. 2009, doi: 10.1021/LA900350S/SUPPL_FILE/LA900350S_SI_001.PDF.

[224] J. Mehne *et al.*, "Characterisation of morphology of self-assembled PEG monolayers: A comparison of mixed and pure coatings optimised for biosensor applications," *Anal. Bioanal. Chem.*, vol. 391, no. 5, pp. 1783–1791, Jul. 2008, doi: 10.1007/S00216-008-2066-0/FIGURES/8.
[225] S. Walke *et al.*, "Preparation and characterization of microencapsulated DwPT trivalent vaccine using water soluble chitosan and its in-vitro and in-vivo immunological properties," *Int. J. Biol. Macromol.*, vol. 107, pp. 2044–2056, Feb. 2018, doi: 10.1016/J.IJBIOMAC.2017.10.073.
[226] O. Suys, A. Derenne, and E. Goormaghtigh, "ATR-FTIR Biosensors for Antibody Detection and Analysis," *Int. J. Mol. Sci.*, vol. 23, no. 19, p. 11895, Oct. 2022, doi: 10.3390/IJMS231911895/S1.
[227] K.-Y. Law and H. Zhao, "Terminologies and Definitions," *Surf. Wetting*, pp. 123–133, 2016, doi: 10.1007/978-3-319-25214-8_6.
[228] K. M. Salleh, N. A. Z. Armir, N. S. N. Mazlan, M. Mostapha, C. Wang, and S. Zakaria, "Hydrogel- and aerogel-based composites: Biodegradable hydrogel and aerogel polymer blend-based composites," *Biodegrad. Polym. Blends Compos.*, pp. 355–388, Jan. 2022, doi: 10.1016/B978-0-12-823791-5.00019-3.
[229] O. Livnah, E. A. Bayer, M. Wilchek, and J. L. Sussman, "Three-dimensional structures of avidin and the avidin-biotin complex.," *Proc. Natl. Acad. Sci. U. S. A.*, vol. 90, no. 11, p. 5076, Jun. 1993, doi: 10.1073/PNAS.90.11.5076.
[230] M. Hebditch and J. Warwicker, "Web-based display of protein surface and pH-dependent properties for assessing the developability of biotherapeutics," *Sci. Reports 2019 91*, vol. 9, no. 1, pp. 1–9, Feb. 2019, doi: 10.1038/s41598-018-36950-8.
[231] B. A. Russell, K. Kubiak-Ossowska, P. A. Mulheran, D. J. S. Birch, and Y. Chen, "Locating the nucleation sites for protein encapsulated gold nanoclusters: a molecular dynamics and fluorescence study," *Phys. Chem. Chem. Phys.*, vol. 17, no. 34, pp. 21935–21941, Aug. 2015, doi: 10.1039/C5CP02380G.
[232] S. Wang *et al.*, "Efficient on-chip isolation of HIV subtypes," *Lab Chip*, vol. 12, no. 8, pp. 1508–1515, Apr. 2012, doi: 10.1039/c2lc20706k.
[233] M. Reth, "Matching cellular dimensions with molecular sizes," *Nat. Immunol. 2013 148*, vol. 14, no. 8, pp. 765–767, Jul. 2013, doi: 10.1038/ni.2621.
[234] X. Zhao *et al.*, "In vitro investigation of protein assembly by combined microscopy and infrared spectroscopy at the nanometer scale," *Proc. Natl. Acad. Sci. U. S. A.*, vol. 119, no. 32, p. e2200019119, Aug. 2022, doi: 10.1073/PNAS.2200019119/SUPPL_FILE/PNAS.2200019119.SAPP.PDF.
[235] M. G. P. Saifer, L. D. Williams, M. A. Sobczyk, S. J. Michaels, and M. R. Sherman, "Selectivity of binding of PEGs and PEG-like oligomers to anti-PEG antibodies induced by methoxyPEG-proteins," *Mol. Immunol.*, vol. 57, no. 2, pp. 236–246, Feb. 2014, doi: 10.1016/J.MOLIMM.2013.07.014.
[236] J. Mendez-Garza, B. Wang, A. Madeira, C. Di-Giorgio, G. Bossis, and C. Di Giorgio, "Synthesis and surface modification of spindle-type magnetic nanoparticles: gold coating and PEG functionalization," *J. Biomater. Nanobiotechnol.*, vol. 4, no. 03, pp. 222–228, 2013, doi: 10.4236/JBNB.2013.43027.
[237] M. Cheng *et al.*, "Biotin-Conjugated Upconversion KMnF3/Yb/Er Nanoparticles for Metabolic Magnetic Resonance Imaging of the Invasive Margin of Glioblastoma," *ACS Appl. Nano Mater.*, vol. 6, p. 8830, May 2023, doi:

10.1021/ACSANM.3C01215/ASSET/IMAGES/LARGE/AN3C01215_0007.JPEG.
[238] S. Rajan, K. Marimuthu, C. B. Ayyanar, and M. E. Hoque, "Development and in-vitro characterization of HAP blended PVA/PEG bio-membrane," *J. Mater. Res. Technol.*, vol. 18, pp. 4956–4964, May 2022, doi: 10.1016/J.JMRT.2022.04.130.
[239] E. Güven, K. Duus, M. C. Lydolph, C. S. Jørgensen, I. Laursen, and G. Houen, "Non-specific binding in solid phase immunoassays for autoantibodies correlates with inflammation markers," *J. Immunol. Methods*, vol. 403, no. 1–2, pp. 26–36, Jan. 2014, doi: 10.1016/J.JIM.2013.11.014.
[240] K. J. Land, D. I. Boeras, X. S. Chen, A. R. Ramsay, and R. W. Peeling, "REASSURED diagnostics to inform disease control strategies, strengthen health systems and improve patient outcomes," *Nat. Microbiol. 2018 41*, vol. 4, no. 1, pp. 46–54, Dec. 2018, doi: 10.1038/s41564-018-0295-3.
[241] H. Zetterberg, "Blood-based biomarkers for Alzheimer's disease—An update," *J. Neurosci. Methods*, vol. 319, pp. 2–6, May 2019, doi: 10.1016/J.JNEUMETH.2018.10.025.
[242] Y. Hang, J. Boryczka, and N. Wu, "Visible-light and near-infrared fluorescence and surface-enhanced Raman scattering point-of-care sensing and bio-imaging: a review," *Chem. Soc. Rev.*, vol. 51, no. 1, pp. 329–375, Jan. 2022, doi: 10.1039/C9CS00621D.
[243] X. Zambrana-Puyalto, N. Maccaferri, P. Ponzellini, G. Giovannini, F. De Angelis, and D. Garoli, "Site-selective functionalization of plasmonic nanopores for enhanced fluorescence emission rate and Förster resonance energy transfer," *Nanoscale Adv.*, vol. 1, no. 6, pp. 2454–2461, Jun. 2019, doi: 10.1039/C9NA00077A.
[244] D. S. Y. Ong, S. J. de Man, F. A. Lindeboom, and J. G. M. Koeleman, "Comparison of diagnostic accuracies of rapid serological tests and ELISA to molecular diagnostics in patients with suspected coronavirus disease 2019 presenting to the hospital," *Clin. Microbiol. Infect.*, vol. 26, no. 8, pp. 1094.e7-1094.e10, Aug. 2020, doi: 10.1016/J.CMI.2020.05.028.
[245] D. W. Crook *et al.*, "Antibody testing for COVID-19: A report from the National COVID Scientific Advisory Panel," *Wellcome Open Res.*, vol. 5, 2020, doi: 10.12688/WELLCOMEOPENRES.15927.1.
[246] K. T. Abe *et al.*, "A simple protein-based surrogate neutralization assay for SARS-CoV-2," *JCI Insight*, vol. 5, no. 19, Oct. 2020, doi: 10.1172/JCI.INSIGHT.142362.
[247] S. Feng, M. Z. Hua, M. S. Roopesh, and X. Lu, "Rapid detection of three mycotoxins in animal feed materials using competitive ELISA-based origami microfluidic paper analytical device (μPAD)," *Anal. Bioanal. Chem.*, vol. 415, no. 10, pp. 1943–1951, Apr. 2023, doi: 10.1007/S00216-023-04612-Y/FIGURES/4.
[248] L. Wu, G. Li, X. Xu, L. Zhu, R. Huang, and X. Chen, "Application of nano-ELISA in food analysis: Recent advances and challenges," *TrAC Trends Anal. Chem.*, vol. 113, pp. 140–156, Apr. 2019, doi: 10.1016/J.TRAC.2019.02.002.
[249] M. Zhang *et al.*, "Super-resolved Optical Mapping of Reactive Sulfur-Vacancies in Two-Dimensional Transition Metal Dichalcogenides," *ACS Nano*, vol. 15, no. 4, pp. 7168–7178, Apr. 2021, doi: 10.1021/ACSNANO.1C00373/ASSET/IMAGES/MEDIUM/NN1C00373_M001.GIF.

Appendix A

Appendix

A.1 Declaration of Copyright Clearance Agreements

Reference Number	License Supplier	License Number
[28]	Springer Nature	Permission not required
[98]	Springer Nature	5606490126766
[120]	John Wiley and Sons	5606490352422
[159]	Springer Nature	5606490501205
[160]	Springer Nature	5606490600603
[172]	Springer Nature	5606490757761